The Measurement and Optimization of Direct Laser Acceleration

by

Hongmei Tang

A dissertation submitted in partial fulfillment
of the requirements for the degree of
Doctor of Philosophy
(Electrical and Computer Engineering)
in the University of Michigan
2024

Doctoral Committee:

Associate Professor Louise Willingale, Chair
Professor Almantas Galvanauskas
Professor Karl Krushelnick
Dr. Yong Ma
Professor Alexander G. R. Thomas

Hongmei Tang
tanghm@umich.edu
ORCID iD: 0000-0003-4885-6863

ACKNOWLEDGMENTS

First and foremost, I am extremely grateful to my supervisor Prof. Louise Willingale for her invaluable advice, continuous guidance, encouragement, and patience throughout my PhD study. Having the opportunity to work with Louise has been the most fortunate thing that has happened to me during my research journey. She not only opened the door to the world of plasma physics research for me but also provided me with numerous opportunities to communicate and collaborate with excellent researchers in the field of plasma.

I have had the incredible privilege of working with exceptional researchers at CUOS, University of Michigan. Many thanks to Research Scientist Dr. Anatoly Maksimchuk for operating the T-Cubed laser and supporting my scintillator project. And it has been a truly great pleasure to work with Dr. Brandon Russell. We worked together on setting up the scintillator experiment. Besides, he taught me how to use Osiris simulation software and was always so patient with my questions. Thank you to Dr. Paul Campbell for helping me with the data analysis, providing experimental advice, and sharing his coding expertise with me. I would like to thank Prof. Alec Thomas for teaching me numerical modeling knowledge and having inspirational discussions. And many thanks to Research Scientist Dr. Yong Ma, who helped me a lot in running simulations and visualizing the data. Also thank you to Veronica Contreras for performing shot day with me in Rochester. Thank you to Brendan Stassel for giving me a lot of help, support and entertainment. I sincerely appreciate Prof. Karl Krushelnick, and Prof. Almantas Galvanauskas for being my committee member and giving valuable comments on this thesis. In addition, thank you to Karl for organizing DPP practice talk seminars, where I improved my presentation skills.

I also have had the great fortune to work with many outstanding researchers from other universities and institutions. I would like to thank General Atomics Scientist Dr. Mario Manuel for providing scintillator samples and having helpful discussions.

Many thanks to Prof. Alexey Arefiev from UCSD and his group. Alexey offered me numerous constructive suggestions during our bi-weekly discussions of the direct laser acceleration (DLA) project. Thank you to I-Lin Yeh and Kavin Tangtartharakul for running simulations and contributing to the theoretical work. I would like to express gratitude to Dr. Hui Chen from Lawrence Livermore National Laboratory (LLNL) for her treasured and continuous support in calibrating electron energy spectra for DLA project. Also, I am really grateful to the scientists and staff at the Laboratory for Laser Energetics, University of Rochester. Dave Canning and his team tried their best to overcome technical difficulties and provide experimental support. I would like to acknowledge Dr. Marija Vranic and her student Róbert Babjak, who work at the University of Lisbon, for their valuable contribution to the DLA work. And thank you to Dr. Félicie Albert (LLNL) and Dr. Jessica L Shaw (LLE) for your useful advice on DLA project.

Last but not least, I would like to express my gratitude to my friend Wenqian Zou and my family. Wenqian, I want to thank you for your love and understanding. You checked on the progress of my thesis every day and encouraged me to complete the writing. Also, I would like to thank my parents for unconditionally supporting my choice.

TABLE OF CONTENTS

LIST OF FIGURES

FIGURE

LIST OF TABLES

TABLE

ABSTRACT

This thesis presents experimental measurements and numerical modeling of electron acceleration optimization and laser channel formation in relativistic laser interactions with underdense plasma, as well as scintillator characterization for proton imaging applications.

The Direct Laser Acceleration (DLA) of electrons during a high-energy, picosecond laser interaction with a gas jet target was studied experimentally and numerically. Experiments using the OMEGA EP facility demonstrate that the electron maximum energy and mean energy are significantly enhanced by controlling the laser focusing geometry. Energetic electron beams with maximum energy (~ 400 MeV) exceeding 20 times the ponderomotive energy of the laser pulse were measured under certain focusing, pulse energy, and plasma density conditions. 2D particle-in-cell simulations demonstrate that the laser focusing condition will change the laser pulse evolution, channel field generation, and electron oscillations, all of which contribute to the final electron energy. Through this observation, a simple model was developed to calculate the optimal laser focal spot size in more general conditions and is validated by experimental data.

DLA was further optimized experimentally by tilting the gas nozzle toward the laser source, providing a plasma density with a sharp up ramp and gentle down ramp profile. Using a picosecond pulse with energy of 63 J and a plasma with a peak density of 8×10^{18} cm^{-3}, a 30° tilted nozzle produced 4.5 times the electrons of a straight nozzle. 2D simulations reveal that the plasma density gradient affects the final number and energy of electrons by changing the laser self-focusing, electron injection position, and the sheath field evolution. Electrons start to be accelerated from a lower density in the sharp upward ramp region and lose less energy while traveling through a sheath field formed in a gentle downward ramp region.

The channel formation and filamentation evolution in the DLA process were diag-

nosed using proton deflectometry and optical probing methods. Through comparing proton images from shot to shot, the channel width at the stable stage is found to be dependent on the laser focal spot size, and the final channel width is related to the pulse duration. Simulations show that a pulse with a duration longer than one picosecond may form new modes as it propagates in the channel.

The final part of this thesis characterized the spatial resolution and imaging properties of plastic scintillators. Laser-driven proton beams with broad energy spectra were used to illuminate the scintillators. Different types and thicknesses of Eljen Technology scintillators are compared to determine their intrinsic point spread function. Point projection imaging of a mesh is used to compare the imaging resolution of the scintillator to the frequently used but single-shot imaging detector, radiochromic film, and was found to be reasonably comparable and sufficient for many experimental applications.

CHAPTER 1

Introduction

The advent of the high-intensity ultrashort pulse laser systems, based on the chirped pulse amplification (CPA) technique, has enabled the experimental investigation of matter under extreme conditions and expanded the frontiers of high energy density physics. The CPA technique was first conceived by Donna Strickland and Gérard Mourou in the 1980s [12], through stretching the laser pulse in the time domain, amplifying the stretched pulse, and finally compressing the pulse to ultra-short duration, the laser power could be significantly increased without damaging the gain medium. A brief schematic showing the CPA mechanism is shown in Figure 1.1. The groundbreaking work of Strickland and Mourou laid the foundation for the construction of advanced multi-terawatt, petawatt class laser facilities, such as Omega EP at the University of Rochester [4], Hercules at the University of Michigan [13], ALEPH at Colorado State University [14], and ZEUS at the University of Michigan [15]. The focusing of the intense short-pulse laser enables peak intensity to far exceed $10^{18}\mathrm{Wcm}^{-2}$. When irradiated by such a high-intensity laser, the electrons in the material are driven to speeds close to the speed of light, meaning that the interaction is in the relativistic regime.

These cutting-edge high-energy high-power laser facilities have broadened the horizons of research across multiple disciplines. Laser interactions with plasma encompass

a diverse range of phenomena that occur when ultrashort high-intensity laser pulses propagate into the ionized matter, covering a variety of processes that span from the microscopic to the macroscopic scales. The electromagnetic fields in the plasma can be incredibly strong and are desirable to accelerate particles to extraordinarily high energies [16, 17, 18]. The accelerated particles have applications in medical and materials science [19, 20], as well as in high-energy physics experiments. In astrophysics research, laser-plasma interactions enable controlled investigation of laboratory astrophysics, such as supernova and cosmic rays research, by recreating the high-energy environments found in space [21, 22, 23, 24]. Furthermore, the intense radiation produced in laser-plasma interactions provides a tool to study the behavior of dense and highly energetic materials found in stars and planets, prompting radiative hydrodynamics research [25, 26]. Another important area facilitated by laser-plasma interactions is inertial confinement fusion [27, 28], where nuclear fusion is triggered by compressing and heating a fuel target to the point where nuclear reactions occur using laser beams.

Although the above are just a few examples of the many applications of relativistic-intensity laser plasma interactions, lots of complex processes and their underlying mechanisms remain to be fully explored. This dissertation mainly focuses on direct laser acceleration of electrons and high-energy-density diagnostic technology, which are discussed in more detail in the following chapters.

1.1 Electron acceleration

The plasma-based particle accelerator was first proposed by Tajima and Dawson in 1979 [18]. Electrons that are trapped in a plasma wake, that is created by an intense electromagnetic pulse, can be accelerated by the wake longitudinal field. This is known as laser

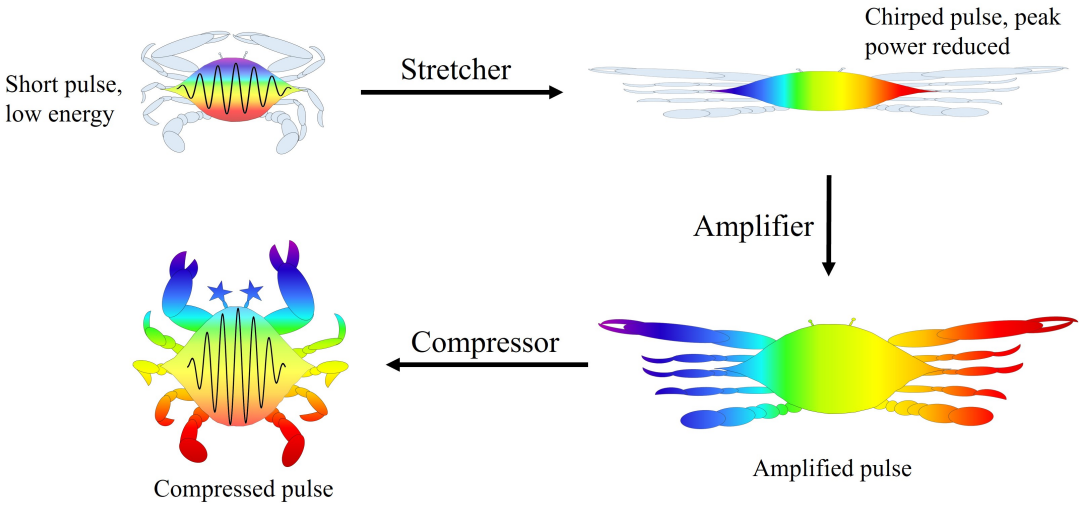

Figure 1.1: A cartoon scheme of chirped pulse amplification. A short pulse from an oscillator with a low energy is temporally stretched, which reduces its peak power. Then the stretched pulse is amplified, increasing the pulse energy. Finally, the pulse is compressed and its power increases dramatically.

wakefield acceleration (LWFA). In their estimates, a laser with a power of 10^{18} Wcm^{-2} could produce a longitudinal accelerating field with a magnitude of 100 GV/m in a plasma with a density of 10^{18} cm^{-3}. The acceleration gradient, which is three orders of magnitude higher than that of a conventional accelerator, could generate electrons of GeV energy level over a distance of several centimeters.

The advancements in laser technology have progressed LWFA to multiple regimes. Self-modulated LWFA (SMLWFA) can be driven by a laser with a pulse duration $\sim$ 1 ps and a modest $a_0 \lesssim 1$ [29, 30, 31, 32]. The laser in the plasma is modulated by Raman scattering and the self-modulated instability, resulting in a train of laser micro-pulses at the plasma frequency and consequently large amplitude plasma waves grow, which accelerate electrons to relativistic energies. Another area that attracted great interest is the LWFA in blowout regime [33, 34], where the laser pulse is short (on the order of several 10 fs to 100 fs), intense and matched to the plasma density. High energy

electrons with low divergence and energy spread are trapped at the rear of a wake bubble and accelerated by the longitudinal wakefield.

As the laser pulse duration is increased to the order of a picosecond and the normalized laser intensity a_0 exceeds 1, direct laser acceleration (DLA) becomes the dominant acceleration mechanism [35]. A high-intensity laser will create an ion channel and accelerate electrons within the channel while propagating through an underdense plasma [36, 37, 38]. Highly-energized electrons with large emittance, small divergence, and wide energy spread are able to be obtained from particle interaction with the laser electric and magnetic fields. The first experiment reporting DLA was conducted by Gahn in 1999 [35]. A 1.2 TW long-pulse laser was focused by an $f/3$ parabolic mirror to a high-pressure gas nozzle (plasma density up to 4×10^{20} cm^{-3}) with a peak laser intensity of 4×10^{18} $\mathrm{W/cm}^2$. Electrons with energy up to 12 MeV were emitted from He gas and reproduced by 3D particle-in-cell simulations. In 2005, Mangles et al. reported an experiment performed on Vulcan laser where a pulse with a peak intensity of 3×10^{20} $\mathrm{W/cm}^2$ (corresponding to a $a_0 \sim 15$) generated an ion channel in an underdense plasma [39]. They verified that the electron acceleration was attributed to DLA instead of LWFA by measuring the transmitted laser spectrum. A strong correlation between the modulation in transmitted laser spectra and the effective temperature of the electron beam was observed at low intensities ($\sim 10^{19}$ $\mathrm{W\ cm}^{-2}$) [31, 40]. However, this correlation was not observed at higher intensity ($\sim 3 \times 10^{20}$ $\mathrm{W\ cm}^{-2}$), suggesting that the principal acceleration mechanism is not plasma wave acceleration [39]. Thereafter, more research was conducted to study DLA and its application in driving bright directional x-ray radiation [41, 42, 43, 44].

In order to better understand the mechanism of electron energy gain in the cavitated channel, many numerical simulations were carried out to reveal the laser evolution and

the electron motion from different angles [45, 46, 47]. The theoretical studies were initiated using a plane wave propagating through a well-constructed preformed channel, with or without the presence of external background electric or magnetic fields. The electron energy gain is a result of the cumulative effects of both the longitudinal and transverse components of the laser electric field. A number of background fields in the plasma, including channel electric fields and self-generated magnetic field, have been shown to indirectly influence the beam-particle energy exchange through changing the dephasing rate, electron initial condition, controlling energy loss, etc.

However, DLA is a complex and dynamic process, which is sensitive to a number of factors and unexpected subsequent variables under experimental conditions. Previous investigations performed by Hussein et al. on the Omega EP laser facility demonstrated the existence of an ideal plasma density for accelerating electrons [48]. A picosecond pulse was focused on a plasma plume which was excited by a nanosecond long pulse laser heating a CH foil and produced electrons with energy up to 500 MeV. Though high energy electrons were generated, the target has a long density gradient region, making the processes more difficult to understand and being potentially less stable. Therefore, optimizing the experimental configuration for DLA under well-controlled conditions is essential for the production of steady electron beams and the advancement of next generation accelerators.

1.2 Proton imaging

Proton imaging is a very useful diagnostic tool for studying various physical processes under extreme conditions, such as laser channeling [42], inertial fusion implosions [49], and magnetic field generation [50], etc. The target normal sheath acceleration (TNSA)

proton beams are widely utilized for performing proton deflectometry in high energy density physics research [51]. Typical ion detectors used for measuring the proton beam image are Columbia resin no. 39 (CR39), or radiochromic film (RCF). CR39 is renowned for its ability to record the tracks left by charged particles. After chemical etching, the radiation tracks are visible in the material, providing information about the incident ion species, energy, and angle of incidence. RCF is a material that undergoes color changes in response to ionizing radiation. This property allows for the precise mapping of ion distributions, energy spectra measurement, and beam spatial profile visualization. Both CR39 and RCF have excellent spatial resolution for imaging applications. However, they are single-use detectors and need scanning to process and analyze data. As proton deflectometry experiments move from being exclusively conducted at the high-energy glass-based laser systems, typically having less than 10 shots per day, to new higher-repetition extremely high-power Ti: Sapphire systems, CR39 and RCF are becoming less practical, leading to the implementation of scintillator based detectors [52, 53, 54, 55]. In addition to being multi-use, a high spatial resolution is also required particularly for imaging and resolving fine structures ($< 100\ \mu\mathrm{m}$), resulting in the need to characterize scintillator properties before bringing it into operation.

An experiment designed to characterize the spatial resolution of certain types of scintillators is described in chapter 5 [56].

1.3 Thesis Outline

In this thesis, the electron acceleration from relativistic intensity laser interaction with underdense plasma is studied and scintillator detectors for proton imaging are characterized.

Experiments and numerical modeling were combined to explore the direct laser acceleration mechanism and to optimize experimental conditions for electron generation. The DLA work demonstrated in this dissertation facilitates access to future compact plasma-based accelerators using extremely high power picosecond-duration lasers and offers potential utility in delivering bright hard X-ray sources for advanced imaging applications in material detection and medical science.

The experiments designed to characterize the spatial resolution of the scintillator detectors are initially driven by the demand for multi-use proton detectors in high repetition rate laser systems. The challenge of ion imaging in a high rep-rate laser chamber lies in improving reusability while maintaining a high spatial resolution for imaging microstructures. A micro-scaled mesh grid was illuminated by a TNSA proton beam produced from short pulse (400 fs) laser interaction with copper foil to test the resolution limit of the scintillator. The results demonstrate that the scintillator has a comparable resolution to RCF, indicating the feasibility of substituting RCF with scintillators in future proton diagnostic systems.

Chapter 2 provides the relevant fundamental theory of intense laser pulse interactions with plasma.

Chapter 3 introduces high-power laser systems – OMEGA EP laser and T-Cubed laser – that were utilized to perform the experiments in this thesis. This chapter also offers an overview of the diagnostic techniques and equipment used for data collection. Additionally, a brief introduction to particle-in-cell simulations is included.

Chapter 4 focuses on the direct laser acceleration project. The influences of the laser focusing geometry and plasma density gradient on electron acceleration are studied experimentally and numerically. The proton radiography and optical probe method, including shadowgraphy and interferometry, were used to image the channel formation

and filamentation development in the DLA process. The effects of laser focusing conditions and pulse duration on the channel evolution are presented.

Chapter 5 characterizes the spatial resolution and examines the imaging quality of different scintillators. The results lead the way in constructing reusable ion detectors in high energy density physics experiments.

Chapter 6 summarizes and concludes the work described in this thesis. Possible extensions for future investigations are also suggested.

CHAPTER 2

Theoretical Background

2.1 Basic of Laser Plasma

2.1.1 Intense laser field

The field of a laser with a wavelength of λ_L and an angular frequency of ω_L can be described using a vector potential $\mathbf{A} = \mathbf{A}_0 \sin(\mathbf{k} \cdot \mathbf{r} - \omega_L t)$, where $k_L = 2\pi n/\lambda_L$ is the laser wavenumber and n is the refractive index. For a plane wave with the electric field **E** polarized in the y-direction and the magnetic field **B** in the z-direction, the **E** and **B** fields are:

$$\mathbf{E} = -\frac{\partial \mathbf{A}}{\partial t} = \omega_L A_0 \cos(k_L x - \omega_L t)\ \hat{y} = E_0 \cos(k_L x - \omega_L t)\ \hat{y}, \tag{2.1}$$

$$\mathbf{B} = \nabla \times \mathbf{A} = k_L A_0 \cos(k_L x - \omega_L t)\ \hat{z} = B_0 \cos(k_L x - \omega_L t)\ \hat{z}, \tag{2.2}$$

where $E_0 = \omega_L A_0$, $B_0 = k_L A_0$ and $\hat{y}$ and $\hat{z}$ are unit vectors in the y and z directions respectively.

To define "high intensity" for lasers, we usually use the normalized vector potential

a:

$$a = \frac{eA}{m_e c} = \frac{eE}{m_e c \omega_L} \tag{2.3}$$

where e is the electron charge, m_e is the electron mass and E is the electric field. It is more often to use the peak normalized vector potential, which is proportional to the peak electric field:

$$a_0 = \frac{eE_0}{m_e c \omega_L}. \tag{2.4}$$

It is the ratio of the quiver energy to the rest mass energy. As a_0 approaches 1, electron oscillation velocity gradually becomes close to the speed of light c, the electron kinetic energy approaches the electron rest mass energy, $m_0 c^2$ (0.511 MeV), and the relativistic effects of the electron moving in the electromagnetic field become significant. The value of the peak normalized vector potential can be calculated using the laser wavelength and laser intensity I:

$$a_0 = 0.85 \times 10^{-9} \lambda_L[\mu m](I[W/cm^2])^{1/2}. \tag{2.5}$$

Here, the laser wavelength is in units of $\mu\mathrm{m}$ and the intensity is in units of $\mathrm{W/cm^2}$. The intensity of the laser is given by the magnitude of the Poynting vector, S, averaged over the laser period:

$$I = \langle |S| \rangle = \frac{1}{\mu_0} \langle |E \times B| \rangle = \frac{\epsilon_0 c}{2} E_0^2 \tag{2.6}$$

where μ_0 is the vacuum permeability constant and ϵ_0 is the vacuum permittivity. For

$a_0 = 1$, $\lambda_L = 1\mu\mathrm{m}$, the laser intensity is $I \sim 10^{18}\ \mathrm{W/cm^2}$. The interaction of a laser pulse with an a_0 above unity is referred to as the relativistic regime.

2.1.2 Electron ionization

In a laser-plasma interaction, the ionization process often plays a significant role in shaping the dynamics of the plasma and influencing the overall behavior of the interaction. When an intense laser beam irradiates a target, different ionization mechanisms may come into play at different intensities, leading to complex and dynamic phenomena. The Keldysh parameter γ_k, which is a dimensionless quantity, is often used to characterize the ionization processes:

$$\gamma_k = \sqrt{\frac{I_P}{2U_P}} \tag{2.7}$$

where I_P is the ionization potential and $U_P = e^2 E_L^2 / 4 m_e \omega_L^2$ is the non-relativistic ponderomotive potential with E_L being the laser electric field. The Keldysh parameter is the ratio between the binding strength of the electron in an atom or molecule and the electric field strength of an external laser field.

Figure 2.1 shows three main optical field ionization processes in laser plasma interactions. For $\gamma_k \gg 1$, the dominant ionization process is the multi-photon ionization (figure 2.1 (a)). Multi-photon ionization is a process in which an electron absorbs multiple photons of light simultaneously or in rapid succession, leading to the release of the electron from its potential well. In traditional single-photon ionization, a photon with sufficient energy can promote an electron from a bound state to a free state, causing ionization. However, in multi-photon ionization, the energy of a single photon may not be enough to achieve ionization, but the cumulative energy of multiple lower-energy photons can

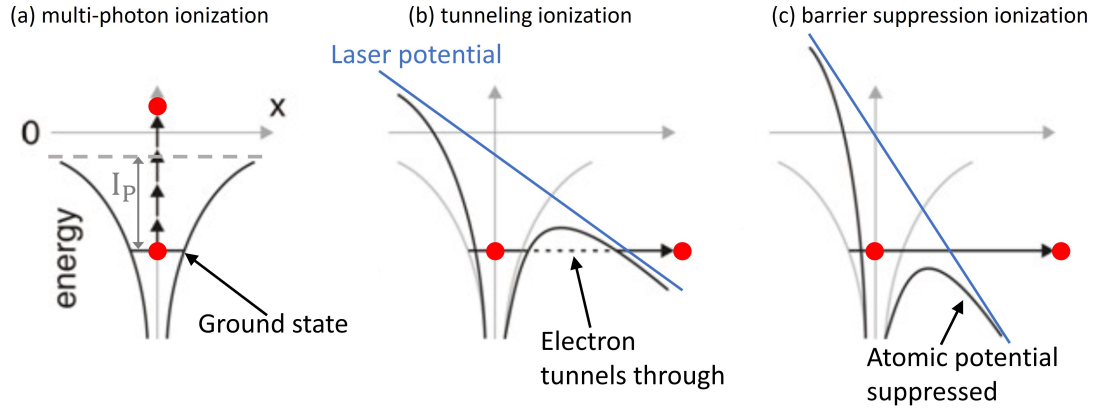

Figure 2.1: Three ionization processes: (a) multi-photon ionization, (b) tunneling ionization, and (c) barrier suppression ionization.

be sufficient to remove an electron. As γ_k decreases, the ionization mechanism transitions from multiphoton ionization to tunnel ionization (figure 2.1 (b)). When an atom is subjected to an intense electric field, the Coulomb potential is suppressed, so the potential energy barrier around the atom becomes thinner and more penetrable. Electrons without enough kinetic energy to overcome the potential energy barrier can "tunnel" through the barrier, leading to ionization. If the laser intensity is extremely high such that $\gamma_k \ll 1$, the barrier suppression ionization occurs. The laser electric field can easily suppress the Coulomb potential, effectively reducing or eliminating the potential energy barrier as illustrated in figure 2.1 (c). The laser intensity is usually above a threshold of $I[\mathrm{W/cm^2}] \sim 4 \times 10^9 (\mathrm{I_P[eV]})^4 \mathrm{Z}^{-2}$, where Z is the charge state after ionization.

2.1.3 Single particle motion in an electromagnetic field

Consider a single electron irradiated by an electromagnetic wave characterized by $E(\mathbf{r},t)$, $B(\mathbf{r},t) \propto \exp[i(\mathbf{k}\cdot\mathbf{r} - \omega_L t)]$. The motion of a single electron is governed

by the Lorentz force equation:

$$\frac{d\mathbf{p}}{dt} = -e(\mathbf{E} + \mathbf{v} \times \mathbf{B}), \tag{2.8}$$

where **v** denote the electron quiver velocity, $\mathbf{p} = \gamma m_e \mathbf{v}$ is the electron quiver momentum and $\gamma = 1/\sqrt{1 - v^2/c^2} = \sqrt{1 + p^2/m_e c^2}$ is the relativistic Lorentz factor. The $(\mathbf{v} \times \mathbf{B})$ force only becomes important when the electron velocity approaches the speed of light because $|\mathrm{E}| = \mathrm{c}|\mathrm{B}|$.

If the laser $a_0 < 1$, the electron motion is primarily dominated by the laser electric field and the contribution from the magnetic field is trivial. Electrons oscillate linearly along the electric field orientation.

If it is in the relativistic intensity regime with $a_0 \gtrsim 1$, the electric field will oscillate electrons and the $(\mathbf{v} \times \mathbf{B})$ force will change the direction of electron motion. To analytically solve equation 2.8, we can use the vector potential **A** to express the electric and magnetic fields of the laser:

$$\mathbf{E} = -\nabla\phi - \frac{\partial \mathbf{A}}{\partial t}, \tag{2.9}$$

$$\mathbf{B} = \nabla \times \mathbf{A}, \tag{2.10}$$

where ϕ is the electrostatic potential. Substituting equation 2.9 and 2.10 to the equation of electron motion gives:

$$\frac{d\mathbf{p}}{dt} = -e\left[-\nabla\phi - \frac{\partial \mathbf{A}}{\partial t} + \mathbf{v} \times (\nabla \times \mathbf{A})\right]. \tag{2.11}$$

Using the vector identity of $\mathbf{v} \times (\nabla \times \mathbf{A}) = (\nabla \mathbf{A}) \cdot \mathbf{v} - (\mathbf{v} \cdot \nabla)\mathbf{A}$ and the convective

derivative of $\frac{d}{dt} = \frac{\partial}{\partial t} + (\mathbf{v} \cdot \nabla)$, the equation 2.11 can be rewritten as:

$$\frac{d\mathbf{p}}{dt} = -e\left[-\nabla\phi - \frac{d\mathbf{A}}{dt} + (\nabla\mathbf{A}) \cdot \mathbf{v}\right]. \tag{2.12}$$

The first term on the right side is $\nabla\phi = 0$ for the single electron, therefore the above equation becomes:

$$\frac{d\mathbf{p}}{dt} = -e\left[-\frac{d\mathbf{A}}{dt} + (\nabla\mathbf{A}) \cdot \mathbf{v}\right] = -e\left[-\frac{d\mathbf{A}}{dt} + (\nabla\mathbf{A}) \cdot \frac{\mathbf{p}}{\gamma m_e}\right]. \tag{2.13}$$

Moving the $\frac{d}{dt}$ terms to the same side gives:

$$\frac{d}{dt}(\mathbf{p} - e\mathbf{A}) = -e(\nabla\mathbf{A}) \cdot \mathbf{v} = -e(\nabla\mathbf{A}) \cdot \frac{\mathbf{P}}{\gamma m_e}. \tag{2.14}$$

Consider a plane wave with $\mathbf{A} = A\hat{y}$ propagating in x-direction, which means $\partial\mathbf{A}/\partial y = 0$. The equation 2.14 yields the following equations in the (x, y)-plane:

$$\frac{d}{dt}p_x = -ev_y\frac{\partial A_y}{\partial x}, \tag{2.15}$$

$$\frac{d}{dt}(p_y - eA_y) = 0. \tag{2.16}$$

The equation 2.16 gives the electron transverse momentum of:

$$\frac{p_y}{m_e c} = a, \tag{2.17}$$

with a being the normalized vector potential as discussed in section 2.1.1.

For the longitudinal component, by plugging equation 2.17 into the relativistic momentum, $p^2 = p_x^2 + p_y^2 = (\gamma^2 - 1)m_e^2c^2$, the longitudinal momentum can be written

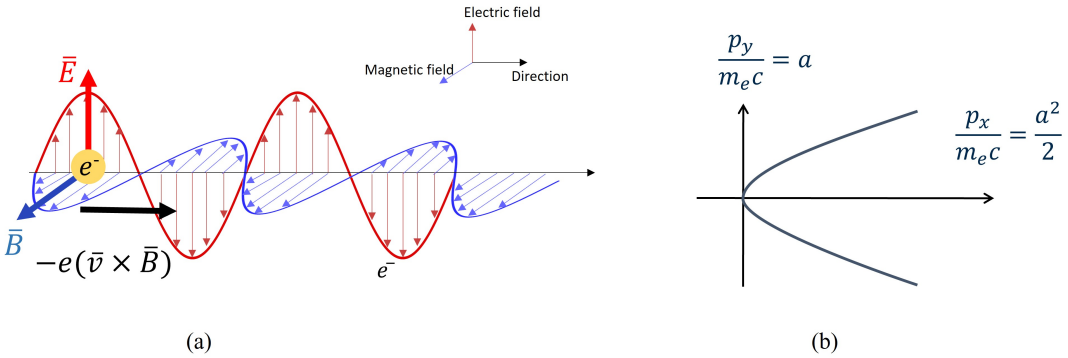

(a) (b)

Figure 2.2: (a) Single electron irradiated by a plane wave in vacuum. (b) Electron motion in momentum space.

as:

$$\frac{p_x^2}{m_e^2 c^2} = \gamma^2 - 1 - a^2. \tag{2.18}$$

Now consider the electron energy $\mathcal{E}$:

$$\mathcal{E} = \gamma m_e c^2 \tag{2.19}$$

$$\rightarrow \frac{d\mathcal{E}}{dt} = m_e c^2 \frac{d\gamma}{dt} = -e\mathbf{v}\cdot\mathbf{E} \tag{2.20}$$

$$\rightarrow m_e c^2 \frac{d\gamma}{dt} = -ev_y E_y = ev_y \frac{\partial A_y}{\partial t}. \tag{2.21}$$

Subtracting equation 2.21 from equation 2.15 gives:

$$c\frac{dp_x}{dt} - m_e c^2 \frac{d\gamma}{dt} = -ev_y \left(c\frac{\partial A_y}{\partial x} + \frac{\partial A_y}{\partial t} \right). \tag{2.22}$$

Since it is a plane wave with $A_y = A_{y0}\exp(\omega_L t - kx)$, the term on right hand side of

the above equation $(c\frac{\partial A_y}{\partial x} + \frac{\partial A_y}{\partial t}) = 0$. Hence, the integration of equation 2.22 becomes:

$$\gamma = \frac{p_x}{m_e c} + 1. \tag{2.23}$$

Now, by plugging the above expression into equation 2.18, the γ factor can be eliminated, giving the longitudinal momentum:

$$\frac{p_x}{m_e c} = \frac{a^2}{2}. \tag{2.24}$$

Then γ factor has the form of:

$$\gamma = \frac{a^2}{2} + 1. \tag{2.25}$$

This is the maximum energy that an electron could gain under the vacuum condition. Combining the expression of transverse momentum and longitudinal momentum yields:

$$\frac{p_x}{m_e c} = \frac{1}{2}\left(\frac{p_y}{m_e c}\right)^2, \tag{2.26}$$

which means the electron moves along a parabolic shape in the momentum space, as shown in figure 2.2 (b).

The electron position on its trajectory is related to the momentum as:

$$\frac{dx}{dt} = \frac{c}{\gamma}\frac{p_x}{m_e c} = \frac{1}{\gamma}\frac{a^2 c}{2}, \tag{2.27}$$

$$\frac{dy}{dt} = \frac{c}{\gamma}\frac{p_y}{m_e c} = \frac{1}{\gamma}\, ac. \tag{2.28}$$

Change to the wave frame and use $\tau = t - x/c$ and $\frac{d\tau}{dt} = 1 - \frac{1}{c}\frac{dx}{dt}$. For constant of

motion, $\frac{p_x}{m_e c} = \gamma - 1$, then $\frac{\gamma}{c}\frac{dx}{dt} = \gamma - 1$, which gives $\gamma\left(1 - \frac{1}{c}\frac{dx}{dt}\right) = 1$, $\frac{d\tau}{dt} = 1/\gamma$. The equation 2.27 and 2.28 become:

$$\frac{dx}{d\tau} = \frac{a^2 c}{2}, \tag{2.29}$$

$$\frac{dy}{d\tau} = ac. \tag{2.30}$$

The integration of equation 2.29 and 2.30 give:

$$x(\tau) = \frac{ca_0^2}{4}\left[\tau + \frac{1}{2\omega_L}\sin(2\omega_{\mathrm{L}}\tau)\right], \tag{2.31}$$

$$y(\tau) = \frac{ca_0}{\omega_L}\sin(\omega_{\mathrm{L}}\tau). \tag{2.32}$$

2.1.4 Ponderomotive force

As a laser propagates into a plasma, the beam is usually focused onto a small spot at its focal plane, resulting in high peak laser intensity and spatial gradients of the laser electric field. Electrons irradiated by this oscillating laser field experience a cyclical drift in response to the spatial gradient in the electric field intensity, moving towards the regions of lower intensity. Intuitively, the electron moves through a longer distance when it is pushed from the center of the laser outward in the first half laser cycle because of high field strength near the center. Then in the second half cycle, since the periphery electric fields are lower, the electron feels a weaker returning force and therefore will not move back to its original position. This cumulative effect, sustained over a number of laser cycles, results in the net displacement of electrons away from the central region of highest intensity. The force due to the intensity gradient is known as the ponderomotive force. As a consequence of this displacement, an electron-depleted channel forms in the plasma along the trajectory of the laser pulse, which is referred to as ponderomotive

channeling. This channel exhibits a reduced electron density compared to its surroundings, creating an area of lower plasma density. The ponderomotive channeling process continues until the channel electric field due to spatial charge separation balances the ponderomotive force, leading to an equilibrium state.

The ponderomotive force is proportional to the laser intensity gradient. Here we will use the same coordinates as before, where the laser wave is propagating in the x-direction and the electric field is oscillating in the y-direction. In the non-relativistic regime, the ponderomotive force, F_P, has the form of:

$$F_P = -\frac{e^2}{4m_e\omega_L^2}\frac{\partial E_0^2}{\partial y}. \tag{2.33}$$

The relativistic ponderomotive force can be derived using the equation of electron motion 2.14. The electron momentum consists of a fast quiver motion component, which follows the equation 2.17, and a slowly varying component. Averaging the electron motion equation over laser cycle gives the expression of the relativistic ponderomotive force:

$$F_P = -\frac{e^2}{2m_e\langle\gamma\rangle}\nabla\langle\mathbf{A}^2\rangle \tag{2.34}$$

$$= -\frac{m_e c^2}{2\langle\gamma\rangle}\nabla\langle a^2\rangle. \tag{2.35}$$

where $\langle\ \rangle$ symbols represent the time average.

The potential associated with the ponderomotive force is:

$$U_P = m_e c^2(\langle\gamma\rangle - 1), \tag{2.36}$$

where $\langle\gamma\rangle = \sqrt{1+\langle a^2\rangle}$. $\langle a^2\rangle = a_0^2/2$ for linearly polarized light and $\langle a^2\rangle = a_0^2$ for

circularly polarized light.

2.2 Relativistic laser pulse interaction with underdense plasma

Underdense plasmas have electron densities lower than the critical density for a given laser frequency, allowing the laser field to propagate through and facilitating a unique environment for relativistic laser-plasma interactions. The critical density, $n_c = \epsilon_0 m_e \omega_L^2 / e^2$, is defined as the density at which electron plasma frequency equals the laser frequency. The laser propagation in an underdense plasma can be affected by a number of factors, such as relativistic self-focusing, stimulated Raman scattering, and the formation of filaments. These nonlinear and dynamic processes give rise to complex particle dynamics, which in turn influence the propagation of the laser wave and plasma wave propagating through the plasma. The interaction of relativistic intensity lasers with underdense plasmas holds immense potential for advancing our understanding of fundamental physics, including quantum electrodynamics in strong fields [57] and the behavior of relativistic particles [36]. Moreover, the exploration of this regime finds applications in areas like compact particle accelerators [20], attosecond pulse generation [58], and novel radiation sources [59], thereby opening avenues for transformative advancements at the intersection of laser science and plasma physics.

2.2.1 Self-focusing

Self-focusing is a nonlinear optical process induced by the change of the refractive index in the medium as exposed to an intense electromagnetic wave. The axial refrac-

tive index becomes higher than the off-the-axis refractive index in the material, which curves the beam wavefront and the laser tends to converge. In an underdense plasma, the self-focusing phenomenon can be driven by the relativistic effect or the ponderomotive effect.

At relativistic intensities $> 10^{18}\ \mathrm{Wcm}^{-2}$, the electrons experience an increase in their effective mass due to them moving relativistically. This causes electrons to be more massive in the high-intensity region with a mass correction of $\langle\gamma\rangle m_e$ and the refractive index becomes larger than that of the marginal region of the beam. Consequently, the laser focuses and this is referred to as relativistic self-focusing.

In regions of high electric field intensity, electrons are pushed away by the ponderomotive force, leading to a local depletion of electrons. This electron expulsion creates a channel within the plasma where the electron density is lower on axis, contributing to an increase in the refractive index and prompting a focusing effect. This is known as ponderomotive self-focusing.

In an underdense plasma, the refractive index η can be expressed by:

$$\eta = \sqrt{1 - \left(\frac{\omega_p}{\langle\gamma\rangle\omega_L}\right)^2} = \sqrt{1 - \frac{n_e}{\langle\gamma\rangle n_c}}, \tag{2.37}$$

where $\omega_p = \sqrt{n_e e^2/\epsilon_0 m_e}$ is the electron plasma frequency. The effect of both relativistic and ponderomotive self-focusing is to provide a higher refractive index along the laser axis and a lower refractive index away from the axis. Due to the phase velocity $v_p = c/\eta$, an increased refractive index slows down the light wave phase velocity, and the edge of the beam will travel faster than the axial part. This leads to the converging of the wavefront towards the axis, which means that an initial area with a higher intensity automatically becomes more intense as the laser propagates.

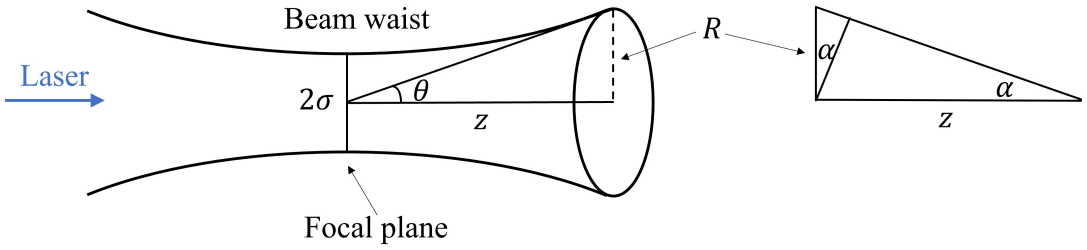

(a) Diffraction (b) self-focusing

Figure 2.3: The effect of (a) diffraction and (b) self-focusing on a beam in plasma.

As the laser power exceeds a threshold value, the self-focusing effect in the plasma can balance the laser diffraction. Figure 2.3 illustrates the geometric optics of the relative effects of self-focusing on laser diffraction. Consider a Gaussian laser beam with a radial profile of $a(r) = a_0 \exp(-\mathrm{r}^2/\sigma^2)$, where a is the vector potential and 2σ is the beam waist. The classical diffraction angle without non-linear effects is [60]:

$$\theta = \frac{dR}{dz} \simeq \frac{\sigma}{Z_R} = \frac{2}{k_L \sigma}. \text{ (for small } \theta) \tag{2.38}$$

where $Z_R = \pi\sigma^2/\lambda$ is the Rayleigh length.

Since $\gamma = (1 + a^2/2)^{1/2}$ for a linearly polarized beam, the refractive index can be expressed by:

$$\eta = \sqrt{1 - \frac{\omega_p^2}{(1 + a^2/2)^{1/2}\omega_L^2}} = \frac{c}{v_\phi}. \tag{2.39}$$

And the difference between the phase velocity at the center and the edge of the laser beam is:

$$|\frac{\Delta v_\phi}{c}| = \frac{\omega_p^2\, a^2}{8\, \omega_L^2}. \tag{2.40}$$

Now consider the self-focusing effect in figure 2.3 (b). Since the angle α is small, we have: $\sin\alpha \simeq \tan\alpha \simeq \alpha$. And the maximum path difference for the center and outside laser beam is

$$\Delta L = \sin\alpha \mathrm{R} = \alpha \mathrm{R} = \alpha^2 \mathrm{z}. \tag{2.41}$$

While ΔL can also be calculated using the phase velocity $\Delta L = |\Delta v_\phi| t = |\frac{v_\phi}{c}| z$. Therefore the maximum focusing angle is

$$\alpha^2 = \frac{\omega_p^2 \, a^2}{8 \, \omega_L^2}. \tag{2.42}$$

If $\alpha > \theta$, the relativistic effects are greater than natural diffraction and self-focusing occurs. This gives:

$$a^2\sigma^2 = \frac{e^2 E^2}{m^2 \omega_L^2 c^2}\sigma^2 > \frac{32c^2}{\omega_p^2}. \tag{2.43}$$

From the above equation, the threshold power that allows the relativistic self-focusing to overcome the diffraction effect can be derived [61]:

$$P_c = 17 \, \frac{\omega_L^2}{\omega_p^2} = 17 \, \frac{n_c}{n_e} \ [\mathrm{GW}], \tag{2.44}$$

which is referred to as critical laser power.

Other than the effects in the radial direction, the self-focusing will also compress the laser pulse in the longitudinal direction because the leading edge of the pulse sees a higher density, which reduces the phase velocity of the laser head [62, 63]. Therefore, the pulse duration is shortened.

2.2.2 Laser channeling

If the laser pulse length is greater than the plasma period $\tau_L > 1/\omega_p$, one of the consequences of the ponderomotive effect is the formation of an ion channel in underdense plasma [64, 65, 42] as electrons are continuously expelled radially. The relativistic self-channeling of a TW laser in underdense plasma was first clearly observed using Thomson scattering in 1994 by P. Monot et al. [66]. The transverse ponderomotive force of a laser pulse with power surpassing the critical threshold P_c is capable of expelling all electrons from the high-intensity region to the spherical area. Due to the large mass difference, the electrons respond much faster than ions. Electrons are pushed away from the ions in the radial direction and ions are left behind. And since the laser pulse can sustain this strong force for a long time period, electrons are unable to return to their original positions due to the ponderomotive force, resulting in the formation of a channel free of electrons with a positive charge of background ions along the laser propagation direction. This self-generated channel with denser boundaries serves as a wave guide for the laser pulse and may extend the light propagation distance to many Rayleigh lengths. Due to the charge separation, quasi-static localized electric fields will grow as the laser travels through plasma. There is a longitudinal electric field [67] forming near the channel opening and a transverse electric field forming in the channel [48]. In addition to electric fields, an azimuthal magnetic field will also be generated due to the electron currents being driven inside the channel. Although the amplitude of these channel fields is several orders smaller than the laser field, they can significantly alter the dynamics of particles that move in the channel and enhance electron energy gain from incoming laser pulse [45]. (The effects of these fields are discussed in more detail in the following sections 2.2.4.) The channel formation has been proven to be vitally important not only for particle acceleration but also has a potential application for fast

ignition. In 1994, a three-phase scheme for fast ignition inertial confinement fusion using laser channeling was proposed by M. Tabak et al. [68]. A pre-formed laser-driven channel directs a second intense laser pulse to penetrate through the dense ablation material with minimum energy loss, enabling strong electron heating and therefore high coupling efficiency of the laser energy to the ignition core. The potential impact of this concept has prompted more investigation of the plasma channel dynamics and laser guiding [69, 70, 71, 72, 73, 42].

2.2.3 Filamentation

Filamentation can occur as high intensity laser propagates through plasma and leads to beam breakup [74, 75, 40]. The filamentation instability can be triggered by ponderomotive effects or relativistic effects and can cause modifications of the propagating pulse by spatially modulating the laser intensity in the radial direction. The efficiency of laser energy coupling to particles and electron acceleration will be negatively affected by the filamentation because of the reduced laser intensity, the beam breaking up and the beam scattering [76, 77].

2.2.4 Direct Laser Acceleration

A relativistic intensity ($a_0 \gg 1$) laser with a picosecond pulse duration ($\tau_L \gtrsim 1\mathrm{ps}$) is able to accelerate electrons to high energy level exceeding several hundred MeV while propagating through an underdense plasma [36, 35, 78, 79, 67, 80]. The predominant acceleration mechanism is direct laser acceleration (DLA), which refers to a regime where electrons gain energy directly from the transverse component of the laser electric field through several different methods. Electrons irradiated by the transverse electro-

magnetic fields will oscillate in the transverse direction, and the $\mathbf{v} \times \mathbf{B}$ force turns the transverse electron momentum into the longitudinal direction. Unlike the dynamic in a vacuum environment discussed in section 2.1.3, electrons that move in the ion channel can break the momentum oscillation symmetry with the assistance of weak background channel fields, allowing net energy gain.

As discussed in section 2.2.2, the laser pulse expels electrons in the radial direction and creates an ion channel. A small number of electrons will be injected into the channel from the channel opening or the channel boundaries, which can be triggered by several mechanisms. In a complex interaction with strong self-generated static electric and/or magnetic fields, electrons may go through betatron oscillations with small amplitude in the self-generated static electric and/or magnetic fields [36]. A resonance occurs if the frequency of the electron oscillation along the polarization of the laser pulse electric field coincides with the laser frequency, enabling effective energy exchange between the laser and particles. Another mechanism is the stochastic perturbations on single electron motion [78, 81], which arise from a variety of sources, including fluctuations in the laser intensity, phase errors, and interactions with other particles or fields within the plasma. The stochastic perturbations may induce sufficient dephasing and enhance electron acceleration by enabling particles to gain additional energy from the laser field through a process known as stochastic heating. In addition, parametric amplification of electron oscillations across the plasma channel and a longitudinal electric field at the channel opening have also been found to modulate the electron motion and lead to energy increase [79, 67].

The quasi-static fields formed in the plasma channel alter the electron motion trajectories and can significantly enhance energy transfer [45]. The longitudinal electric field at the channel opening helps to push electrons into the channel and offers a small

initial longitudinal velocity, which decreases the electron dephasing with the laser wave [67]. This means electrons are capable of spending more time being accelerated. The charge separation in the ion channel generates a transverse electric field E_{ion}. The channel transverse electric field alters the electron transverse oscillation direction, making electron transverse velocity anti-parallel to the laser electric field over extended segments. The electrons moving along with the laser creates an azimuthal magnetic field surrounding themselves, which play an important role in confining the electron transverse excursion [82, 47]. This self-generated magnetic field has been shown to facilitate a rapid energy transfer from the laser pulse to an accelerated electron via transversely bouncing electrons deflection multiple times in the channel.

To describe the electron motion in the laser-driven plasma channel, let's consider a single electron irradiated by a plane electromagnetic wave in an ion channel with a quasi-static transverse electric field $\mathbf{E}_{ion}$. Here we use same notation as section 2.1.3. The electric field $\mathbf{E}_L = (0, E_y, 0)$ and magnetic fields $\mathbf{B}_L = (0, 0, B_z)$ of the laser can be expressed using the normalized non-dimensional vector potential $\mathbf{a}$, $\mathbf{E}_L = -(m_e c/e)(\partial \mathbf{a}/\partial t)$, $\mathbf{B}_L = (m_e c^2/e)\nabla \times \mathbf{a}$. The total electric field, $\mathbf{E} = \mathbf{E}_L + \mathbf{E}_{ion}$, is the summation of the oscillating laser wave field and the static background field $\mathbf{E}_{ion}$ due to the charge separation in the ion channel. The static component in the laser channel can be written by $\mathbf{E}_{ion} = \omega_{p0}^2 m_e y/2|e|\hat{y}$, where $\hat{y}$ is a unit vector in y direction. The electron motion is governed by the following equations:

$$\frac{d\mathbf{p}}{dt} = -e\mathbf{E} - \frac{e}{\gamma m_e}\left[\mathbf{p} \times \mathbf{B}\right], \tag{2.45}$$

$$\frac{d\mathbf{r}}{dt} = \frac{c}{\gamma}\frac{\mathbf{p}}{m_e c}, \tag{2.46}$$

where $\gamma = \sqrt{1 + p^2/m_e^2c^2}$ is the Lorentz factor, **r** is the electron position and **p** is the electron momentum. Equation 2.45 yields the following equations of motions in the $(x,\ y)$-plane:

$$\frac{dp_x}{dt} = -\frac{e}{\gamma m_e} p_y B_z, \qquad \frac{dp_y}{dt} = -e(E_y + E_{ion}) + \frac{e}{\gamma m_e} p_x B_z, \tag{2.47}$$

$$\frac{dx}{dt} = v_x = \frac{p_x}{m\gamma}, \qquad \frac{dy}{dt} = v_y = \frac{p_y}{m\gamma}. \tag{2.48}$$

As discussed in section 2.1.3, $d\gamma/dt = -ev_yE_y/(m_ec^2)$ in the vacuum. However, in the quasi-static channel, the variation of γ factor is rewritten as:

$$\frac{d\gamma}{dt} = -\frac{ev_y}{m_ec^2}(E_y + E_{ion}) = -\frac{ev_y}{m_ec^2}E_y - \frac{ev_y}{m_ec^2}\frac{m\omega_p^2 y}{2e} \tag{2.49}$$

Combining with equation 2.45 gives:

$$\frac{d\gamma}{dt} = \frac{d}{dt}\left(\frac{p_x}{m_ec}\right) - \frac{\omega_p^2}{2c^2} y \cdot \frac{dy}{dt} \tag{2.50}$$

This implies that, as the electron moves along the channel, the following quantity remains conserved [46, 83]:

$$\gamma - \frac{p_x}{m_ec} + \frac{\omega_p^2}{4c^2} y^2 = \mathcal{I} = \mathcal{I}_0 = \text{const.} \tag{2.51}$$

with $\mathcal{I}$ represent the integral of motion. If an electron has an initial axial momentum p_0 and initial transverse displacement y_0, then

$$\mathcal{I}_0 = \sqrt{1 + \frac{p_0^2}{m_e^2c^2}} - \frac{p_0}{m_ec} + \frac{\omega_p^2 y_0^2}{4c^2}. \tag{2.52}$$

The theoretical maximum energy of the most energetic electrons is then determined based on their initial positions and the background plasma density [46, 84]:

$$\gamma_{\text{max}} \simeq 2\mathcal{I}^2 \frac{\omega_L^2}{\omega_p^2}. \tag{2.53}$$

Equation 2.53 indicates that the electrons with larger first transverse oscillation amplitudes y_0 are able to achieve higher energies for a given plasma density. An electron goes through several betatron oscillations in the channel. After achieving the maximum energy in the channel, an electron may decelerate due to the dephasing with the laser wave. The maximum electron resonant amplitude is:

$$y_{\text{max}} = \frac{2c}{\omega_p} \sqrt{\left(\frac{a_0\, \omega_p}{\epsilon\, \omega_L} \right)^{2/3} - 1}\,, \tag{2.54}$$

where $\epsilon = a_0 \omega_p / (\omega_L \mathcal{I}^{3/2})$ is a threshold parameter on the order of unity that relates to the electron initial conditions. Equation 2.54 explicitly demonstrates that a laser pulse with a higher a_0 can accelerate electrons with an initial position further away from the channel axis.

The above theoretical analysis is proposed under the assumption of plane wave propagation in a preformed channel. However, in real experiments, where a Gaussian beam is utilized and the plasma has a limited length scale of millimeters, the interaction condition is much more complicated. Numerous factors, including laser power, laser focusing geometry, pulse duration, plasma density, density gradient, etc, could potentially influence the DLA process. For instance, if the laser is focused to a tiny spot size on the order of micrometers at its focal plane, the wavefront is curved and consequently, part of the transverse electric field will be converted to the longitudinal direction. The longitudinal electric field, which decreases with beam focal spot size, is proven to do negative work

on the electron [85]. The beam size also affects the formation of the channel, i.e. a larger beam could sustain a cleaner channel in a longer distance. More details are investigated and discussed in Chapter 4.

2.2.5 Current filamentation instability

The current filamentation instability is a significant phenomenon that arises when there are anisotropic electron current distributions in a plasma [86, 87, 88]. This instability leads to the development of filament-like structures in the current and plasma density, causing the growth of magnetic fields and particle scattering. In laser-plasma interactions, the laser electric field can drive an anisotropic distribution of electrons, leading to the generation of currents within the plasma. When the current becomes sufficiently anisotropic, it can trigger the current filamentation instability. The magnetic fields generated through Ampère's law can significantly impact the dynamics of the plasma interaction. They can confine and scatter electrons, alter the propagation of the laser pulse, and influence the overall energy transport within the plasma. For example, in laser driven plasma wakefield acceleration, the instability-induced magnetic fields can affect the propagation of the accelerated electron bunch, potentially leading to enhanced particle trapping and acceleration.

The growth rate (Γ) of the current filamentation instability can be derived using the two-fluid Vlasov-Maxell equations [89]. Assuming the initial densities of two counter-streaming electron beams are homogeneous, the growth rate is given by :

$$\Gamma = \frac{1}{\sqrt{2}} \left[\sqrt{(1/\gamma^3 + k_y^2)^2 + 4k_y^2 v_0^2/\gamma} - (1/\gamma^3 + k_y^2) \right]^2, \tag{2.55}$$

where γ is the Lorentz factor, k_y is the transverse component of the wave vector and v_0

is the initial velocity in the units of speed of light.

2.2.6 Betatron radiation

Betatron X-ray radiation is a natural consequence of the relativistic DLA electron oscillations in a laser-driven plasma channel. This process involves intricate interplay between electromagnetic fields, electron motion, and the self-generated magnetic fields within the channel. The generated X-ray beam has the features of wide energy bandwidth, short duration, and high yield, making it potentially useful for extensive applications across areas of high-energy physics, material science, and medical imaging [80, 90, 91, 92, 41, 93]. Besides, the emitted radiation carries valuable information about the accelerated electron bunch, including its energy distribution, transverse source size, and trajectories.

The electron motion is similar to the behavior within an undulator or wiggler magnet, which are well-known devices in synchrotron light sources for producing intense radiation. Figure 2.4 show the schematic of electron orbits and X-ray emission in two regimes. The undulator refers to a regime where the electromagnetic wave radiated in the same direction along the entire electron trajectory. This occurs for highly collimated radiation in a small cone. The maximal angle between the electron trajectory and the propagation axis ϕ is smaller than the opening angle of the radiation cone $\Delta\theta \sim 1/\gamma$. While in the wiggler regime, the X-rays can be emitted in different directions from different portions of the electron trajectory with $\phi > \Delta\theta \sim 1/\gamma$. A dimensionless parameter $K = \gamma\phi$ is often used to distinguish two regimes. For an undulator, $K \ll 1$, which indicates a small divergence. And for a wiggler, $K \gg 1$.

In the DLA process, electrons undergo strong oscillations, similar to a wiggler situation. The radiation spectrum is broadband and quasi-continuous. The intensity of

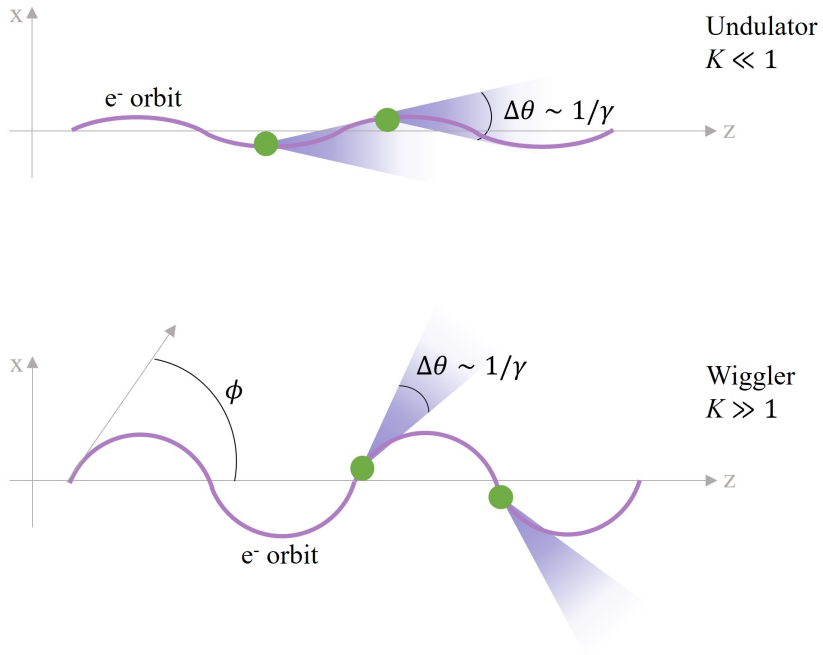

Figure 2.4: Illustration of the undulator (top) and wiggler (bottom). The lobes represent the direction of the instantaneously emitted radiation. Figure adapted from Ref [1].

radiation per unit frequency is given by [94]:

$$\frac{dI}{d\omega} = \sqrt{3}\frac{e^2}{c}\gamma\frac{\omega}{\omega_c}\int_{\frac{\omega}{\omega_c}}^{\infty} K_{5/3}(x)dx, \tag{2.56}$$

where $K_{5/3}$ is a modified Bessel function of the second kind and ω_c is the critical frequency. The critical frequency is defined as [80, 95, 96]:

$$\omega_c = (3/2)k_\beta r_\beta \gamma^3 \omega_\beta, \tag{2.57}$$

where $\omega_\beta = \omega_p/(2\gamma)^{1/2}$ is the betatron frequency, $k_\beta = k_p/(2\gamma)^{1/2}$ is the betatron wavenumber, and r_β is the oscillation radius. Figure 2.5 shows an example of a synchrotron-like spectrum, which is generated from a DLA simulation using laser pa-

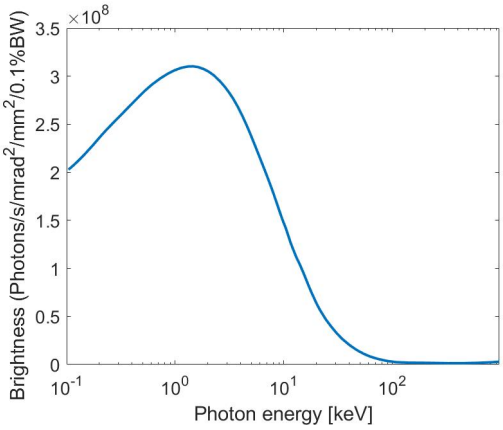

Figure 2.5: A simulated synchrotron-like x-ray spectrum from an electron betatron oscillation on a semi-logarithmic scale. Based on a figure from Ref [2].

rameters of $a_0 = 4.28,\ \tau_{duration} = 0.7$ ps and energy of 20 J.

2.3 Intense laser interaction with overdense plasma

2.3.1 Electron heating

An intense laser pulse is able to heat electrons in an overdense plasma ($n_e > n_c$) through various mechanisms, such as resonance absorption [97, 98], vacuum heating [99, 100], and $\mathbf{j} \times \mathbf{B}$ heating [101].

For resonance absorption, consider an intense laser pulse hits a target. The leading edge of the pulse ionizes the target and creates an expanding plasma with a density gradient. If the laser is p-polarized and has an oblique incident angle, it will propagate through the underdense plasma region and be reflected at the surface of electron density of $n_e = n_c \cos^2\theta$, where n_c is the critical density and θ is the incidence angle [60]. The electric field component along the direction of the density gradient can tunnel toward the critical density. At the critical surface where the laser frequency matches the natural

frequency of plasma oscillations, a resonance occurs, leading to efficient energy transfer from the laser to electron plasma waves [60]. As the plasma wave propagates toward lower densities, it acquires a larger wave number and deposits its energy to electrons through Landau damping, leading to strong absorption of radiation and production of hot electrons.

If the plasma has a steep density gradient, the vacuum heating takes place [99, 100]. Plasma electrons can be dragged out into the vacuum by the oscillating laser pulse and sent back into plasma as the field reverses. The returning velocity is about the quiver velocity of $v_{osc} = eE/m_e\omega_L$. As electrons re-enter the overdense plasma, electrons are no longer affected by the laser and they gain energy. This energy exchange is more efficient than the usual resonant absorption when $v_{osc}/\omega_L > L$, where L is the density gradient length.

As the laser intensity reaches $10^{19}\mathrm{W/cm^2}$, the relativistic electrons have $v_{osc} \sim c$, and the effect of the magnetic field emerges. The $\mathbf{j}\times\mathbf{B}$ heating plays a major role in electron acceleration through the oscillating part of the ponderomotive force [101, 102, 103, 104]. For a laser with intensity $I_L\lambda_L^2[\mathrm{W}\mu\mathrm{m}^2/\mathrm{cm}^2]$, the accelerated electron energy distribution [105, 106] are generally given by $T_e = 0.511\times\ (\sqrt{1+I_L\lambda_L^2/(2.8\times10^{18})}\ - 1)[\mathrm{MeV}]$.

In summary, these three mechanisms—resonance absorption, vacuum heating, and $\mathbf{j}\times\mathbf{B}$ heating—play pivotal roles in electron dynamics, wave generation, and the overall evolution of the plasma system, paving the way for a variety of applications in fields such as ion acceleration, fusion research, and astrophysics.

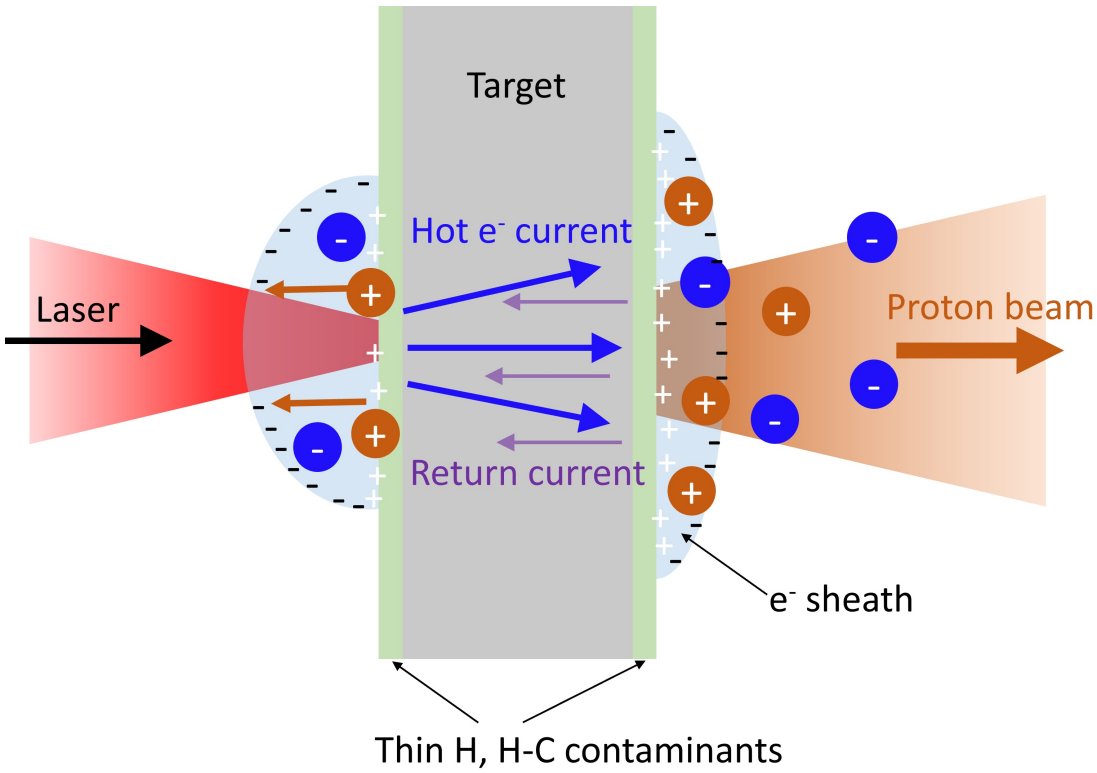

Figure 2.6: A schematic of the target normal sheath acceleration.

2.3.2 Target Normal Sheath Acceleration

The target normal sheath acceleration (TNSA) mechanism is probably the most studied ion acceleration mechanism and has profound implications across particle acceleration, fusion research, laboratory astrophysics, and material science [107, 108]. The TNSA protons, characterized by high energy, broad energy spectrum, directional emission, short acceleration time, and small virtual source size [109, 110], often serve as diagnostic tools for probing plasmas and matter under extreme conditions [111, 112]. The spatial and temporal evolution of the electromagnetic field in the interaction region of interest can be measured by sending TNSA protons through the interaction area and projecting them onto ion detectors in the far field.

The interaction of a laser pulse ($I_L \gtrsim 10^{18}\mathrm{W/cm^2}$) and a solid foil target with a few micrometer thickness can produce protons with energy extending to multi MeV [113, 108]. Figure 2.6 shows a schematic figure of the TNSA mechanism. The intense laser field heats electrons in the overdense plasma through one or several processes described in section 2.3.1. Electrons that gain sufficient energy are able to travel through the target sheet and into the vacuum. The charge separation between the electrons and the plasma ions creates a quasi-static electric field with a direction normal to the target surface and is called a "sheath". The sheath field acts as an electrostatic barrier, which returns the electrons building up the field back into the target and they may go through repeated heating cycles near the front surface. A thin ($\sim$ nm) layer of water vapor and/or hydrocarbon contaminants attached to the surface of the target will be ionized in the quasi-static field and ions will be accelerated to MeV energies over micrometer sections. Due to the high charge-to-mass ratio, protons are primarily accelerated. TNSA occurs on both the front and rear surfaces of the foil as hot electrons can leave the target from both sides. But the rear-surface acceleration has a high efficiency and ions emitted from the rear side gain higher maximum energy than front side ions.

The TNSA ion energy spectrum has an exponential shape and is related to the electron temperature. For acceleration time t, the number of accelerated ions (N_i) per unit energy and unit surface is given by [114]:

$$\frac{dN_i}{d\mathcal{E}_i} \propto \frac{n_{i0}t}{\sqrt{2m_i\mathcal{E}_i}} \exp\left(-\sqrt{\frac{2\mathcal{E}_i}{Zk_BT_e}}\right), \tag{2.58}$$

where $\mathcal{E}_i$ is the ion energy, n_{i0} is the initial ion density, m_i is the ion mass, Z is the charge state and T_e is the electron temperature. The ion spectra are cut off at a maximum energy

$\mathcal{E}_i^{max}$ of:

$$\mathcal{E}_i^{max} \simeq 2Zk_BT_e \left[\ln\left(\frac{2\omega_i t}{\sqrt{2e}}\right)\right]^2, \tag{2.59}$$

where ω_i is the plasma ion frequency and $e \approx 2.71828$ is the mathematical constant.

The TNSA proton beam typically has a divergence with a half angle extending to a few tens of degrees. And the virtual source size of protons is about 10 μm [115, 116].

2.4 Ion propagation in matter

The ions propagating through matter undergo successive interactions with the material particles, including electronic stopping, nuclear stopping, and scattering. High-energy ions deposit their energy to the material electrons mainly via the electronic stopping process. This occurs through inelastic collisions between the energetic ions and material electrons, resulting in electron excitation and ionization. The incoming ion polarizes the electronic cloud of the atoms it encounters, creating temporary electron-hole pairs. The ion kinetic energy is transferred to the electrons, promoting electrons to higher energy states. Subsequently, the excited electrons undergo relaxation processes. They can emit photons as they return to lower energy states, contributing to energy loss in the form of photon generation. Alternatively, the energy can be transferred to other electrons through inelastic collisions, leading to further electron excitation. Ions can also transfer a small portion of energy to the target nuclei through nuclear stopping, potentially leading to nuclear reactions and the emission of secondary particles.

The energy loss of ions within the material follows a characteristic profile. It typically starts with a region of minimal energy loss per unit length at the surface due to electronic stopping. As the ion penetrates deeper, both electronic and nuclear stopping contribute

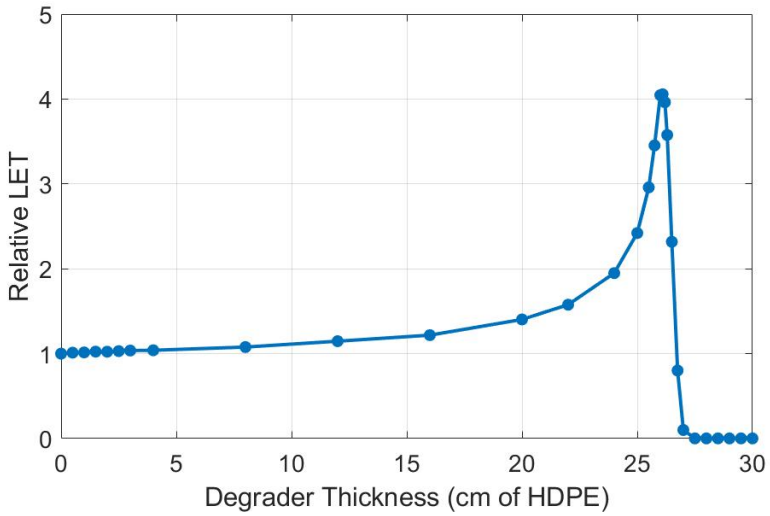

Figure 2.7: Bragg Curve for 205 MeV protons propagating in a high density polyethylene (HDPE) with density of 0.97 $\mathrm{g/cm^3}$. The Bragg peak occurs in 26.1 cm in the material. Figure based on the Brookhaven National Laboratory NSRL Bragg peak measurements [3].

to an increase in energy loss, eventually peaking at a maximum point known as the Bragg peak. Beyond the Bragg peak, energy loss dramatically decreases as the ion energy diminishes. Figure 2.7 shows an example of the Bragg curve of a 205 MeV proton in polyethylene [3]. The energy loss rate, or linear energy transfer (LET) is a function of the distance through the stopping medium.

CHAPTER 3

Methods

3.1 High power laser systems

The advent of the high-intensity ultrashort pulse laser systems based on the chirped pulse amplification (CPA) technique enables the experimental investigation of matter under extreme conditions and expands the frontier of high energy density physics. The CPA technique was first conceived by Donna Strickland and Gerard Mourou in the 1980s [12] and it earned them the Nobel Prize in Physics in 2018. The laser pulse is intentionally stretched in the time domain by applying a spectral chirp. The chirped pulse is then amplified using a laser amplifier, boosting laser energy while maintaining its stretched profile. The laser power is kept below the damage threshold for the amplification medium. After amplification, the chirped pulse is sent through a dispersive element, typically a pair of diffraction gratings or specialized optics. As a result, the stretched pulse is recompressed in time, turning it into an ultrashort pulse with a high peak power. The CPA process significantly enhances the peak intensity of the pulse without damaging the gain medium. Multi-terawatt and even petawatt class laser facilities, like Omega EP at the University of Rochester [4], Hercules at the University of Michigan [13], and ALEPH at Colorado State University [14], have been available for multiple fields of research, such

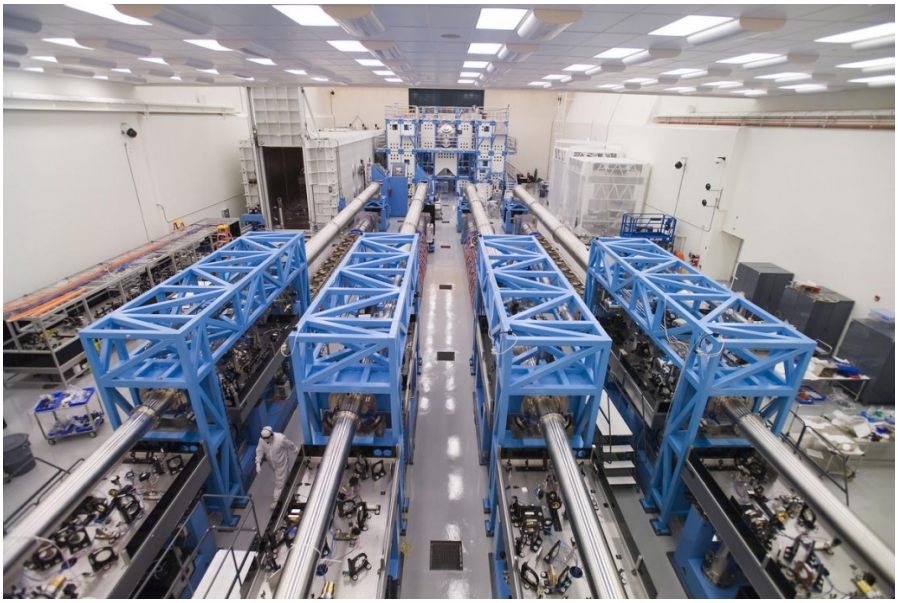

Figure 3.1: A view of the OMEGA EP beamlines. Figure from the Laboratory for Laser Energetics website [4].

as to study inertial confinement fusion (ICF) physics [28, 27], radiative hydrodynamics [25, 26], laboratory astrophysics [21, 22, 23, 24], and particle acceleration [16, 17].

The experiments in this dissertation were performed on two high power laser systems: the DLA project on the OMEGA EP laser and the scintillator characterization project on the T-Cubed laser.

3.1.1 The OMEGA EP laser

The OMEGA extended performance (EP) Laser System, in operation since 2008, is a petawatt-class laser system in the Laboratory for Laser Energetics at the University of Rochester [4]. It has four independent frequency-tripled, kilojoule class beamlines, two of which can be compressed for picosecond duration, petawatt power operation. The repetition rate is approximately 90 minutes for two short pulses operations and 45 minutes for alternating beamline shots.

Two OMEGA EP short pulses beamline 1 (BL1) and beamline 2 (BL2), with a wavelength of 1053 nm, can deliver energy up to 0.5 kJ at their best compression duration of 0.7 ps, 1.25 kJ in 10 ps, and 2.3 kJ in 100 ps. The peak laser intensity is above 2×10^{20} $\mathrm{W/cm^2}$, with an intensity contrast of approximately 10^{10}. The short pulses can be operated together in two configurations: 1) BL1 and BL2 propagate to two perpendicular off-axis parabolic mirrors (OAP) in the OMEGA EP target chamber; 2) two beamlines are combined to co-propagate along a single BL2 axis.

All four OMEGA EP beams can be operated for long-pulse (0.1 to 10 ns) at a wavelength of 351 nm with maximum energy up to 5 kJ delivered to individual beams. The best focus spot size is approximately 400 $\mu\mathrm{m}$ in with distributed phase plates and 100 $\mu\mathrm{m}$ without distributed phase plates.

3.1.2 The T-Cubed laser

The T-cubed (Table-Top Terawatt) laser is a CPA hybrid Ti:sapphire/Nd:phosphate glass system in the Gérard Mourou Center for Ultrafast Optical Science at the University of Michigan [5]. It is capable of delivering 8 J of energy in 400 fs (20 TW). The laser has a wavelength of 1053 nm and a focused intensity up to 3×10^{19} $\mathrm{W/cm^2}$ with the Amplified Spontaneous Emission (ASE) energy contrast of better than 10^{-5}. Before delivering to the experimental chamber, the compressed laser pulse is sent to the plasma mirror chamber, where contrast is improved by another 2.5 orders of magnitude.

Figure 3.2 shows a schematic of the T-Cubed laser system [5]. The "Mira-900" oscillator system, which is pumped by a continuous-wave (CW) green laser with an average power of 10 W, produces a 76 MHz train of 100 fs pulses operating at a wavelength of 1.053 $\mu\mathrm{m}$ and an average power of 200 mW utilizing a Kerr mode-locked Ti:sapphire laser. The short pulse train from the oscillator is sent to the stretcher, where it is stretched

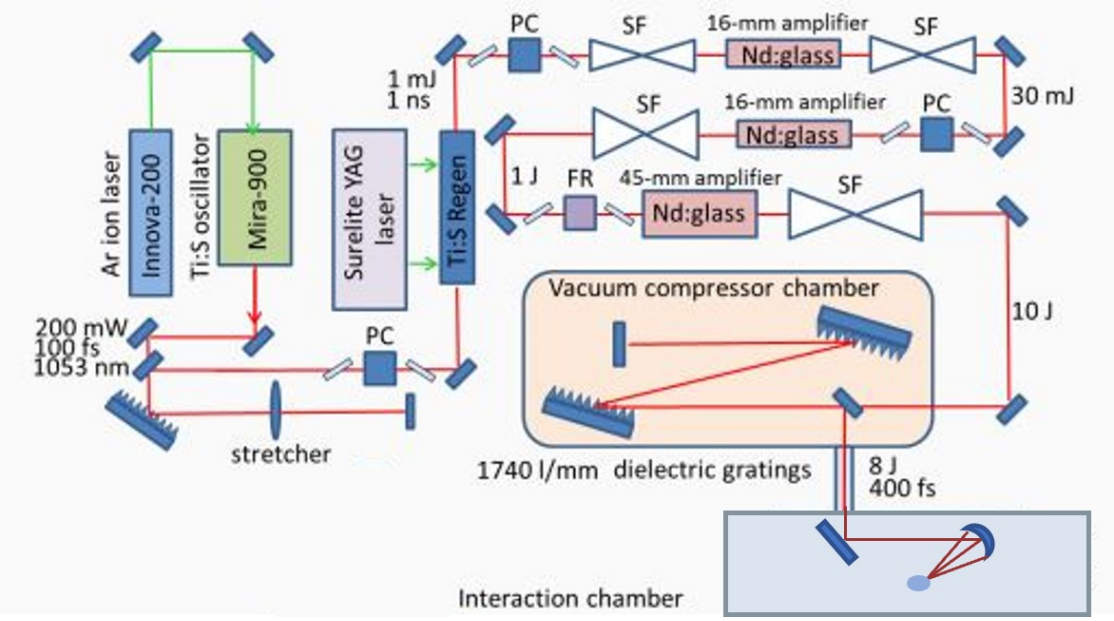

Figure 3.2: Schematic of T-Cubed laser system. Figure from the Center for Ultrafast Optical Science website [5].

out temporally by 4 passes on a single grating to approximately 1 ns. After the Pockels cell selection, the pulse is amplified in the Ti:sapphire regenerative amplifier (regen) to a 1 mJ energy level. The regen output is then further amplified in Nd:Glass amplifiers to 10 Joules. Vacuum spatial filters are installed after each amplifier for beam expansion, relay imaging, and beam smoothing. The amplified pulse is delivered to a separate vacuum compressor chamber, where it is compressed by a grating pair to a duration of 400 fs and the maximum energy is about 8 J. Finally, the output compressed beam is guided to the target interaction chamber.

In the target chamber, the pulse is focused by an OAP onto either a solid or gas target to produce high-temperature relativistic plasmas. In the past, many experiments have been successfully performed using T-Cubed laser, such as wakefield electron acceleration [117], nonlinear Thomson scattering observation [118], Coulomb explosion and ion acceleration in underdense plasma [119], proton acceleration from solid target [110],

relativistic harmonics generation [120] and many other high-field science effects discoveries. Before decommissioning in 2021, the last completed experiment on T-Cubed was to characterize the spatial resolution of plastic-based scintillators [56, 121].

3.2 Ionizing radiation detectors

Ionizing radiation detectors that are capable of detecting, identifying and measuring charged particles, neutrons and electromagnetic radiation are of vital importance in characterizing and analyzing HEDP experiments. The selection of ionizing radiation detectors for a specific interaction depends on multiple factors, such as the radiation species, detector material sensitivity, resolution, reusability, post-processing, etc. Common detectors used in laser-plasma interactions include CR-39, radiochromic film, image plate and scintillators. When ionizing radiation interacts with the sensitive material constituting the detectors, the energy transfer and deposition mechanism behind are different depending on the nature of radiation [122, 123]. Usually electrons and positrons lose energy through Coulomb collisions and radiative processes (bremsstrahlung) in matter [124, 122]. Protons and other heavy charged particles interact with matter through a number of mechanisms, including multiple Coulomb scattering, excitation, ionization and nuclear scattering. Different from the charged particles, X-rays and gamma rays, which belong to electromagnetic radiation, mainly have three types of energy-loss processes: photoelectric absorption, Compton scattering and pair production. In contrast to charged particles and x-rays, neutrons only interact with atomic nuclei through elastic or inelastic scattering, transmutation, radiative capture and fission reactions depending on the neutron energy [125, 126].

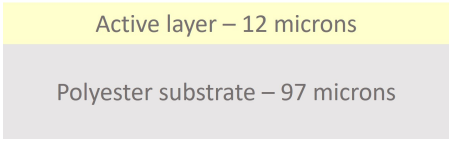

Figure 3.3: Configuration of GAFChromic HD-V2 dosimetry film.

3.2.1 Radiochromic film

Radiochromic film (RCF) is a thin plastic film consisting of a single or double active layer on a clear thin polyester substrate with a transparent coating. RCF films are designed to be able to generally detect all sorts of ionization radiations and they are insensitive to visible light. RCF can provide high spatial resolution and absolute dosimetry. The active layer contains radiation sensitive organic microcrystal monomers, marker dyes, stabilizers and other components giving the film its energy-independent response. When irradiated by the ionizing radiation, the dye in the film undergoes a photo-chemical reaction and turns from light color (transparent or light yellow) to a shade of blue. The darkness of the film reflects the quantity of absorbed radiation dose. After being scanned, an accurate radiation dose can be retrieved from the optical density.

The type of RCF we used in the experiments is the GAFChromic HD-V2 high-dose dosimetry film, which is manufactured for use with beams of photons, electrons, protons, ions and neutrons. It can resolve small features up to $5\ \mu\mathrm{m}$ and is easy to handle and process without the need of a darkroom. The structure of the HD-V2 film is shown in figure 3.3. It has an active layer with a thickness of nominally $12\ \mu\mathrm{m}$ and a polyester substrate of $97\ \mu\mathrm{m}$ thick. The dye in the active layer is light yellow without being exposed to radiation.

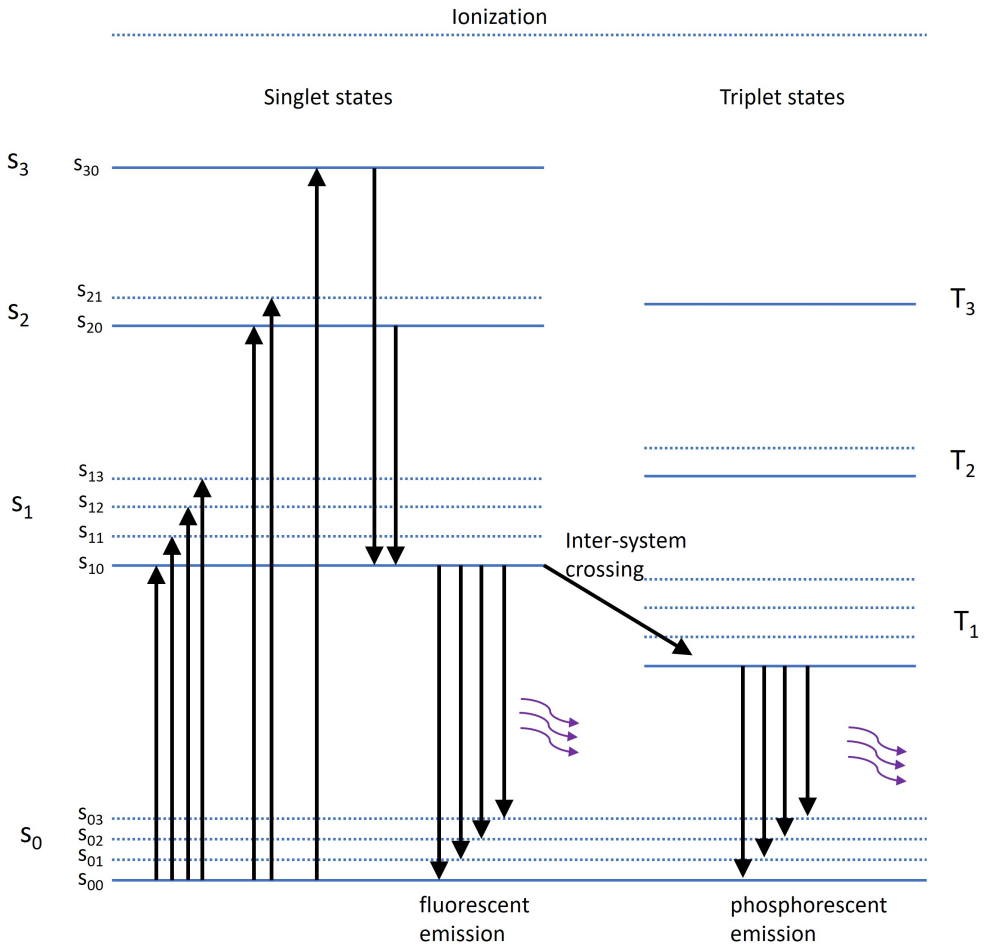

Figure 3.4: Schematic of scintillation mechanism. S_0 is the ground state. S_1, S_2, S_3 are excited singlet states. T_1, T_2, T_3 are excited triplet states. S_{00}, S_{01}, S_{10}, S_{11} etc. are vibrational sublevels. Figure based on Ref [6].

3.2.2 Scintillator

Scintillators are materials that exhibit luminescence when excited with ionizing radiation. Compared to typical detectors such as CR-39 or RCF films which are both single use detectors, one of the most notable advantages of scintillators is that they are multi-use and particularly appropriate for high repetition rate extremely high power systems. There are copious types of scintillators, and based on the material, scintillators can be divided into two basic categories: organic and inorganic. The scintillation mechanism of inorganic scintillators, which are usually crystals grown in high temperature furnaces, rely on their crystalline structure or impurity activators. While the organic scintillators are primarily due to the molecular structure of the material [6, 123]. A schematic of a Jablonski energy diagram can be used to explain the mechasnism of a typical organic scintillator, which is shown in figure 3.4. The S_0 is the ground state, consisting of several vibrational sublevels, expressed by S_{0x}, where the subscript x refers to one of the vibrational levels. The S_1, S_2, S_3 represent excited singlet electronic states associated with sub-levels and T_1, T_2, T_3 represent excited triplet electronic states. When a charged particle or x-ray comes into the scintillator, it deposits energy into the material. Electrons in the scintillation material will gain this energy and become excited. Electrons will jump from the ground state to one of the excited vibrational states in S_1, S_2 or S_3 within a time scale of order 10^{-15} s. After being promoted to a non-equilibrium state, electrons will rapidly fall to the lowest excited state S_{10} in a time scale of $10^{-12} - 10^{-9}$ s through vibrational relaxation or internal conversion. Then the electrons de-excite from S_{10} state to one of the S_{0x} states and at the same time photons are emitted, which is known as fluorescence. This process could last for hundreds of picoseconds to several nanoseconds. The emitted photon can be detected by a CCD camera and be used to characterize the properties of the incoming ionizing radiation. In addition to internal

PROPERTIES	**EJ-204**	**EJ-212**	**EJ-228**
Light Output (% Anthracene)	68	65	67
Scintillation Efficiency (photons/1 MeV e-)	10400	10000	10200
Wavelength of Maximum Emission (nm)	408	423	391
Light Attenuation Length (cm)	160	250	-
Rise Time (ns)	0.7	0.9	0.5
Decay Time (ns)	1.8	2.4	1.4
Pulse Width, FWHM (ns)	2.2	2.7	1.2
No. of H Atoms per cm^3 (x1022)	5.15	5.17	5.15
No. of C Atoms per cm^3 (x1022)	4.68	4.69	4.69
No. of Electrons per cm^3 (x1023)	3.33	3.33	3.33
Density (g/cm^3)	1.023	1.023	1.023
Polymer Base	Polyvinyltoluene		
Refractive Index	1.58		
Softening Point	75°C		
Vapor Pressure	Vacuum-compatible		
Coefficient of Linear Expansion	7.8×10^{-5} below 67°C		
Light Output vs. Temperature	At 60°C, L.O. = 95% of that at 20°C No change from -60°C to 20°C		
Temperature Range	-20°C to 60°C		

Table 3.1: Properties for EJ-204, EJ-212, and EJ-228 scintillators. Table adapted from Ref [10, 11].

conversion, there is a minor chance for electrons to de-excite from high energy singlet states to a triplet state, a process referred to as inter-system crossing. As electrons relax to their ground states, phosphorescent emission occurs, which occurs on a time scale of 10^{-3} s.

The scintillators we characterized in the T-Cubed experiment (see Chapter 5) are EJ-204, EJ-212, and EJ-228 with different thicknesses, which are commercially available plastic-based scintillators manufactured by the Eljen Technology company [10, 11]. They all exhibit wide temperature tolerance, ranging from $-20°\mathrm{C}$ to $60°\mathrm{C}$, and emit light with a maximum wavelength around 400 nm. To accommodate various requirements, each type has its unique properties. The EJ-204 is characterized by high scintil-

lation efficiency, high response speed, short light attenuation length and low background noise [11]. The EJ-212 is specifically formulated for use in thin sheets with a thickness of less than 5 mm. It could have applications in industrial and health physics measurement of alpha, beta, gamma, and neutron radiations as well as medical instruments [11]. The EJ-228 is designed specially for very fast timing applications and particularly suitable for high count rates situations [10]. Other main properties of each scintillators are listed in table 3.1.

3.2.3 Image plate

The image plate detectors are another film-like radiation image sensor, comprised of a phosphor layer which could store radiation energy until scanned by a laser beam. The type of image plate used in EPPS diagnostic for OMEGA EP experiment is Fuji BAS-SR. It contains a $\sim 100\ \mu\mathrm{m}$ thick phosphor layer of $\mathrm{BaFBr:Eu^{2+}}$ compound, which has high luminescence efficiency, and a $\sim 8\ \mu\mathrm{m}$ thick layer of mylar to protect the phosphor [127, 128]. The working mechanism of image plate relies on photo-stimulated luminescence (PSL) [129, 127, 7]. When exposed to ionizing radiation, the incident energy raises the europium ions to a excited state. Then the ions promptly loss part of the energy and slip to a metastable state, forming a latent image in the image plate. The stored information can be released by the irradiation of a laser with appropriate wavelength of 630-680 nm, such as He-Ne laser. The europium ions are excited to a higher state, which is not metastable, then they return to the ground state. Concurrently the decay of ion emits blue-purple light (390-400 nm). The PSL is collected into a photomultiplier tube and is converted to electrical signals, which can be digitized and processed for storage and display. And the detected photon number is proportional to the amount of energy deposited in the sensitive layer. After scanning, the residual latent

image on the image plate will be erased by exposing the film to bright fluorescent light, and the screen will be ready for re-use in new diagnostics.

The absolute responses of the image plates for different ionizing radiation types have been precisely calibrated. By using hot electrons with energy range between 100 keV and 4 MeV to irradiate the image plate, Chen *et al.* [130] found the PSL intensity has a nonlinear response to the electron energy. And because the detection sensitivity varies with both radiation sources and image plate types, the PSL needs to be separately calibrated for each image plate.

3.3 Diagnostics

Diagnostics capable of monitoring the laser-plasma interactions and measuring the output particles and radiation are essential for high-energy-density physics research. General methods for characterizing plasma features, electric and magnetic fields, and beam properties that will be used for this thesis work are discussed in this section.

3.3.1 Electron Positron Proton Spectrometer

The Electron Positron Proton Spectrometer (EPPS) is a permanent magnet-based charged particle spectrometer (designed by LLNL [131]) mounted in a Ten-Inch Manipulator (TIM) frame, which can be inserted into the OMEGA EP target chamber. Figure 3.5 shows the schematic of the EPPS diagnostic assembly and its mechanism. The spectrometer assembly is constructed of a steel box containing permanent magnets, providing a nearly uniform magnetic field. Two magnetic field strengths are available, a high field of 0.8 Tesla and a low field of 0.3 Tesla. There is a narrow slit with a width of one or a few millimeters on the front side, allowing particles to enter the spectrom-

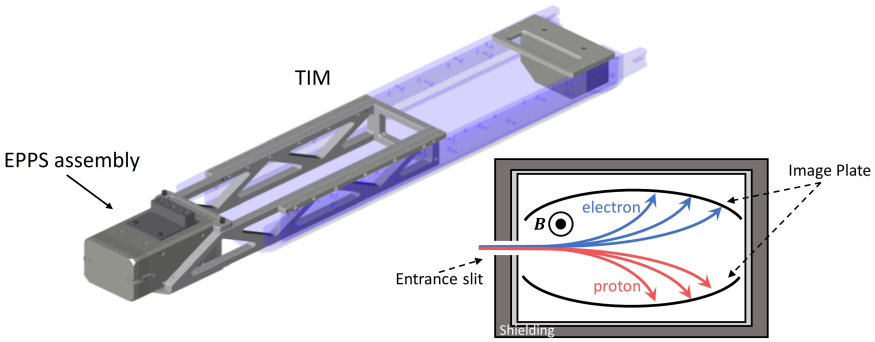

Figure 3.5: Left: TIM-deployed EPPS diagnostic assembly. TIM designed from [4]. Right: a schematic of the EPPS mechanism.

eter. The charged particles will be dispersed by the magnetic field according to their kinetic energy. The motion of a charged particle in a magnetic field is described by the relativistic equation of motion, $\frac{\partial}{\partial t}(\gamma m \mathbf{v}) = q\mathbf{v} \times \mathbf{B}$, where γ is the Lorentz factor, m is the particle mass, q is the particle charge, $\mathbf{v}$ is the particle velocity, and $\mathbf{B}$ is the magnetic field. In a uniform magnetic field, the particle will move along the gyroradius $r_G = \gamma m v_\perp / qB$, where $v_\perp$ is the velocity component perpendicular to the magnetic field. Two curved image plates are used as detectors to collect spectral data, one for positively charged particles and the other for negative. The image plates are protected by $129\ \mu\mathrm{m}$ Mylar filters. The low-energy particles move along small radius and will hit the image plate close to the entrance while high-energy particles will end up at the far end. The particle energy conversion from deflection distance follows a nonlinear function and the energy resolution is usually lower for high energy particles, which have reduced deflections. The energy resolution of the spectrometer is determined mainly by a combination of the adjustable slit width, distance to the beam source, and the intrinsic resolving capability of the detector [131].

3.3.2 Proton radiography

Proton radiography is a valuable and widely used technique to measure quasi-static electromagnetic fields generated in high-energy-density physics (HEDP) experiments [115]. The proton beam source can be generated either by fusion products in a D^3He implosion [132], providing monoenergetic beams (14.7 MeV D^3He protons and 3 MeV DD protons), or by target normal sheath acceleration, providing multi-energetic protons with maximum energy up to several tens of MeV [115, 107]. The laser-driven TNSA proton beams are characterized by small effective virtual source size, short emission times, and broad energy spread, which means that the spatial and temporal resolution of the imaging can be very small ($\sim 10\ \mu\mathrm{m}$). With these advantages, TNSA proton beam is often used to record the time and spatial evolution of transient fields in laser produced plasma experiments, such as magnetic reconnection [22], shock front propagation [133], inertial confinement fusion [134], plasma density gradients [135], and laser-plasma instabilities [50]. Protons emitted from the source, propagate to the main interaction of interest, where the local electromagnetic fields deflect the protons, altering the trajectories such that an image forms in the far-field detected proton profile. Different energy protons will travel through the interaction area at different times because they propagate at different velocities. Higher energy protons with fast speed reach the interaction area earlier than those lower energy protons. A detector stack with aluminum filters between each two detector sheets record the deflected proton beam. The aluminum filters with different thicknesses will stop protons at different energy ranges, defining the energy bins that each RCF layer is sensitive to. The high energy protons will be detected at the back of the stack, showing interaction at the early time. Hence, from back to front, the RCF layers show the temporal evolution of the interaction. Depending on the requirement of imaging resolution and operation rate, the proton detectors can be Columbia Resin No.

39 (CR39), radiochromic film (RCF), or scintillators. This diagnostic was employed in experiments performed on the OMEGA EP experiment where we use a picosecond pulse and a $50\ \mu\mathrm{m}$ thick copper as the proton source and RCF films as detectors.

3.3.3 Thomson parabola ion spectrometer

A Thomson parabola ion spectrometer is a device used to measure the energy spectra of ions with different charge to mass ratios. The idea of the mass-spectrometer was firstly proposed by J. J. Thomson in 1911 [136], and then is widely used for measuring charged particles produced from laser plasma interactions [137, 138, 139, 140, 141] or in fusion research [142, 143]. The operation principle of the Thomson parabola spectrometer is schematically shown in Figure 3.6. The main part of the Thomson parabola is made up with two parallel permanent magnets, which can provide a nearly uniform magnetic field between them, and a pair of electric field plates. The electric field plates are inserted inside the magnets and are connected to a standard commercial high voltage power supply. To use the Thomson parabola, a voltage is applied across the two plates, an electric field is set up in the gap between, which is parallel to the magnetic field. When a charged particle travels into the electric and magnetic fields, its trajectory will be drifted both in the direction parallel to the electric/magnetic field, due to the electric field, and in the direction perpendicular to the magnetic field and its initial moving direction, due to $\mathbf{v} \times \mathbf{B}$ force. For different ion species, the different charge-to-mass ratios will separate the trajectories into separate curves. An ion detector, which was a microchannel plate coupled to a phosphor screen in our experiment performed on T-Cubed laser, is placed behind the magnets at a certain distance. Usually, a certain number of neutral particles are also generated in interactions owing to the recombination effect. These neutral particles are not affected by the electric or magnetic fields, so they

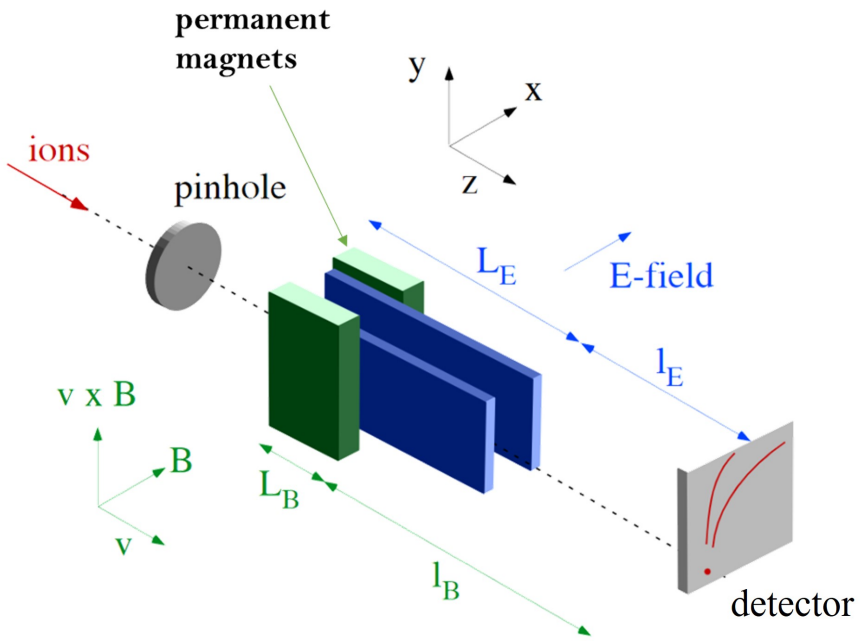

Figure 3.6: A schematic of the Thomson parabola ion spectrometer. The permanent magnets are shown in green and the electric plates are shown in blue. Figure reproduced from Ref [7].

strike the detector at a point along the direction they move in, which is called "neutral point" or "straight through". An ion beam with an energy spread forms a curve on the detector and the high energy end is closest to the neutral point because higher energy ions move faster and pass through the fields in a shorter time, meaning they are less deflected. The deflection distance from the neutral point is used to retrieve the ion energy. Besides, a pinhole is set in front of the spectrometer to restrict the number of ions entering and improve the energy resolution.

To more explicitly illustrate the principle of a Thomson parabola spectrometer, consider an ion traveling through the pinhole into the electric and magnetic fields in the frame of figure 3.6 [7]. The ion has a mass of Am_u, where m_u is the atomic mass unit, a charge to mass ratio Z/A, velocity v and kinetic energy $E_K = \frac{1}{2}Am_uv^2$. The initial ion velocity is along positive z-direction. The electric field **E** and magnetic field **B** are only in the x-direction. The dimensions of **E** and **B** are as follows: L_E and L_B give the length of the electric and magnetic fields respectively and l_E and l_B are the electric and magnetic drift length (the distance from the exit of the electric field plates and magnets to the detector plane). The charged particle motion in **E** and **B** fields follows the equation of:

$$\frac{d(Am_u\mathbf{v})}{dt} = Ze(\mathbf{E} + \mathbf{v} \times \mathbf{B}). \tag{3.1}$$

Solving equation 3.1 gives us an analytical solution for the shapes of the ion tracks. In the detector plane, we will see particle deflection in two directions, a deflection in x-direction due to the electric force and a deflection in y-direction derived from $\mathbf{v} \times \mathbf{B}$

force. The deflection distances are:

$$\begin{aligned} x &= \frac{ZeEL_E}{2E_K}[\frac{L_E}{2} + l_E], \\ y &= \frac{ZeBL_B}{\sqrt{2Am_uE_K}}[\frac{L_B}{2} + l_B]. \end{aligned} \tag{3.2}$$

Combining above two equations give us:

$$y^2 = \frac{ZeB^2L_B^2}{Am_uEL_E}\frac{(\frac{L_B}{2} + l_B)^2}{\frac{L_E}{2} + l_E}x, \tag{3.3}$$

which is a parabolic shape. And the ion kinetic energy can be determined using equation 3.2:

$$E_K = \frac{(ZeBL_B)^2}{2Am_u}[\frac{L_B}{2} + l_B]^2\frac{1}{y^2}, \tag{3.4}$$

3.3.4 4ω optical probe

The OMEGA EP laser system has a fourth-harmonic (4ω) optical probe diagnostic to characterize spatial density profiles in a wide variety of plasmas conditions. The 4ω probe system is built using a 10 ps duration, 263 nm wavelength laser and a pack of optical systems including schlieren, shadowgraphy, interferometry, and grid image refractometry [8]. This diagnostic has excellent performance in characterizing localized channels with high spatial and temporal resolution, long-scale-length plasma over a few millimeter field of view and preformed plasma in high-intensity laser-solid target interactions [144, 145, 146]. The 4ω probe laser is seeded by a 10 ps duration, 1053 nm wavelength oscillator which is coupled to a regenerative amplifier. The pulse is then delivered to a frequency conversion system to quadruple its frequency. After that the output 4ω light with a maximum energy up to 20 mJ is focused to a spot of ~ 5 mm at the target interaction area. After propagating through the plasma, the probe beam is

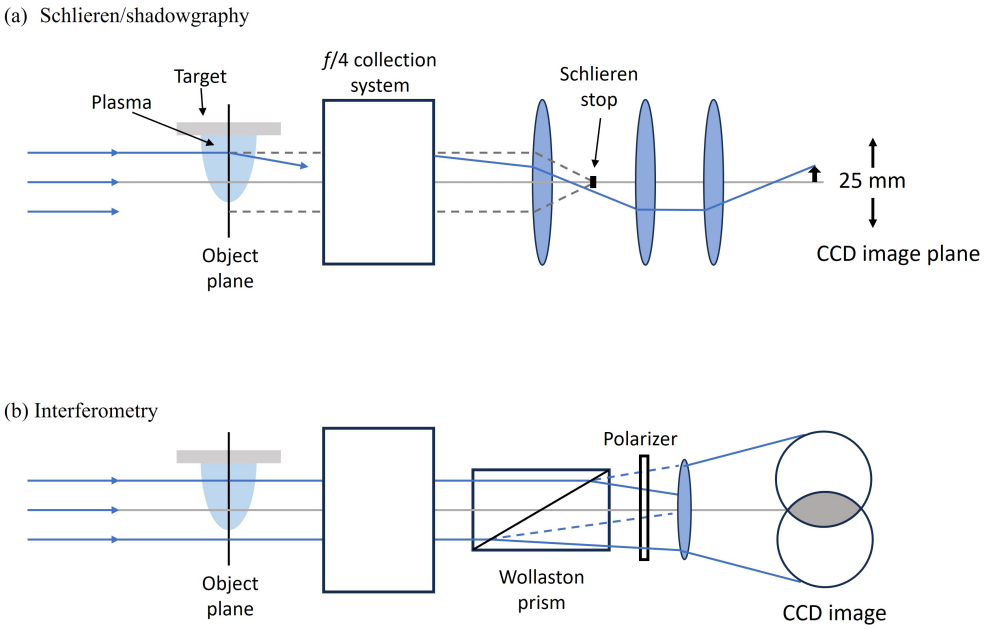

Figure 3.7: Schematics of the 4ω (a) shadowgraphy, with schlieren accommodated by blocking undeflected rays; and (b) interferometry. Based on figures from Ref [8].

collected by an $f/4$ catadioptric telescope and a transport system to relay to separate diagnostics. In our experiment, we mainly used the shadowgraphy and interferometry diagnostics, the schematics for which are illustrated in figure 3.7.

The shadowgraphy system projects the image of the plasma object plane onto the CCD image plane. The density disturbances in the interaction region refract the probe light and cast shadows. This setup can be converted to a Schlieren configuration by inserting a stop in the optical system. The shadowgraphy diagnostic is capable of resolving fine structures with a smallest size of one micrometer in the plasma. A CCD camera using a [$27\ \mathrm{mm} \times 27\ \mathrm{mm}$] 16 bit chip with 13.5 μm pixel size is employed to capture the image.

In the interferometry diagnostic, a Wollaston prism is utilized to split the probe beam into two replicas, which will then interfere with each other and form dark and light

fringes in their overlapping area. To ensure a clear interference pattern, the probe beam needs to be carefully aligned so that half of it (top half in figure 3.7(b)) illuminates the interaction region while the other half (bottom half in figure 3.7(b)) passes through the intact plasma or vacuum as a reference. The top half, which goes through phase shift as it propagates through plasma density variation region where refraction index changes, will interfere with the bottom half, which has no optical path change. To detect the plasma profile with high accuracy, the interferometry is recommended to use for underdense plasmas having an electron density typically below $10^{20}\ \mathrm{cm}^{-3}$.

3.4 Particle-In-Cell simulations

Particle-in-cell (PIC) simulation is a computational technique used to numerially model the interactions of charged particles with electromagnetic fields in a plasma. It is widely used in modeling complex and dynamic plasma systems and is particularly powerful in exploring phenomena that are often challenging to study in experiments.

In the PIC simulation frame, the macroscopic system is divided into discrete parcels, each representing a collection of particles with different weightings. These particles can be electrons, ions, or other charged species. The virtual space accommodating these particles is subdivided into a computational mesh grid, forming the canvas upon which the simulation unfolds. The driving forces – electric and/or magnetic fields – are defined at each grid point and govern the particle behavior. The evolution of the system state is advanced through the interplay of macro-particle movement and the updating of fields at discrete time steps.

Individual particle movement is driven by the Lorentz force equation, accounting for the influence of electromagnetic fields on charged particles. As particles transit across

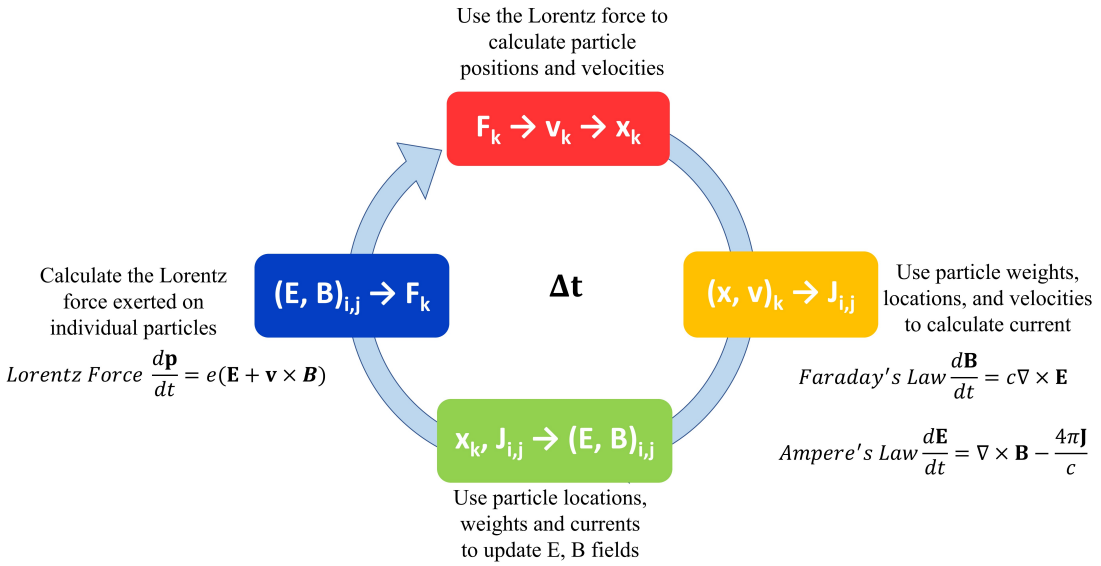

Figure 3.8: PIC code computational loop.

the grids, their trajectories are recalculated, allowing them to respond to the electromagnetic fields. Concurrently, the fields at grid points are updated to reflect the changes induced by particle motion. To update fields, the particle charge and current densities are projected onto the grid, effectively depositing these properties at nearby grid points. The particle distribution is then utilized to recalculate electric and magnetic fields through Maxwell's equation with different numerical solvers. The new fields, in turn, affect particle movement in the subsequent time step, resulting in a continuous feedback loop of the entire system.

The simulation accuracy and speed are determined by a number of factors, including particle number, grid size, and time step. To have a stable simulation environment with diminished wave dispersion due to grid size, the maximum allowable time step (Δt) is

determined by the Courant-Friedrichs-Lewy (CFL) condition:

$$\Delta t \sum_{i=1}^{n} \frac{c}{\Delta x} \ll 1, \tag{3.5}$$

where Δx is the grid interval and n is the number of dimensions. The CFL condition ensures that the time step is small enough to accurately capture the fastest waves or changes in the system, preventing numerical instability.

OSIRIS 4.0 is the PIC code used in this work. It is an open-source high-performance fully-relativistic 3D-3V (3 dimensions in both space and velocity) code, which is written by the OSIRIS consortium of UCLA and IST (Lisbon, Portugal) [147, 148]. Since the three spatial dimensional simulation is extremely expensive and time-consuming, the simulations for this thesis were run in two dimensions. The simulations were run at the University of Michigan on the Great Lakes Slurm cluster. Output files are downloaded and analyzed using Python and Matlab.

CHAPTER 4

Direct Laser Acceleration

4.1 Introduction and motivation

The rapid advancement of ultra-high power laser facilities is enabling the realization of high energy density physics experiments and exploration of next-generation plasma-based accelerators [149, 12]. As described in section 4, Direct Laser Acceleration (DLA) is one of the mechanisms capable of generating high-flux, high-energy electrons, offering the feasibility of constructing compact and cost-effective accelerators. In the DLA mechanism, electrons are able to be accelerated to hundreds of MeV by a relativistic intensity laser within the laser-driven channel that forms in an underdense plasma [39]. The electric field of the laser oscillates electrons in the transverse direction and the $(\mathbf{v} \times \mathbf{B})$ force converts transverse momentum to longitudinal momentum. The channel fields dramatically increase electron energy gain by reducing the dephasing rate and keeping electrons in phase with laser wave over an extended distance [45].

As an accessible source of high-energy electrons, DLA has the potential to drive innovations in the fields of particle physics and medical therapy, such as accelerating secondary ions/neutrons [150, 151, 152], and providing a non-invasive treatment option for cancer patients. In addition to the technical advancement, the primary motivation for

the DLA project is to serve as a bright directional x-ray source. Within the laser channel, electrons undergo betatron oscillation, emitting x-rays along the tangential direction of their trajectories. Based on the features of broad-band high-yield and high-energy, the x-ray beam has diverse applications in medical imaging [41, 93, 153, 154, 155], material science, nuclear physics [156], and high-energy physics diagnostics [157]. Furthermore, the DLA plays a vital role in understanding many laser-matter interactions under extreme conditions. The investigation of laser channel creation and the electron energy transfer mechanism promotes the study of interactions in which the DLA process occurs as accompanying processes [158]. For example, revealing the energy transfer mechanism from the driving laser pulse to the plasma electrons is essential in the context of hole boring scheme for fast ignition inertial confinement fusion, where a millimeter-scale channel is required to guide a second laser to the ignition core [68].

Previous investigations have studied the electron motion in the laser channel [39, 159], the electron energy enhancement with the assistance of channel fields [45] and the effect of laser a_0 [46] and plasma density [48] on DLA.

In this chapter, DLA experiments performed on the OMEGA EP laser are presented. The electron acceleration was optimized from multiple dimensions through running parameter scans. The investigated parameters include laser focusing condition, laser power, pulse duration, plasma peak density, and density gradient. The electron beam was found to have maximum energies exceeding 20 times the ponderomotive energy of the laser pulse under certain focusing [160], pulse energy, and plasma density profile [161]. The channel formation and evolution were imaged and recorded using the optical probe diagnostic and proton radiography. 2D particle-in-cell simulations using the code OSIRIS 4.0 were used to reveal the acceleration mechanism and the effect of different parameters on electron acceleration and channel formation.

4.2 Experimental setup

4.2.1 Laser parameters

The experiment was performed at the University of Rochester Laboratory for Laser Energetics using the OMEGA EP laser facility. The two short pulses, beamline 1 (BL1) and beamline 2 (BL2), were utilized for the DLA project. The laser pulses have a central wavelength of $1.053\ \mu\mathrm{m}$, a duration of $(700 \pm 100)\ \mathrm{fs}$ for best compression, and can be focused to a smallest in-vacuum full-width at half-maximum (FWHM) focal spot size of $\mathrm{FWHM} \approx 4\ \mu\mathrm{m}$ using an $f/2$ equivalent off-axis parabolic mirror with a square beam profile. With the best compression and full beam aperture, the maximum on-target energy is 300 J for BL1 and 500 J for BL2. The laser beam is focused onto the edge of supersonic helium gas jet targets to create plasma and subsequently interact with the generated plasma.

To optimize the DLA electron generation from multiple perspectives, we performed parameter scans for a number of factors, including plasma parameters such as peak density and density gradient, as well as laser parameters like focusing geometry, pulse duration, laser energy, etc. These parameter scans required several different configurations using BL1 and BL2 to cover a wide range of experimental settings. Both beams, for example, can be sequentially used to interact with straight-oriented gas targets to study the effect of laser focusing conditions. The laser focal spot size was adjusted by clipping the peripheral beam with circular apodizers with different diameters. The maximum spot size of $(12.2 \pm 0.2)\ \mu\mathrm{m}$ was produced using an $f/10$ apodizer. In cases where we aimed to study the effect of the plasma density gradient, the gas jet nozzles were orientated at a specific angle. Furthermore, proton imaging diagnostic was used to observe the channel formation during the interaction, so one beam (BL2) was used

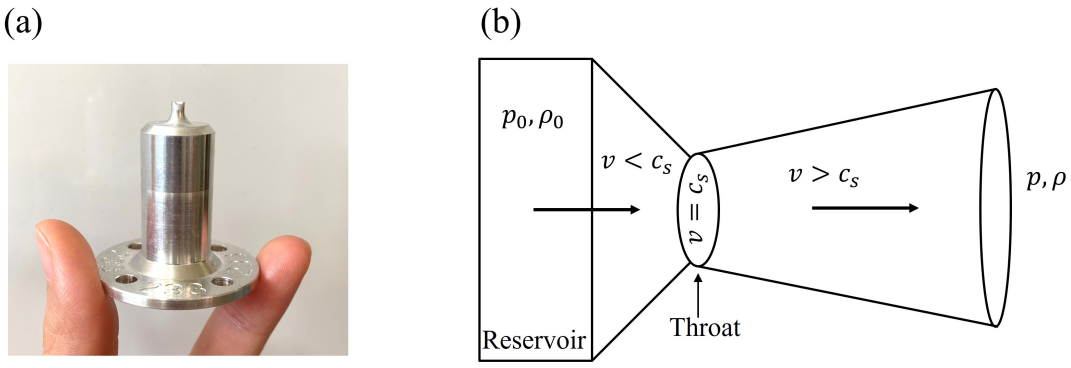

Figure 4.1: (a) Photo of a $\mathrm{Mach}\ 5 - 2\ \mathrm{mm}$ gas jet nozzle. (b) A sketch of the nozzle mechanism adapted from Ref. [9].

as the main interaction beam while the other beam (BL1) was utilized to interact with copper foils for proton generation. The details for each design are shown in the sections below.

4.2.2 Supersonic gas jet targets

A supersonic gas jet nozzle is a very useful component in high-energy-density physics experiments, serving as a fundamental tool for producing precisely controlled and highly reproducible plasma. The supersonic gas jet nozzle operates by releasing a high-pressure gas through a specially designed constricted aperture, leading to the formation of a narrow, high-velocity gas stream, with a speed typically exceeding the local speed of sound. The gas flow property is characterized by the Mach number $\mathrm{M} = \mathrm{v}/\mathrm{c_s}$, where v is the flow velocity and c_s is the sound speed. The working principle of a nozzle is shown in figure 4.1 (b). In the reservoir converging section, the gas flow is accelerated. The gas velocity reaches the speed of sound at the throat of the nozzle. Passing through the throat, the gas goes through isentropic adiabatic expansion in the diverging area with speed surpassing sound speed. After releasing from the nozzle exit, the gas has an ap-

proximately flat top density profile with a diameter equal to the nozzle exit diameter and a peak density ρ of $\rho_0/\rho = (1 + (\gamma_a - 1)M^2/2)^{1/(\gamma_a - 1)}$, where ρ_0 is the gas density in the reservoir and γ_a is the adiabatic index of the gas [9]. At a farther distance away from the exit, the gas column expands at an angle around $1/\mathrm{M}$. And the FWHM of the gas flow is approximately equal to $D = D_{exit} + 2L/\mathrm{M}$, where D_{exit} is the nozzle exit diameter and L is the distance from exit to the measuring point. The 2D plasma density profiles for Mach 2 and Mach 5 nozzles are predicted using an analytic model developed by A. M. Hansen *et al* [9]. K. McMillen and J. L. Shaw performed neutral density measurements and 2D fluid calculations [162] which provided further corrections to Hansen's model and more accurate density distributions. We have used the 2D fluid calculations to estimate the peak plasma density for our experiments.

4.2.3 Diagnostics

The interaction was monitored and measured using various diagnostics. The laser intensity at its focal plane is measured by an on shot diagnostic. The main diagnostics for the generated hot electron beam is the magnetic electron-positron-proton-spectrometer (EPPS details described in section 3.3.1) [131]. The density distribution of the plasma and the channel were detected by shadowgraphy and interferometry using an optical probe beam (detailed in section 3.3.4). And the evolution of the electromagnetic fields in the interaction area was recorded using proton radiography (see section 3.3.2).

Proton radiography package

Protons are generated through the interaction of a picosecond laser pulse with a $50\ \mu\mathrm{m}$ thick copper foil via the TNSA mechanism. The generated proton beam possesses desirable properties for imaging applications, such as a small virtual source size, well-

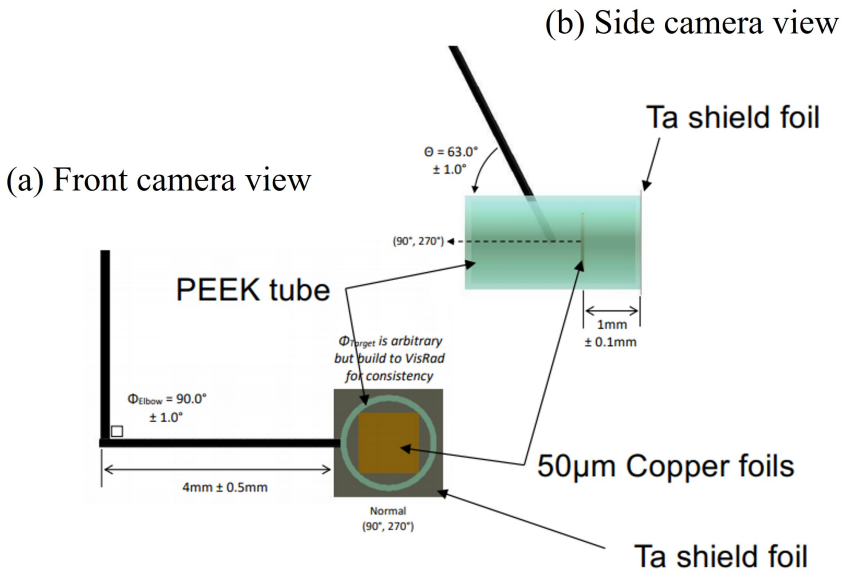

Figure 4.2: The configuration of proton generation package for proton radiography diagnostic. A $50\ \mu\mathrm{m}$ copper foil is attached inside a PEEK tube. The front side is covered by a Tantalum shield. The proton package is held by an 90° elbowed stalk in the chamber. Panel (a) and (b) demonstrate the front view and side view of the package respectively.

RCF pack 1

Material	Label
500 μm Al	
HD-V2 Film	H1
100 μm Al	
HD-V2 Film	H2
100 μm Al	
HD-V2 Film	H3
100 μm Al	
HD-V2 Film	H4
200 μm Al	
HD-V2 Film	H5
200 μm Al	
HD-V2 Film	H6
200 μm Al	
HD-V2 Film	H7
300 μm Al	
HD-V2 Film	H8
300 μm Al	
HD-V2 Film	H9
500 μm Al	
HD-V2 Film	H10
1000 μm Al	
HD-V2 Film	H11
1000 μm Al	
HD-V2 Film	H12
2000 μm Al	
HD-V2 Film	H13
2000 μm Al	
HD-V2 Film	H14
3000 μm Al	
MD-V2-55	M15

RCF pack 2

Material	Label
500 μm Al	
HD-V2 Film	H1
100 μm Al	
HD-V2 Film	H2
100 μm Al	
HD-V2 Film	H3
100 μm Al	
HD-V2 Film	H4
200 μm Al	
HD-V2 Film	H5
200 μm Al	
HD-V2 Film	H6
200 μm Al	
HD-V2 Film	H7
100 μm Al	
HD-V2 Film	H8
100 μm Al	
HD-V2 Film	H9
200 μm Al	
HD-V2 Film	H10
200 μm Al	
HD-V2 Film	H11
300 μm Al	
HD-V2 Film	H12
300 μm Al	
HD-V2 Film	H13
500 μm Al	
HD-V2 Film	H14
3000 μm Al	
MD-V2-55	M15

RCF pack 3

Material	Label
500 μm Al	
HD-V2 Film	H1
100 μm Al	
HD-V2 Film	H2
100 μm Al	
HD-V2 Film	H3
100 μm Al	
HD-V2 Film	H4
200 μm Al	
HD-V2 Film	H5
200 μm Al	
HD-V2 Film	H6
200 μm Al	
HD-V2 Film	H7
100 μm Al	
HD-V2 Film	H8
100 μm Al	
HD-V2 Film	H9
100 μm Al	
HD-V2 Film	H10
100 μm Al	
HD-V2 Film	H11
100 μm Al	
HD-V2 Film	H12
100 μm Al	
HD-V2 Film	H13
100 μm Al	
HD-V2 Film	H14
100 μm Al	
HD-V2 Film	H15
100 μm Al	
HD-V2 Film	H16
100 μm Al	
HD-V2 Film	H17
200 μm Al	
HD-V2 Film	H18
200 μm Al	
HD-V2 Film	H19
300 μm Al	
HD-V2 Film	H20
3000 μm Al	
MD-V2-55	M21

Figure 4.3: Three RCF packs used in the experiments.

collimated, and a wide energy spread. In our experiments, a proton generation package was employed and its configuration is shown in figure 4.2. The Cu foil was installed in a PEEK tube and shielded from scattered light and radiations from the interaction area by a 5 μm thick Ta foil on the front side, which faced the interaction area. The whole assembly was held by a TIM with an elbowed stalk to prevent the stalk from obstructing the optical probe. The Cu foil was positioned 8 mm from the interaction. The BL1 with a focal spot size $\sim$ 4 μm and an energy of 150 J was focused onto the Cu foil to produce protons. When the high-energy protons travel through interaction regions with varying electromagnetic fields, their trajectories are deflected due to the Lorentz force. The strength and direction of the electromagnetic fields determines the extent of the deflection for protons with different energy.

To detect protons within different energy bins, which reflect interaction at different times, we placed a radiochromic film (RCF) pack, consisting of multiple RCF sheets separated by aluminum filters with varying thicknesses, at 8 cm from the interaction center. Three RCF pack configurations were used and the compositions are listed in tables in figure 4.3.

4.3 Effects of the laser focusing geometry

The electron energy was found to significantly change when the laser focal spot size was adjusted in experiments. Previous simulations performed by our collaborators K. Tangtartharakul *et al.* [85] demonstrated that increasing the focal spot size to approximately the same as the channel width can enhance energy coupling efficiency for a fixed laser peak power. Counter-intuitively, raising the laser peak intensity by focusing the beam to a smaller spot does not lead to higher electron energy. This energy increase with in-

creased spot size is due to the fact that the wavefront is less curved for the larger focal spot, hence the negative work done by the longitudinal component of the laser electric field is reduced [163]. Furthermore, Babjak *et al.* find an analytical prediction for the optimal focal spot, which approximately matches the electron transverse resonant amplitude, for laser powers of 1-Petawatt and higher over a range of plasma densities [164]. Similar studies about the impact of laser focusing geometry have been performed in the laser wakefield acceleration (LWFA) regime. A laser with a spot size larger than the plasma wavelength and a pulse duration $\tau \times c$ shorter than a plasma wavelength maintains high intensity and self-guides in the plasma, allowing the acceleration of monoenergetic electron bunches [165]. However, the recent work in the DLA regime were all based on theoretical research, we still lack explicit experimental evidence showing the effect of laser focusing geometries on DLA. To fill this gap, we conducted a series of experiments to scan different laser focusing conditions. And the results of this work are being summarized and are in preparation for a journal publication [160].

4.3.1 Experimental setup

Fig. 4.4(a) shows the schematic of the setup. A best-compressed laser pulse with a duration of (700 ± 100) fs was focused by an $f/2$ equivalent off-axis parabolic mirror to the edge of a 2 mm diameter supersonic helium gas jet target. The target gas backing pressure was varied to achieve a range of peak plasma densities (n_0) between $0.008\ n_c$ to $0.06\ n_c$, where n_c is the critical density. The default near-field beam profile is square. To change the effective f-number of the beam, circular apodizers with different diameters were used so that the full-width at half-maximum (FWHM) focal spot size in vacuum varied from $(4.6 \pm 0.5)\ \mu$m to $(12.2 \pm 0.2)\ \mu$m. The on-shot wavefront was measured and the vacuum focal plane was reconstructed. However, the increase of the beam size was

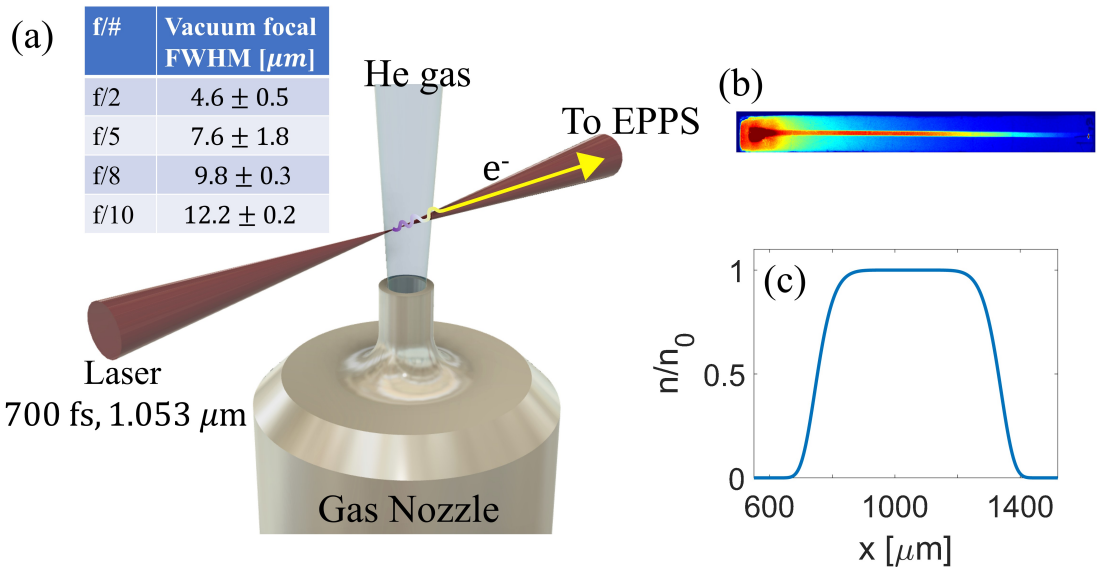

Figure 4.4: (a) Experimental setup. The inset table shows four f-number for different apodizers and their corresponding in-vacuum laser FWHM. (b) Raw electron spectrometer image. (c) The longitudinal density profile that is employed in simulations. n_0 is the peak plasma density, which is in the range of $0.008\ n_c$ to $0.06\ n_c$.

realized by clipping the beam before focusing, leading to a reduction of the maximum possible on-target energy, hence limiting the obtainable a_0 for large focal spots. The range of peak vacuum intensities were $(0.15\text{–}10.7) \times 10^{20}\ \mathrm{Wcm}^{-2}$, corresponding to an a_0 range of 3.4 to 30. The electron beam energy spectrum was measured along the laser axis by a magnetic EPPS [131]. An example of the raw electron spectrum on an image plate is shown in Fig. 4.4(b).

4.3.2 Particle-in-cell simulation

To model the interaction, 2D PIC simulations were performed using the OSIRIS 4.0 code [147, 148] (detailed in section 3.4). A $[750\ \mu\mathrm{m} \times 200\ \mu\mathrm{m}]$ moving window with a resolution of 50 cells per λ in longitudinal (x) direction and 35 cells per λ in transverse (y) direction moving in the speed of light was utilized. Each cell has 4 electrons and 4

fully ionized mobile helium ions. An open boundary condition was applied to both dimensions. To approximate the density distribution of a gas jet nozzle, the initial plasma density has a super-Gaussian profile in x-direction, with a $450\ \mu\mathrm{m}$ flat top area and two $150\ \mu\mathrm{m}$ ramping zones connecting to the vacuum as shown in Fig. 4.4(c), and a uniform distribution in y-direction. The maximum plasma density n_0 along the laser propagation axis was $0.01\ n_c$, where $n_c = \epsilon_0 m_e \omega^2 / e^2$ is the critical plasma density and ω is the laser frequency. The laser pulse was linearly polarized in y-direction with $a_0 = 3.5$, a wavelength of 1.053 nm and a pulse duration of $\tau = 700$ fs. It was launched from the vacuum region and focused at $n_e = 0.95 n_0$. The initial laser electric field has a Gaussian spatial profile and a temporal form of $E = E_0 \sin(\pi t/\tau)$, where τ is the pulse duration. Three different focal spot sizes with FWHM $= 5\ \mu\mathrm{m},\ 8\ \mu\mathrm{m}, \text{and } 16\ \mu\mathrm{m}$ were examined. And since the energy is changing for different focusing conditions, another set of simulations using a constant laser energy of 8.3 J, which is set based on the energy of the $8\ \mu\mathrm{m}$ beam ($a_0 = 3.5$), were also performed.

4.3.3 Data and analysis

Experimental data and simulation results

The highest electron energy and highest mean energy under the experimental conditions were achieved using a beam with moderate focal spot size. Fig. 4.5 shows seven example experimental electron energy spectra from different laser focal spot sizes at a plasma density of $(0.016 \pm 0.004)\ n_c$. The apodization of the beam to create the different focal spot sizes means the pulse energy was restricted for the large focal spot sizes, resulting in a wide range of $a_0 = 4$ – 26. For a laser focal spot of $\mathrm{FWHM} = 8.3\ \mu\mathrm{m}$, a bi-Maxwellian-like electron energy distribution extending to 400 MeV was observed,

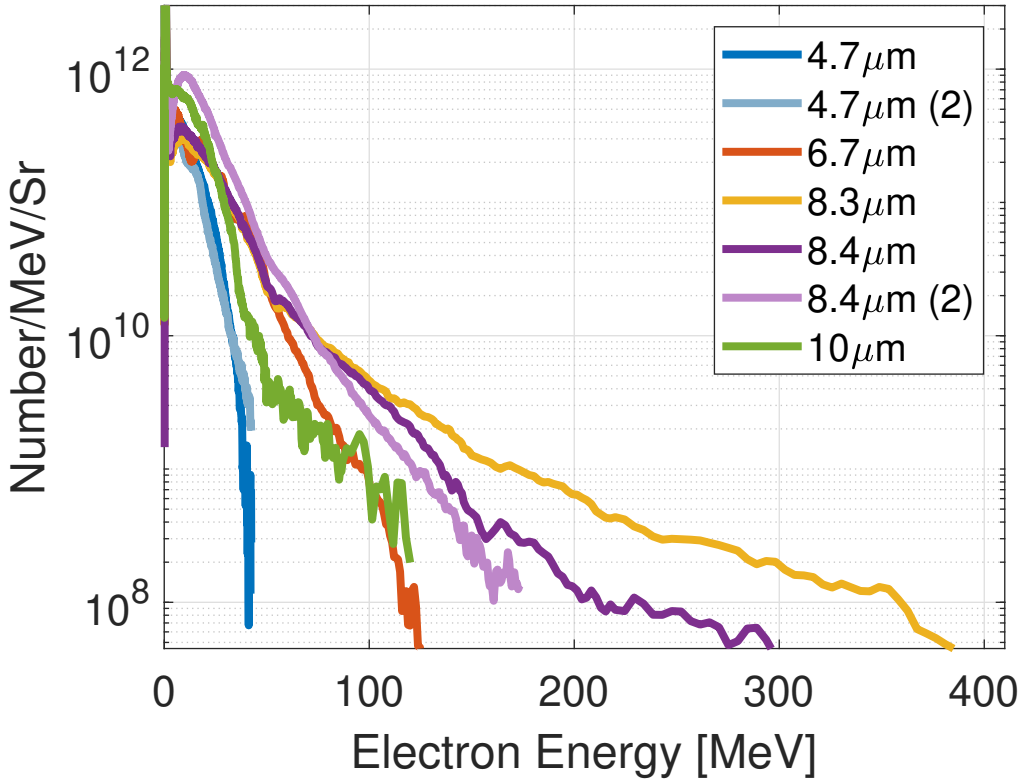

Figure 4.5: Electron spectra for different laser focal spot sizes with similar peak plasma density of $(0.016 \pm 0.004)\ n_c$. The light blue curve, labeled as $4.7\ \mu\mathrm{m}\ (2)$, is a repeat shot of the dark blue shot. The light purple curve, labeled as $8.4\ \mu\mathrm{m}\ (2)$, is a repeat shot of the dark purple shot. The laser a_0 varies for different laser focusing conditions. From small beam size to large beam size, the laser a_0 = 27 (FWHM = $4.7\ \mu\mathrm{m}$), 7.8 (FWHM = $6.7\ \mu\mathrm{m}$), 9 (FWHM = $8.3\ \mu\mathrm{m}$), 10.3 (FWHM = $8.4\ \mu\mathrm{m}$) and 5.7 (FWHM = $10\ \mu\mathrm{m}$).

which exceeds 20 times the ponderomotive energy of the laser pulse High energy tails exceeding 50 MeV are obtained for laser focal spot size within the range of $6.7\ \mu\mathrm{m}$ to $10\ \mu\mathrm{m}$. The significant energy increase upon using a moderate-sized beam suggests there is an optimal laser focusing condition. Due to constraints in experimental time, only two shots – one with a laser beam size of $4.7\ \mu\mathrm{m}$ (dark blue curve in figure 4.5) and another with $8.4\ \mu\mathrm{m}$ (dark purple curve in figure 4.5) – were repeated to check the reproducibility. Both repeated shots show minor shot-to-shot variations. The $4.7\ \mu\mathrm{m}$ shot and its repeat shot almost overlap, with mean electron energies of 16.6 MeV and 16.8 MeV, respectively, showing a difference of 0.2 MeV. The repeat of the $8.4\ \mu\mathrm{m}$ shows a slightly larger gap. The mean energies for the $8.4\ \mu\mathrm{m}$ shot and its repeat shot are 28 MeV and 23 Mev respectively, with a difference of 5 MeV.

To better extract the energy variation trends, data over a large parameter space – density, focal spot size, laser power – was collected and the results are summarized in Fig. 4.6. The data is divided into similar laser power, illustrated by the different colors – (30 ± 1) TW (green), (50 ± 5) TW (blue) and (160 ± 2) TW (red) – and the darkness of color indicating the mean electron energy. The mean electron energy was calculated for electrons above 10 MeV. For each laser power, maximum electron mean energies above 25 MeV were measured. However, due to the fact that changing the laser focal spot will inevitably change other parameters, such as laser intensity for a fixed laser energy or power, it is difficult to directly separate the individual effects of the laser focusing geometry. Therefore, to understand the complex relationship between the laser focusing geometry and the electron acceleration, we perform two-dimensional PIC simulations with either constant laser power or constant peak intensity. This allows us to explicitly analyze the electron collective behavior and single particle dynamics. In simulations, the final spectra of escaping electrons are diagnosed outside of the

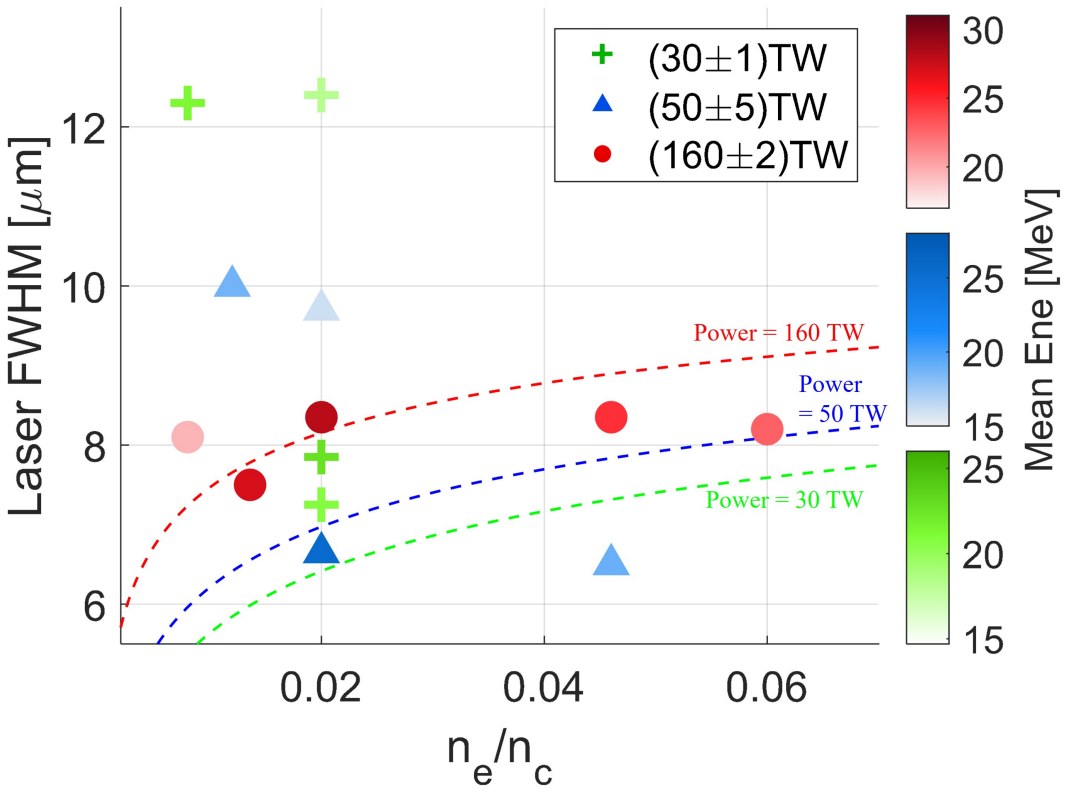

Figure 4.6: The scattered markers show the experimental data in the [laser FWHM – plasma density] domain. Green plus markers are obtained using laser power of (30 ± 1) TW, blue triangles are obtained using laser power of (50 ± 5) TW and red dots are obtained using laser power of (160 ± 2) TW. The color darkness indicates the electron mean energy, with darker color representing higher energy.
The dashed curves show the theoretical prediction of the optimal conditions for electron acceleration, which is calculated based on the assumption of electron transverse displacement matching with laser beam size. The green, blue and red color correspond to laser power of 30 TW, 50 TW, and 160 TW respectively.

plasma, as the laser entirely leaves plasma at $t = 3.8$ ps. The results of simulations using a constant $a_0 = 3.5$ (corresponding to power of 5 TW, 12 TW, 47 TW for laser FWHM $= 5\ \mu\mathrm{m},\ 8\ \mu\mathrm{m}, \text{and } 16\ \mu\mathrm{m}$) or constant laser power of 12 TW (corresponding to a_0 of 5.6, 3.5, 2 for laser FWHM $= 5\ \mu\mathrm{m},\ 8\ \mu\mathrm{m}, \text{and } 16\ \mu\mathrm{m}$) are shown in Fig. 4.7 (a) and (b) respectively. Enhanced acceleration is obtained using an $8\ \mu\mathrm{m}$ beam in both cases. And the improvement of electron number is more dramatic in Fig. 4.7 (b) where a fixed laser power is utilized. In addition, due to a low peak laser intensity, the mean energy of a $16\ \mu\mathrm{m}$ beam is lower than that of a $5\ \mu\mathrm{m}$ beam in the constant power simulation.

The 2D simulations provide insight into the influence of laser focusing on the laser field evolution, which is directly related to the channel formation and electron energy gain threshold. Since both simulation groups (a fixed a_0 group and a fixed power group) show the same trend, the details from one group (fixed a_0) are used to demonstrate the difference Fig. 4.7 (c) shows the temporal evolution of the laser a_0 (dashed lines) and the corresponding electron mean energy (solid lines) for three focusing geometry. The center of the laser pulse arrives at the initialized vacuum focal plane of $x = 800\ \mu\mathrm{m}$ at $t = 1.1$ ps. Then it propagates in the peak density region until $t = 3$ ps, and finally the entire laser leaves the plasma at $t = 3.8$ ps. In the density up-ramp region, a tight initialized focus reaches peak intensity faster than a large beam. As shown in Fig. 4.7 (c), the peak a_0 for a $5\ \mu\mathrm{m}$ beam appears around 1.1 ps, corresponding to $10\ \mu\mathrm{m}$ before the vacuum focus position in the spatial domain, while a $16\ \mu\mathrm{m}$ beam reaches its peak intensity at $t = 1.5$ ps, which is roughly $100\ \mu\mathrm{m}$ after the vacuum focus point. The $5\ \mu\mathrm{m}$ beam reaches its maximum a_0 with a tiny focal spot at a low density position resulting in a narrow channel and a high ponderomotive force. Hence the channel is more thoroughly evacuated and fewer electrons are available to be injected into the

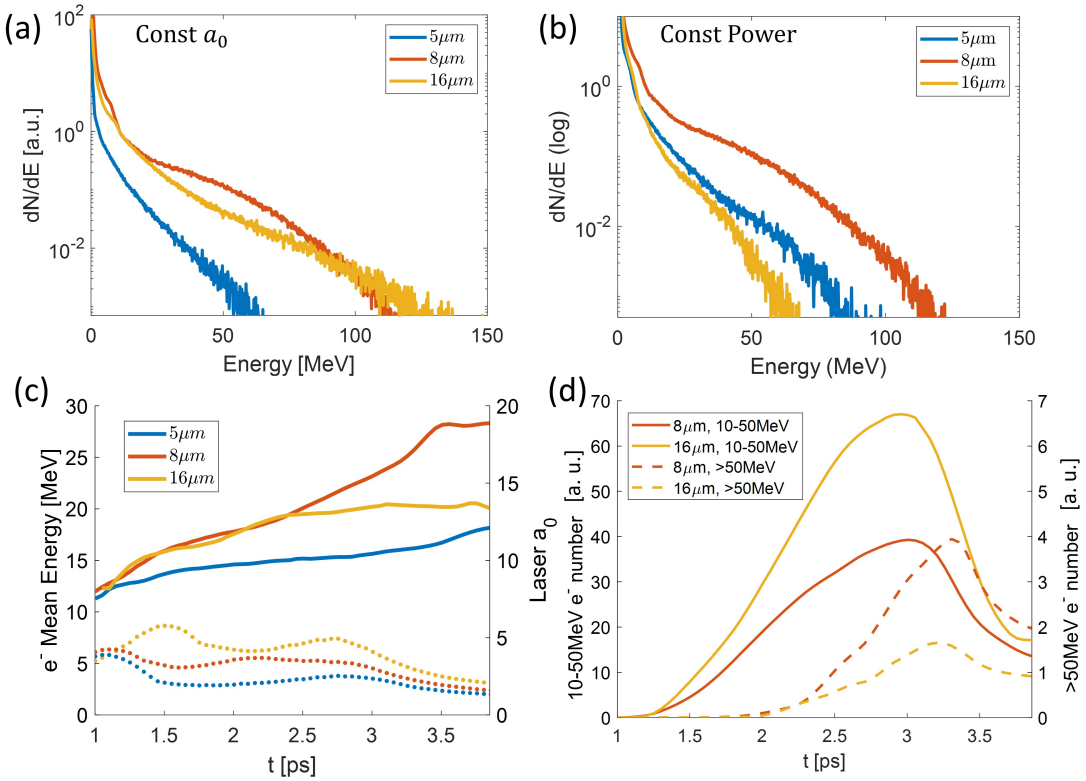

Figure 4.7: Simulated electron energy spectra for different initial focal spot sizes shown at $t = 3.8$ ps using (a) constant laser a_0 and (b) constant laser power. (c) Temporal variation of laser a_0 (dash lines) and the corresponding mean energy of electrons above cutoff energy of 10 MeV (solid lines) from the same simulation sets of the panel (a). (d) Comparison of temporal variation of accelerated electron number for 8 μm and 16 μm beams from constant laser a_0 simulations. The solid lines represent electrons in the energy range of 10–50 MeV and the dashed lines represent high-energy electrons > 50 MeV.

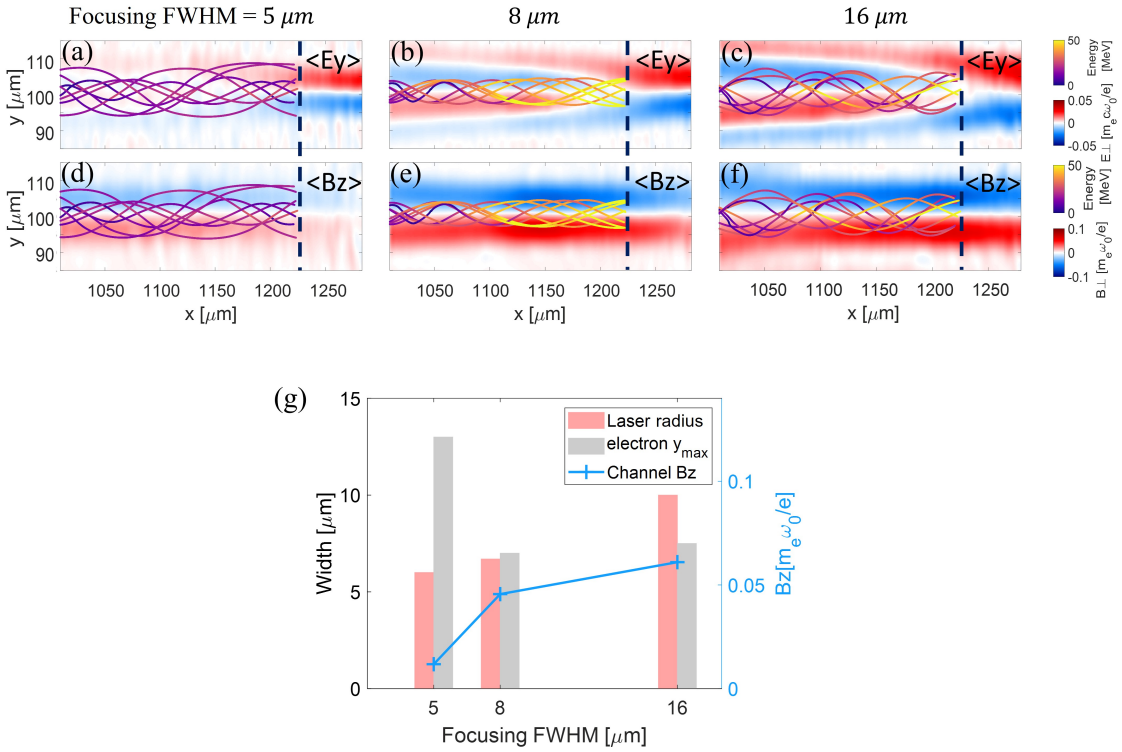

Figure 4.8: Electron trajectories overlapping on the instantaneous channel transverse electric field E_y (top row) and azimutral magnetic field B_z (second row) at $t = 2.86$ ps for laser beam size of 5 μm, 8 μm and 16 μm. The channel fields are temporally averaged over one laser cycle. Panel (g) shows the laser radius, the electron maximum oscillation from the channel axis, and the amplitude of channel B_z fields at the position of $x = 1225$ μm.

channel, leading to weak currents and consequently weak self-generated magnetic fields, as shown in Fig. 4.8 (a).

After passing the focal plane, a small beam also rapidly defocuses and the a_0 is relatively low for the remaining interaction period. The low laser intensity limits the maximum energy that electrons could gain. In contrast to the tight focusing geometry, we see a more stable a_0 for an 8 μm beam. This moderate-sized beam creates a wider channel and more electrons with slightly higher peak longitudinal momentum are injected into the channel, rapidly forming strong currents. After passing the vacuum focal plane, the

laser defocuses to $a_0 = 3$ at $t = 1.6$ ps, then self-focuses to $a_0 = 3.5$ at $t = 1.8$ ps. The a_0 is sustained until it moves to the density down-ramp area. This allows the electron mean energy to increase with a relatively constant slope.

As the beam diameter increased to $16\ \mu\mathrm{m}$ (corresponding to a higher power), the pulse focuses to highest $a_0 = 6$ at $t = 1.5$ ps. The laser intensity is better sustained along the entire interaction length compared to the smaller beams, with relatively large intensity fluctuations. However, the significant intensity enhancement does not appear to improve the mean electron energy gain curve. The temporal variation of the accelerated electron number is shown in Fig. 4.7 (d), for both electrons in the $10 - 50$ MeV and > 50 MeV ranges. Before the laser reaches the density down-ramp region (at $t = 3$ ps), the $16\ \mu\mathrm{m}$ beam drives almost twice the number of low-energy ($10 - 50$ MeV) electrons compared to a $8\ \mu\mathrm{m}$ beam. However, fewer electrons are able to gain energy above 50 MeV for the $16\ \mu\mathrm{m}$ beam. From 3 ps to 3.5 ps, a large number of electrons lose energy and become out of phase with the laser. A sheath field is formed at the density down-ramp area and channel exit due to the charge separation as the electron beam moves out from plasma to vacuum. The sheath field is stronger in the 16 $\mu\mathrm{m}$ beam case because more electrons move into the vacuum. The formation of sheath field causes the reduction in electron number, particularly for the lower energy electrons.

The focusing geometry also implies a different wavefront curvature. Previous research has demonstrated that the transverse E_y field does positive DLA work the electrons, whereas the longitudinal E_x laser field tends to decelerate electrons [45]. The ratio of laser transverse and longitudinal electric field is therefore higher for the larger focal spots ($|E_y|/|E_x|_{5\mu\mathrm{m}} : |E_y|/|E_x|_{8\mu\mathrm{m}} = 19 : 26$ at 2.2 ps). Therefore, compared to the smallest focal spot, the longitudinal electric field of larger focal spots will be less detrimental on the overall acceleration.

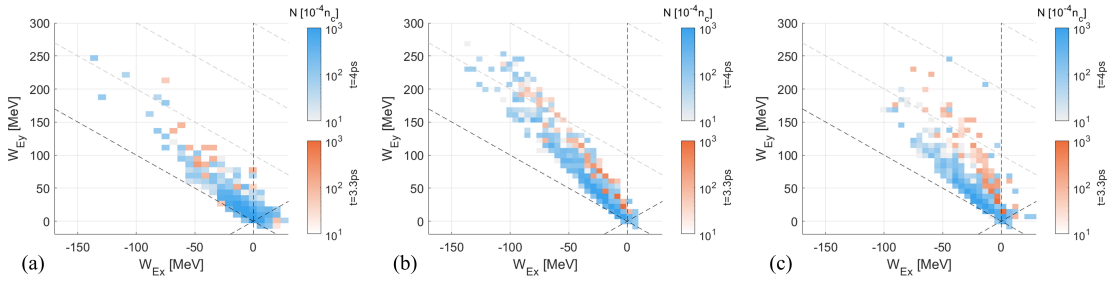

Figure 4.9: Electron distribution in the $[W_{E_x} - W_{E_y}]$ energy space before (orange markers) and after (blue markers) the sheath field down ramp region for laser focal spot size of 5 μm (a), 8 μm (b) and 16 μm (c). The number of electrons is in the logarithm scale. The diagonal dotted lines are electrons with constant total energies $(W_{E_x} + W_{E_y})$, which are equal to the y-intercept.

To investigate the effect of the wavefront curvature and sheath field for each case, the energy contributions from different field components are calculated by performing particle tracking. Seven hundred macro particles were randomly selected from electrons that move along with the laser and eventually out of the plasma. They were tracked from the start of the simulations to the time when the laser completely exits the plasma. The positions, momentum, and the exerted electric fields of the tagged electrons were output at a time interval of 25 fs. The work done by longitudinal electric field E_x and transverse electric field E_y are calculated by time integrals of $W_{E_x} = -\int_0^t |e| \cdot E_x \cdot v_x \, dt'$ and $W_{E_y} = -\int_0^t |e| \cdot E_y \cdot v_y \, dt'$, where v_x and v_y are electron longitudinal and transverse velocities respectively [35].

Fig. 4.9 shows the distribution of the tracked electrons in the $[W_{E_x} - W_{E_y}]$ energy space before ($t = 3.3$ ps, in orange) and after ($t = 4$ ps, in blue) the sheath field region for the three focusing geometries. The electrons generated by a 5 μm focal spot, are more tilted towards W_{E_x} axis in Fig. 4.9 (a), indicating significant negative work was done by the longitudinal laser electric field. Also, the blue markers almost overlap with the orange ones, implying that the electron distribution is minimally affected by the

sheath field. For the moderate and large beams, the majority of pre-sheath field (orange) electrons are around a direction of $W_{E_y} : W_{E_x} \sim 3 : 1$ at $t = 3.3$ ps, corresponding to the time of the high-energy electron number reaches peaks in Fig. 4.7 (d). However, the difference is that fewer orange electrons exceed 50 MeV in Fig. 4.9(c), as previously discussed. Secondly, a larger number of electrons are driven out of plasma by a large focal spot (higher power pulse), hence a stronger sheath field grows in the down-ramp of the plasma, resulting in a greater impact on electron distribution. The blue markers shift leftward along the negative W_{E_x} direction and there is a wider gap between orange and blue electrons for the largest focal spot, suggesting more energy loss in the sheath field and a lower final energy compared to the mid-sized beam.

The particle tracking also reveals more details of the individual electron temporal and spatial dynamics. Fig. 4.8 depicts the trajectories of eight typical energetic electrons overlaid on the instantaneous channel azimuthal magnetic fields B_z (4.8(a)-(c)) at the time of electrons arriving at $x = 1222$ μm for different laser focusing conditions. Fig. 4.8(b) clearly shows that electrons gain much higher energy with a moderate-sized driving pulse. Since the laser fields are not shown in Fig. 4.8(a)-(c), to better illustrate the relative position of electron oscillation and the area that the laser field extends transversely, the magnitude of the electron transverse displacement (y_{max}) and laser beam radius (r) at $x = 1222$ μm are presented using gray and red histograms in Fig. 4.8(d). The peak channel B_z field strength is also plotted in Fig. 4.8(d). As the channel expands with increased laser focal spot size, more electrons may be accommodated within the laser field and accelerated. As a consequence, stronger currents flow in the channel, forming a stronger B_z field. This self-generated quasi-static magnetic field assists the acceleration process by confining the electron radial excursion and deflecting the electrons in the forward direction [82]. Therefore, electrons are confined more tightly

within the wider channel because of the stronger magnetic field, as shown by the gray histogram gradually becoming shorter than the red in Fig. 4.8(d). The ratio of $y_{max}/\ r$ is 2.17 : 1.04 : 0.8 for laser focal FWHM of $5\ \mu$m, $8\ \mu$m and $16\ \mu$m. Therefore, for a $5\ \mu$m beam, the magnetic field is too weak to confine the electron in a way to efficiently allow DLA; for an $8\ \mu$m beam, the electron transverse displacement is well-matched to the laser beam width; while for a $16\ \mu$m beam, electrons are over-confined to a column narrower than the laser size.

Matching condition

Given that the maximum electron oscillation matches the laser beam size in the optimal scenario, a theoretical model can be developed to predict the optimal focusing geometry to a broader range of laboratory conditions. In the laser channel, quasi-static electric and magnetic fields are generated and the laser beam size is approximately equal to the channel width. Assuming that the ponderomotive force is balanced by the force of the charge separation in a stable ion channel, the channel width (w) can be estimated as approximately twice the laser spot radius (r) [166, 34], so that $w \approx 2r = 2\cdot 2\sqrt{a_0'}\cdot c/\omega_p$, where a_0' is the normalized laser vector potential when the laser is in the channel and ω_p is the plasma frequency. Since the laser power $P_L \propto a_0'^2 r^2 \sim a_0^2 r_0^2$, the laser spot size can be rewritten as

$$r = w/2 = [(2c/\omega_p)^2 \cdot a_0 r_0]^{1/3}, \tag{4.1}$$

where r_0 is the beam size at the focal plane. In ref. [46], the maximum electron transverse excursion from the channel axis is calculated using

$$y_{max} = 2c/\omega_p \sqrt{\left(\frac{a_0}{\epsilon}\cdot\frac{\omega_p}{\omega_0}\right)^{2/3} - 1}, \tag{4.2}$$

where ϵ is a parameter depending on the initial conditions. Here we take $\epsilon = 0.2$ for an ideal acceleration condition [164]. Equating Eq. (4.1) and Eq. (4.2), $r = w/2 = y_{max}$, yields a condition where the electron transverse oscillation amplitude matches the laser spot size.

The results are plotted in Fig. 4.6 using dashed curves with green, blue, and red color for laser powers of $30\ \mathrm{TW}, 50\ \mathrm{TW}$ and $160\ \mathrm{TW}$ respectively. For a certain curve, the laser power is constant. Each position on this curve gives the optimal laser focusing FWHM for different plasma densities to reach maximum electron energy according to the simple model. Take the red curve for example, it has a fixed laser power of 160 TW, and the optimal laser FWHM for a plasma density of $n_e = 0.02\ n_c$ is $8.2\ \mu\mathrm{m}$. For each laser power, the optimal laser focal spot size increases with the plasma density.

To examine the validity of the simple theoretic model, the experimental data are plotted using scattered markers in the [Laser FWHM – n_e] space. The green plus markers, blue triangle markers, and red circle markers represent laser power of $(30 \pm 1)\ \mathrm{TW}, (50 \pm 5))\ \mathrm{TW}$ and $(160 \pm 2)\ \mathrm{TW}$ respectively. The darkness of the markers represents the electron mean energy as shown in colorbars on the right side of the figure. Deeper color means higher energy. The darkest red and blue markers are located quite close to the red and blue dashed curves respectively, indicating that the optimized experimental parameter sets (laser power, laser focusing, and plasma density), which produced the electron beam with maximum mean energy, agree with the theoretical prediction of the ideal acceleration conditions. For low laser power of 30 TW, there is not enough experimental data showing a clear energy variation trend. Therefore, for laser power above 30 TW, the theoretical calculation based on the assumption of electron oscillation matching with the laser beam size provides good prediction of the optimal combination of laser and plasma parameters.

4.4 Effects of plasma density gradient

As indicated in section 4.3, the evolution of the laser field in the plasma density ramping up and ramping down areas to a great extent impact the electron dynamics and determine the final energy. To further enhance electron energy gain, the plasma density profile was tailored by tilting the nozzle orientation. The experimental observation, supported by supplementary simulations, illustrates that a plasma density profile characterized by a steep density gradient in the ramping up region and a shallow density gradient in the ramping down region improves energy exchange from the laser field to particles and minimizes the effect of the sheath field. The results are being summarised in a journal article in preparation [161].

4.4.1 Experimental setup

Fig. 4.10 shows the schematic of the setup. Laser pulses with a pulse duration of (700 ± 100) fs and an in-vacuum focal spot size of $8\ \mu\mathrm{m}$ were focused by an off-axis parabola to the edge of a 2 mm diameter supersonic helium gas jet target. We used two different types of nozzles with Mach numbers of 2 and 5. The gas puffed from a nozzle with a small Mach number diffuses quicker, creating an expanding gas column away from the nozzle mouth with long ramp areas. Each gas nozzle has two orientations: a straight nozzle, which is perpendicular to the laser axis, provides a symmetric density profile in the laser propagation direction (Fig. 4.10 (a)); and a 30° tilted nozzle creates a plasma with an asymmetric density profile along the laser propagation direction (Fig. 4.10 (b)). The laser will go through a ramp-up region with a sharp gradient and a ramp-down region with a gentle gradient.

The 2D plasma density profiles for Mach 2 and Mach 5 nozzles are shown in Fig. 4.10

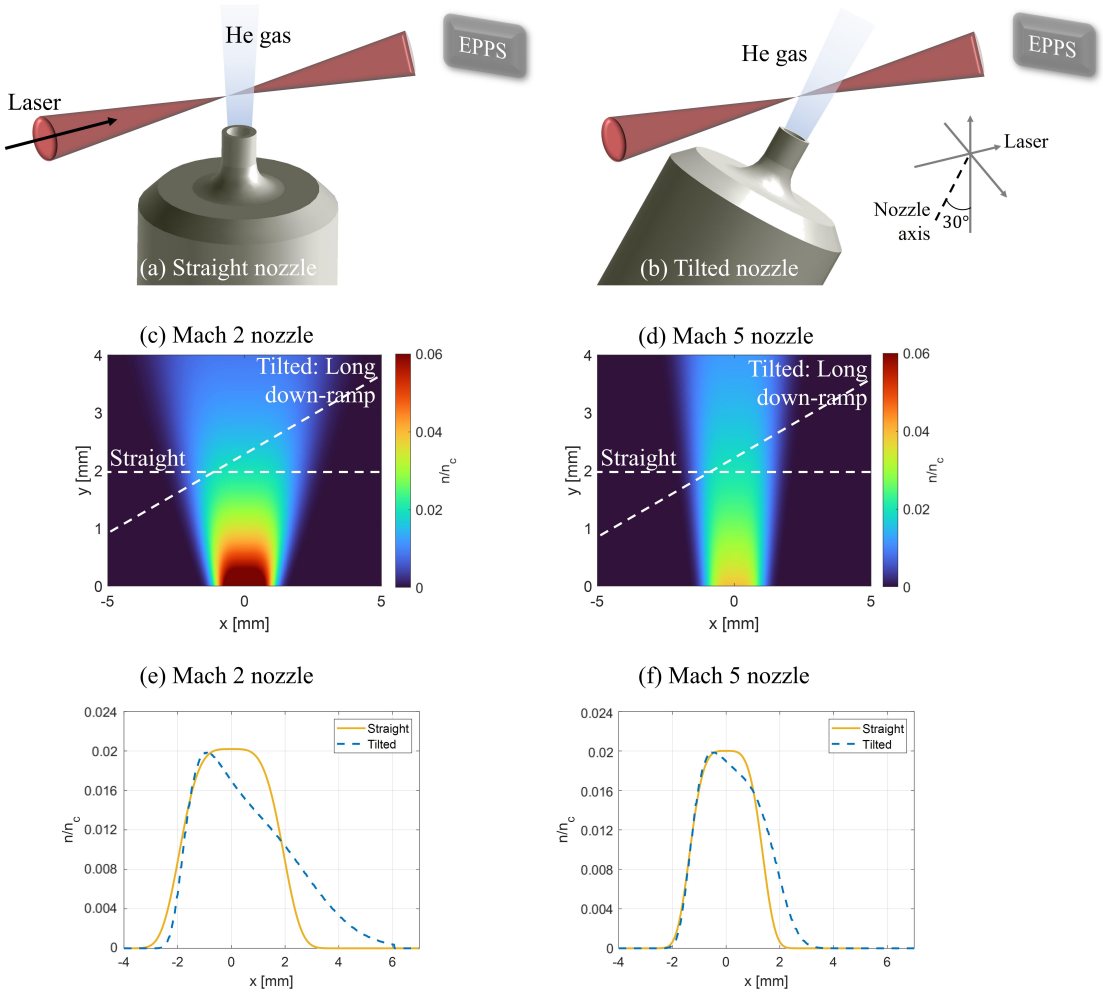

Figure 4.10: Experimental configurations using (a) a straight nozzle and (b) a 30° angled nozzle. The generated electrons are detected by an electron-positron-proton-spectrometer (EPPS). (c) and (d) are the theoretical gas density profiles for Mach 2 and Mach 5 nozzles respectively. The horizontal lines indicate the laser path in a straight nozzle configuration and the tilted lines are the laser path in a tilted nozzle configuration. The outline across the dash lines in (c) and (d) are shown in (e) and (f).

(c) and (d). The corresponding density outlines along the laser propagation direction in both straight nozzle configuration and tilted nozzle configuration are shown in Fig. 4.10 (e) and (f). The theoretical plasma density has an uncertainty of $10\% \sim 30\%$, which was measured in a Thomson scattering experiment performed by Hansen *et al.* on the OMEGA laser [9].

A laser pulse with energy of 30J, corresponding to a peak intensity of (3.9×10^{19}) Wcm^{-2} was used to interact with both Mach 2 and Mach 5 gas nozzles. The peak plasma density was $n_e = 0.02\ n_c$, where $n_c = 1 \times 10^{21}\mathrm{cm}^{-3}$ is the critical density. And a laser with a higher energy of 63 J and a peak intensity of (7.8×10^{19}) Wcm^{-2} interacts only with the Mach 5 nozzle at a lower peak plasma density of $n_e = 0.008\ n_c$.

4.4.2 Particle-in-cell simulation

To model the interaction, 2D PIC simulations were performed using the OSIRIS 4.0 code [147]. A $[750\mu\mathrm{m} \times 200\mu\mathrm{m}]$ moving window with a resolution of 24 cells per λ in both longitudinal (x) and transverse (y) direction was utilized. Each cell has 4 electrons and 4 fully ionized mobile helium ions. An open boundary condition was applied to both dimensions. The initial longitudinal density outlines are shown in Fig. 4.11. Two groups of simulations, one for the Mach 2 nozzle and another for the Mach 5 nozzle, were carried out. For each group, there are three different density profiles: (1) Up-ramp profile with a shallow gradient at the density ramping up region and a steep gradient at the density ramping down region; (2) a symmetric profile; and (3) Down-ramp profile with a steep gradient at ramping up region and a shallow gradient at ramping down region. The up-ramp and symmetric profiles are created using super-Gaussian fitting curves of the theoretical density outlines shown in Fig. 4.10(e) and (f), but on a reduced length scale. The down-ramp profile is designed to explore the effect

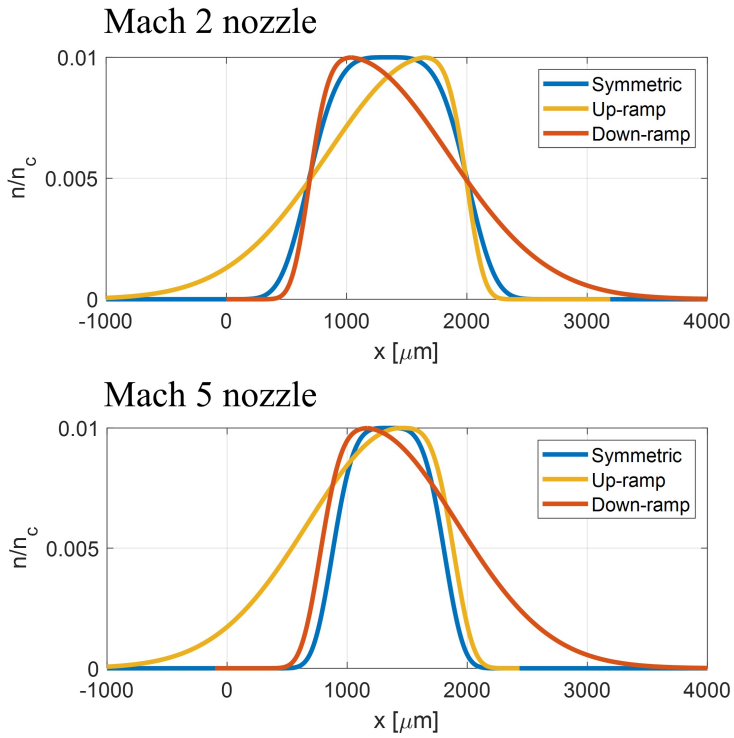

Figure 4.11: Initial longitudinal density profiles for (top) Mach 2 nozzles and (bottom) Mach 5 nozzles used in the PIC simulations.

of a nozzle tilting toward the opposite direction, which is unavailable in experiments. The plasma is uniformly distributed in the transverse direction for all the simulations. The maximum plasma density n_0 along the laser propagation axis was $0.01\ n_c$, where n_c is the critical density. A laser was linearly polarized in y direction with $a_0 = 6$, a wavelength of 1.053 nm, and a pulse duration of 700 fs. It was launched from the vacuum region and focused at $n_e = 0.95\, n_0$. The initial laser electric field has a Gaussian spatial profile and a temporal form of $E = E_0 sin(\pi t/\tau)$, where τ is the pulse duration.

4.4.3 Results and analysis

Fig. 4.12 (a) shows the electron energy spectra obtained from experiments using Mach 2 and Mach 5 nozzles in two orientations. A substantial enhancement in electron acceleration is observed with tilted nozzles. In the Mach 2 nozzle configurations (as indicated by the blue curves in the top panel of Fig. 4.12), a tilted nozzle produces twice as many accelerated electrons as a straight nozzle within the energy range of 10 MeV to 100 MeV. Moreover, the mean electron energy is improved, measuring 17.9 MeV for a straight nozzle and 20.6 MeV for a tilted nozzle. When the same laser energy of 30 J and a peak plasma density of $0.02\ n_c$ are applied to a Mach 5 nozzle configuration, the total number of accelerated electrons shows a similar trend. The number ratio of $10 - 100$ MeV electrons between a tilted nozzle and a straight nozzle is $N_t : N_s = 1.8 : 1$. However, the mean electron energies for both configurations are approximately 20.8 ± 0.2 MeV. The difference between two nozzle orientations becomes larger as the laser energy increases to 63 J and the plasma density drops to $0.008\ n_c$. As illustrated by the red curves in Fig. 4.12 (a), while the solid and dash lines show similar slopes, indicating the same effective temperature, a notable gap is evident between the two lines, with the electron number ratio being $N_t : N_s = 4.5 : 1$. Therefore, an underdense plasma with a sharp ramping up

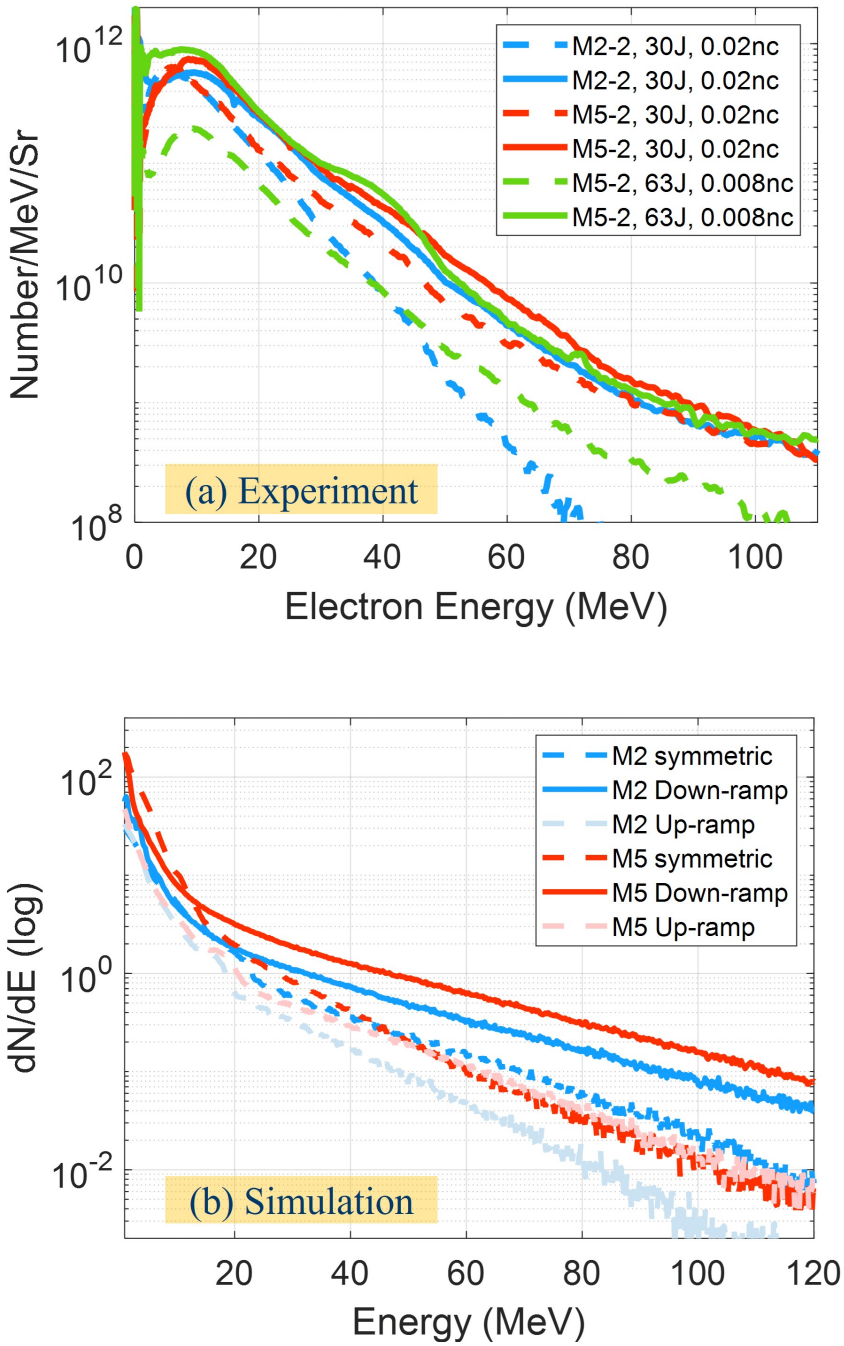

Figure 4.12: (a): Experimental electron spectra for different nozzle configurations. The dashed curves represent data acquired from straight nozzles and the solid curves represent data from tilted nozzles. (b): Electron spectra from simulations. The blue and red colors correspond to Mach 2 and 5 simulations respectively.

region and a gentle ramping down region significantly increases the accelerated electron number from the DLA process.

2D PIC simulations demonstrate the same electron variations with plasma density gradients as the experimental data. Fig. 4.12 (b) shows the simulated electron energy spectra generated by a Mach 2 nozzle and a Mach 5 nozzle. A plasma with the down-ramp initial density profile provides the optimal acceleration condition for both nozzle types. To directly compare with the experimental analysis, we consistently use electrons within the energy range of $10 - 100$ MeV in our calculations. For the Mach 2 nozzle, the electron number ratio is $N_U : N_{Sy} : N_D = 0.52 : 1 : 1.37$. The corresponding mean electron energies are 21.6 MeV, 24.3 MeV, and 30.5 MeV for up-ramp, symmetric, and down-ramp density profiles respectively. For the Mach 5 nozzle, the electron number ratio is $N_U : N_{Sy} : N_D = 0.54 : 1 : 1.77$. And the mean electron energies are 24.7 MeV, 21 MeV, and 31.2 MeV for up-ramp, symmetric, and down-ramp respectively.

The particle motion within the density ramping up region, plateau and ramping down region vary with different plasma density gradient conditions, and the variations are due to distinct factors in each segment. To comprehensively study the impact of density gradients on laser propagation and the corresponding particle behaviors, we separately investigate the interaction in these three sections. In the plasma ramping-up area, a sharp density gradient is found to be more desirable for the electron injection. Fig. 4.13 shows the trajectories of the most energetic electrons in the Mach 5 nozzle simulation sets. The gray curves in the figure represent the initial plasma density profiles, offering a reference for the electron positions. Electrons undergo rapid oscillations characterized by small amplitude and high frequency until they get in phase with the laser field and oscillate between the channel boundaries. As shown in Fig. 4.13, many hot electrons originate from a specific low-density position n_s at some distance inside the plasma, rather than

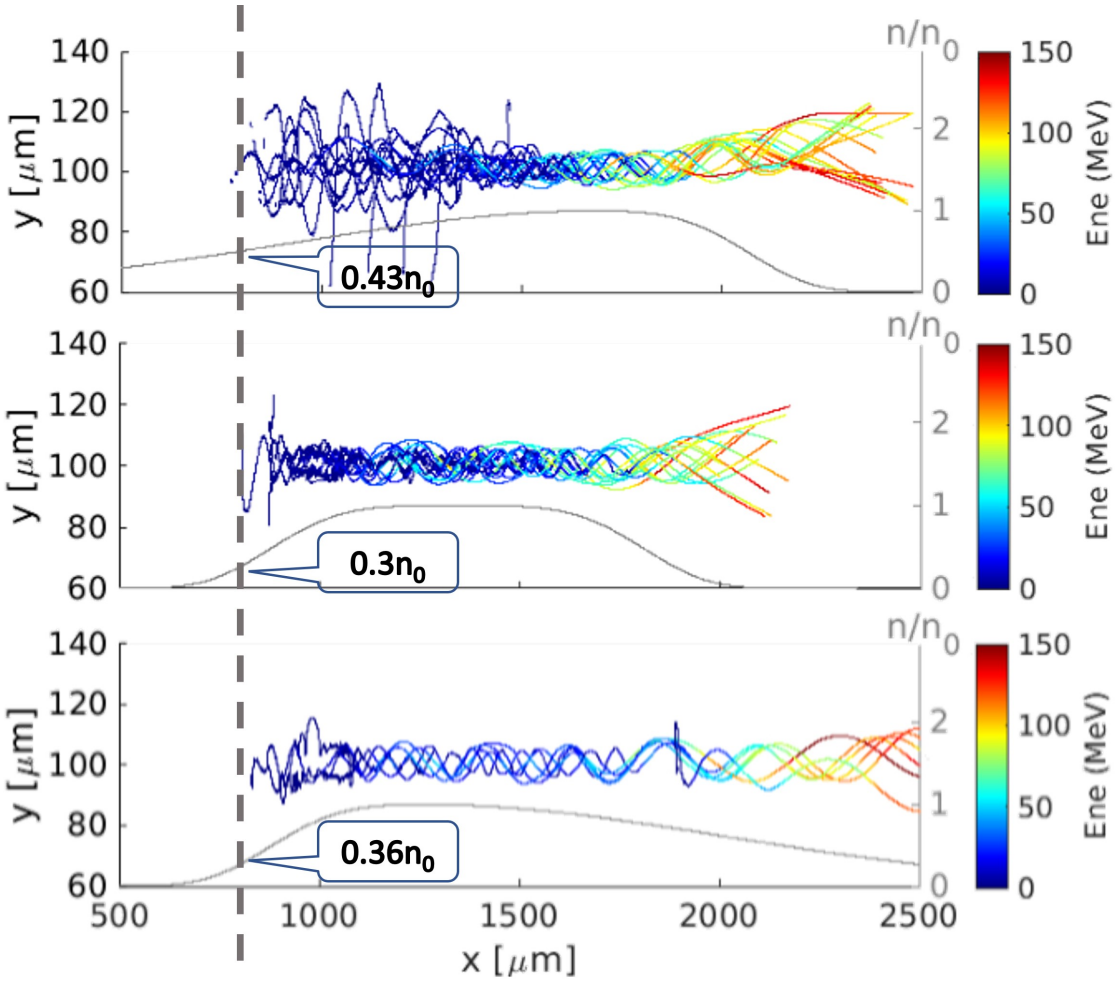

Figure 4.13: Trajectories of energetic electrons that eventually move out of plasma with the laser pulse. From top to bottom are the Up-ramp profile, symmetric profile, and Down-ramp profile respectively.

from the vacuum-plasma boundary at the outset. The lowest initial density/position of the high-energy electrons is $n_s \sim 0.43\ n_0$ in the up-ramp panel, while electrons in the other two panels originate from a lower density of approximately $n_s \sim 0.34\ n_0$. Although an up-ramp plasma profile with a shallow gradient has a longer ramping-up region than a symmetric profile, the acceleration is triggered at a higher initial density, and the effective acceleration length is slightly shortened rather than elongated in the ramping region. Additionally, the laser self-focusing effect is weaker in the up-ramp scenario, resulting in a lower laser a_0 compared to the other two cases, limiting the maximum energy that electrons can attain. Electrons initially in the area with density below n_s are less likely to accumulate high energy. Therefore, an extended ramping-up zone does not considerably contribute to the acceleration process.

It should be noted that as the nozzle gets tilted, the plasma length scale increases. To distinguish the effect of the extended plasma length, we performed a simulation using a longer symmetric profile, as shown in Fig. 4.14. The electron energy is measured when the peak of the laser pulse is located at the edge of the bulk plasma around $x = 2850\ \mu\mathrm{m}$ at simulation time $t = 8$ ps, and when the laser is in vacuum at $t = 11$ ps. Electron acceleration follows a similar pattern in bulk plasma. The distinction is that in the down-ramp plasma, the laser tends to accelerate electrons to higher energies, whereas in the long symmetric scenario, it drives a greater amount of low-energy electrons. However, from 8 ps to 11 ps, a more significant decrease in both accelerated electron number and energy occurs for the long symmetric plasma. The final electron number ratio ends up with $N_{LS} : N_D = 1 : 1.2$, where N_{LS} is the number of $10 - 100$ MeV electron generated from long symmetric plasma. As a large number of electrons are pushed out of the plasma into the vacuum over a short distance, a longitudinal sheath field with a magnitude of eight times that in down-ramp configuration is formed, which retards

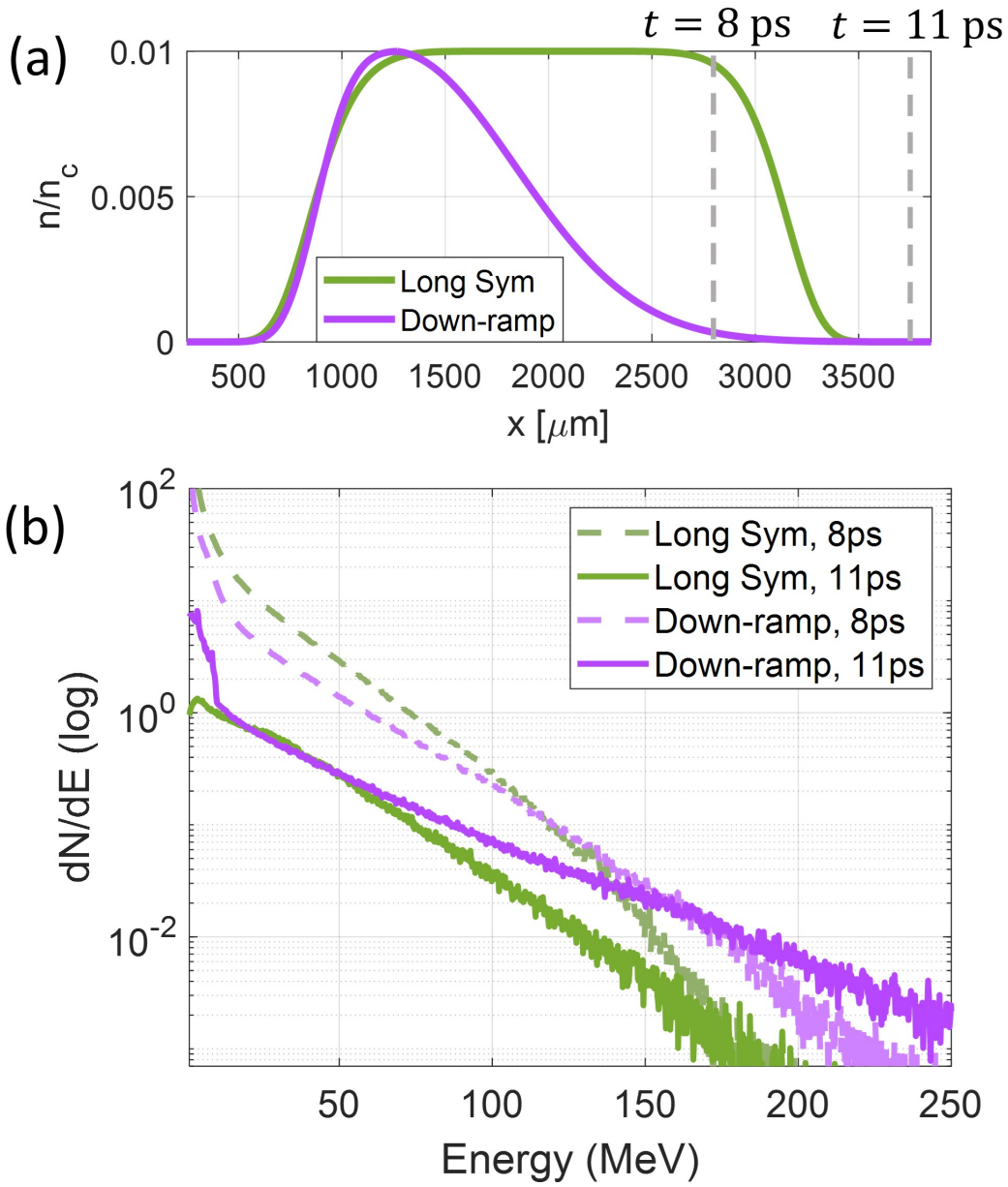

Figure 4.14: (a) Initial longitudinal density outlines for a plasma with a long symmetric density profile and a down-ramp profile. (b) Simulated electron spectra for at $t = 8$ ps and 11 ps.

electrons exiting the plasma.

In the plasma ramping down region, the laser field is enormously influenced by the density gradient, which subsequently impacts the plasma density and electron motion. Fig. 4.15 demonstrates the electron longitudinal momentum, plasma density, and the laser field envelope just before the laser completely exits the plasma. In the up-ramp density and symmetric scenarios, the laser rapidly defocuses in the plasma-vacuum connection area, leading to the expansion of the channel mouth and the creation of an estuary-like shape as shown in Fig. 4.15(d), (e). Furthermore, in the up-ramp situation, the laser beam splits into small branches with modulated leading edges (Fig. 4.15(g)). In contrast, the down-ramp plasma configuration enables the laser to maintain self-focusing along the elongated ramping down region with a tiny beam size (Fig. 4.15(I)) and high peak intensity, resulting in enhanced acceleration and a smaller opening angle at the channel mouth (Fig. 4.15(f)). Electrons continue to gain energy from the intense laser field (higher momentum in Fig. 4.15(c)), thereby effectively counteracting the sheath field.

To have further details on the energy dissipation and transmission between different fields and individual particles in the ramping-down area, we investigated the electron temporal and spatial dynamics by tracking particles that move in phase with the laser and eventually out of the plasma. Previous work has revealed the critical roles played by the laser transverse electric field (E_y), which does positive work (W_{E_x}), and the laser longitudinal electric field (E_x), which does negative work (W_{E_y}) [163, 160]. In our simulation, the sheath field, which is a longitudinal electric field formed by charge separation in the plasma-vacuum transitional area, is also proven to be crucial in electron energy exchange. The electron position, momentum, and electric fields exerted on single particles are diagnosed at every time step of 25 fs in the simulation. We calculated W_{E_x} and W_{E_y}

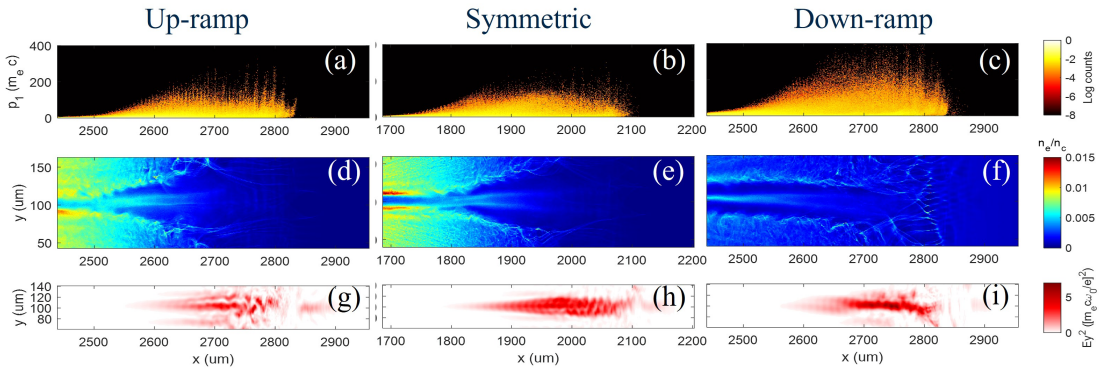

Figure 4.15: Series of PIC simulation snapshots at the time when the laser is about to leave plasma. (a) - (c) The electron number density in the phase space of $[p_1 - x]$, where p_1 is the longitudinal momentum in the unit of $m_e c$. (d) - (f) The electron density profile. (g) - (i) The laser intensity. The amplitude of the laser transverse electric field E_y is in the unit of $m_e c\omega_0/e$.

using time integrals of $W_{E_x} = -\int_0^t |e| \cdot E_x \cdot v_x \, dt'$ and $W_{E_y} = -\int_0^t |e| \cdot E_y \cdot v_y \, dt'$, where v_x and v_y are electron longitudinal velocity and transverse velocity respectively[35]. Fig. 4.16 shows the distribution of sampled particles in the [W_{E_x}-W_{E_y}] energy domain before (orange markers) and after (blue markers) the laser propagates through the sheath field. The inset figures illustrate the simultaneous energy spectra of all electrons in the simulation window. In Fig. 4.16(a) and (b), the majority of electrons show an apparent shift toward negative W_{E_x} direction from orange to blue markers due to the negative work done by the sheath field, causing the total energy decreases, which can also be seen in the insets. In Fig. 4.16(c), instead of moving left, blue-marked electrons continue to climb up in the $W_{E_x} - W_{E_y} > 0$ domain, roughly following the same slope as the orange markers. This is due to the continuous energy transfer from the laser to electrons in the tenuous plasma area, which allows more electrons to compensate for the detrimental effect of the longitudinal fields. Therefore, fewer electrons are bounced

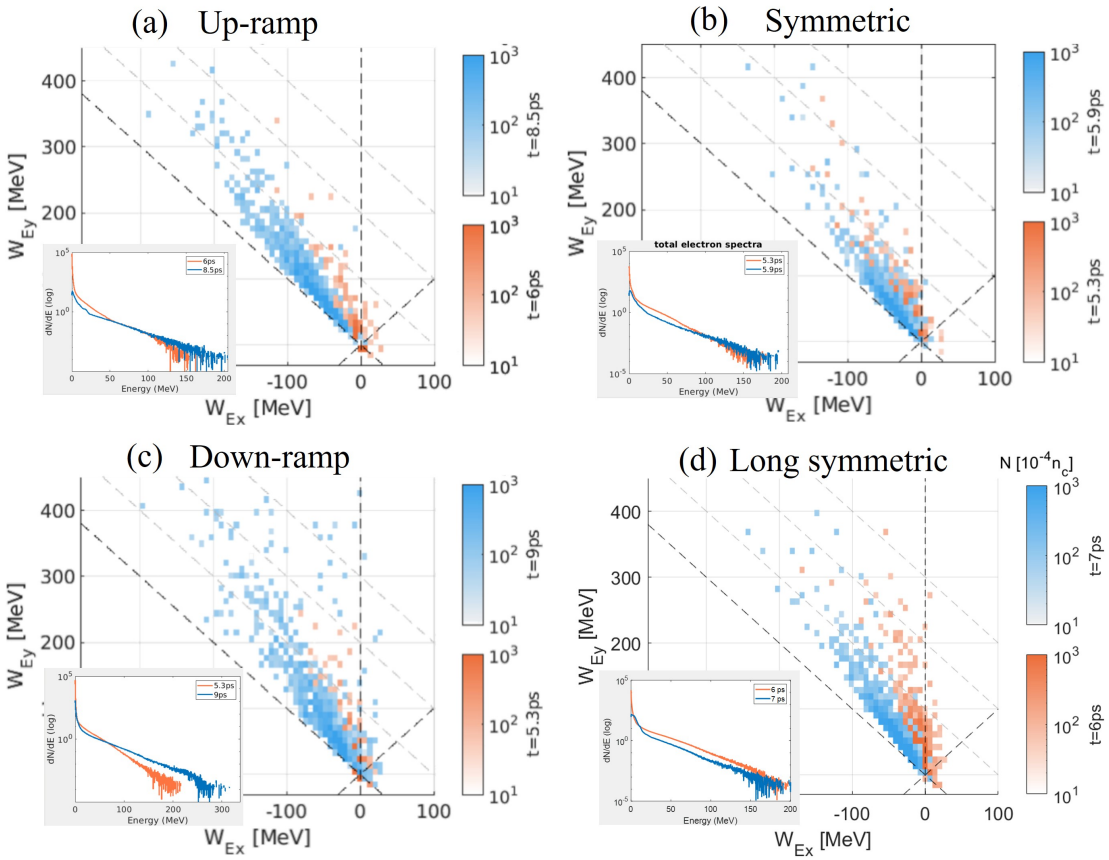

Figure 4.16: The distribution of tracked electrons in the $[W_{E_y} - W_{E_x}]$ energy space for (a) up-ramp, (b) symmetric, (c) down-ramp, and (d) long symmetric density profiles. The blue and orange colors represent the time before and after the sheath field respectively. The inset figures show the total electron spectra.

back by the sheath field to plasma and the final energy is increased. Fig. 4.16(d) shows the long symmetric case. Before the sheath field, orange-marked electrons gather close to the y axis. However, as discussed before, a larger amount of low-energy electrons move out of plasma, forming a stronger sheath field extending to a large area. Blue-marked electrons are pushed more leftward after the sheath field, implying the energy loss is greater in a long symmetric plasma. The final energy becomes lower than that of a down-ramp configuration.

4.5 Channel formation and instability

Studying the formation of the laser channel and the growth of instability in background plasma provides us with additional insights into the DLA interaction mechanism and can contribute to our comprehension of phenomena in astrophysical plasmas and fusion research. Two diagnostics – proton radiography and 4ω optical probe – were employed to observe the channel dynamics.

To produce protons for the proton deflectometry diagnostic, BL1 with an energy of 150 J, duration $\tau = 700$ fs and a focusing $\mathrm{FWHM} \sim 4\ \mu\mathrm{m}$ was used to interact with a copper foil in a proton generation package (as detailed in section 4.2.3). The proton probe beam was imaged using RCF packs.

4.5.1 Temporal evolution of the laser channel

Figure 4.17 shows an example of proton deflectometry images from single shot interactions from time of t_0 to $t_0 + 77$ps. In this shot, a laser pulse with a duration of 1 ps and energy of 111 J was apodized using a $f/5$ apodizer and then focused onto a plasma with a peak density of $0.012\ n_c$. The in-vacuum focal spot size was $7.8\ \mu\mathrm{m}$. The helium

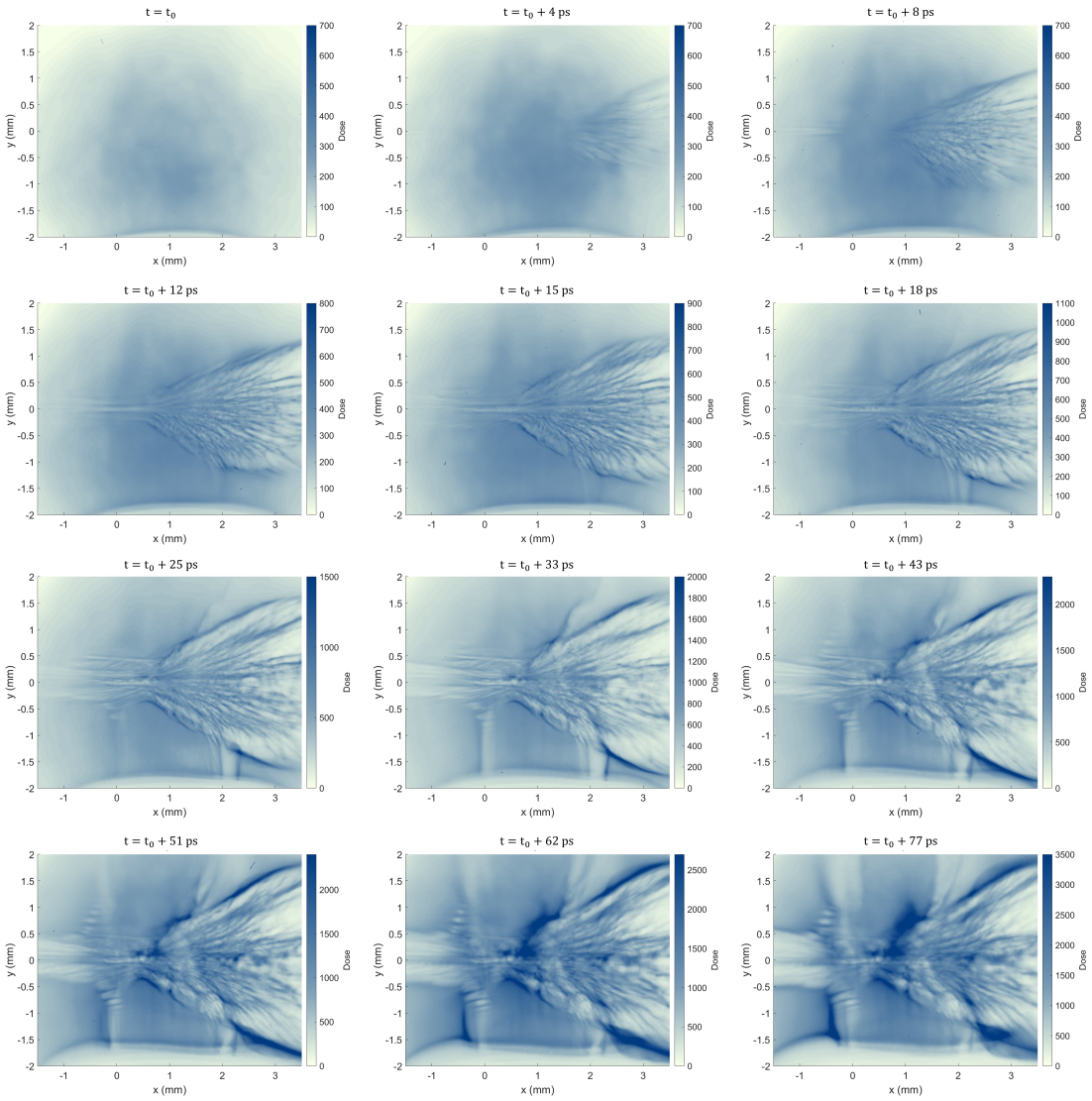

Figure 4.17: Laser channel formation process detected by proton reflectometry for shot No. 34173. The plasma density was $0.012\ n_c$. A 700 fs laser pulse with an energy of 111 J was apodized by an $f/5$ apodizer to a spot FWHM $\sim 8\ \mu$m.

gas was jetted from a Mach 5 - 2 mm diameter nozzle. The nozzle opening area is the section between $x = 0$ and $x = 2$ mm in figure 4.17. The laser propagates from left to right along $y = 0$ and was set to focus on $(x,\ y) = (0,\ 0)$. When the laser travels through plasma, electrons are expelled by the ponderomotive force, while ions, due to their heavy mass, initially remain stationary, forming an ion channel. Besides the laser channel, filamentation is another prominent feature observed in the proton images. Due to the anisotropic electron velocity distributions, instabilities like Weibel instability and current filamentation instability arise in plasma, leading to the development of small magnetic fields that deflect protons to form filamentary structures outside of the main channel. At $t = t_0 + 4$ ps, we begin to see some filaments on the right side of the frame. The filament shows up before the main channel. The protons within a particular energy bin have passed the midpoint of where the channel forms, but they are moving significantly slower than the speed of light. The laser forms the channel behind these protons and the filaments spray out the back. This fan overtakes the protons on the back side as the proton beam exits the plasma to travel to the RCF. At $t = t_0 + 8$ ps, the main laser channel is visible on the left half side of the RCF from $x = -1.5$ mm to $x = 0$. And it becomes clear at $t = t_0 + 12$ ps with a relatively uniform width of 0.1 mm at the focal plane $x = 0$. The channel extends to $x = 1$ mm before expanding and merging into filaments. The filamentation spreads in the y direction within the goblet-shaped outer boundaries, which have an opening angle of approximately $58°$. Then both the channel and the filaments keep growing in the transverse direction. Horizontal fiber filaments also started to grow and gradually surround the main channel on the left half side. At $t = t_0 + 18$ ps, some fine structures appear inside the main laser channel, which is likely due to the ion motion [72]. After the radial expulsion of electrons due to the ponderomotive force, a radial electrostatic field is formed and it accelerates ions outwards,

subsequently inducing field inversion in the channel and dark spots in the proton images. At $t = t_0 + 33$ ps, the channel and filament patterns basically stabilize and evolve much more slowly after that.

4.5.2 Current filamentation instability in background plasma

As electrons are radially expelled by the ponderomotive force, small currents form outside the channel in the background, giving rise to magnetic fields in the plasma and the growth of instability. Figure 4.18 shows a comparison of filamentation surrounding the main channel in simulation and experiments. The zoomed-in figure of the transverse B_z field in figure 4.18 (a) distinctly shows the filaments in magnetic field distribution induced by electron streaming. Through tracking the temporal evolution of the B_z field, an instability growth rate of $0.85\ \mathrm{ps}^{-1}$ is demonstrated in figure 4.18 (b). As discussed in section 2.2.5, a theoretical grow rate of the current filamentation instability can be calculated using $\Gamma_i \sim (|v_0|k_y/\gamma^{1/2})^{1/2} \sim 0.7$, where v_0 is the beam velocity in the unit of light speed, which is approximately equal to 1 in the relativistic limit, $k_y \sim 0.5$ is the transversal wave number and γ is the Lorentz factor [89], which agrees with the simulation. The total current distribution at simulation time $t = 5.5$ ps is used to compare with an experimental shadowgraphy image in figure 4.18 (c). The spatial wavelength for simulation and experiment is 20 μm and 29 μm respectively.

4.5.3 Channel exit

The goblet boundary surrounding filaments on the right side in figure 4.17 is a fairly common feature in our experiments, particularly in low-density shots. To study its formation process, a simulation of a laser pulse with $a_0 = 6$ interaction with a plasma with

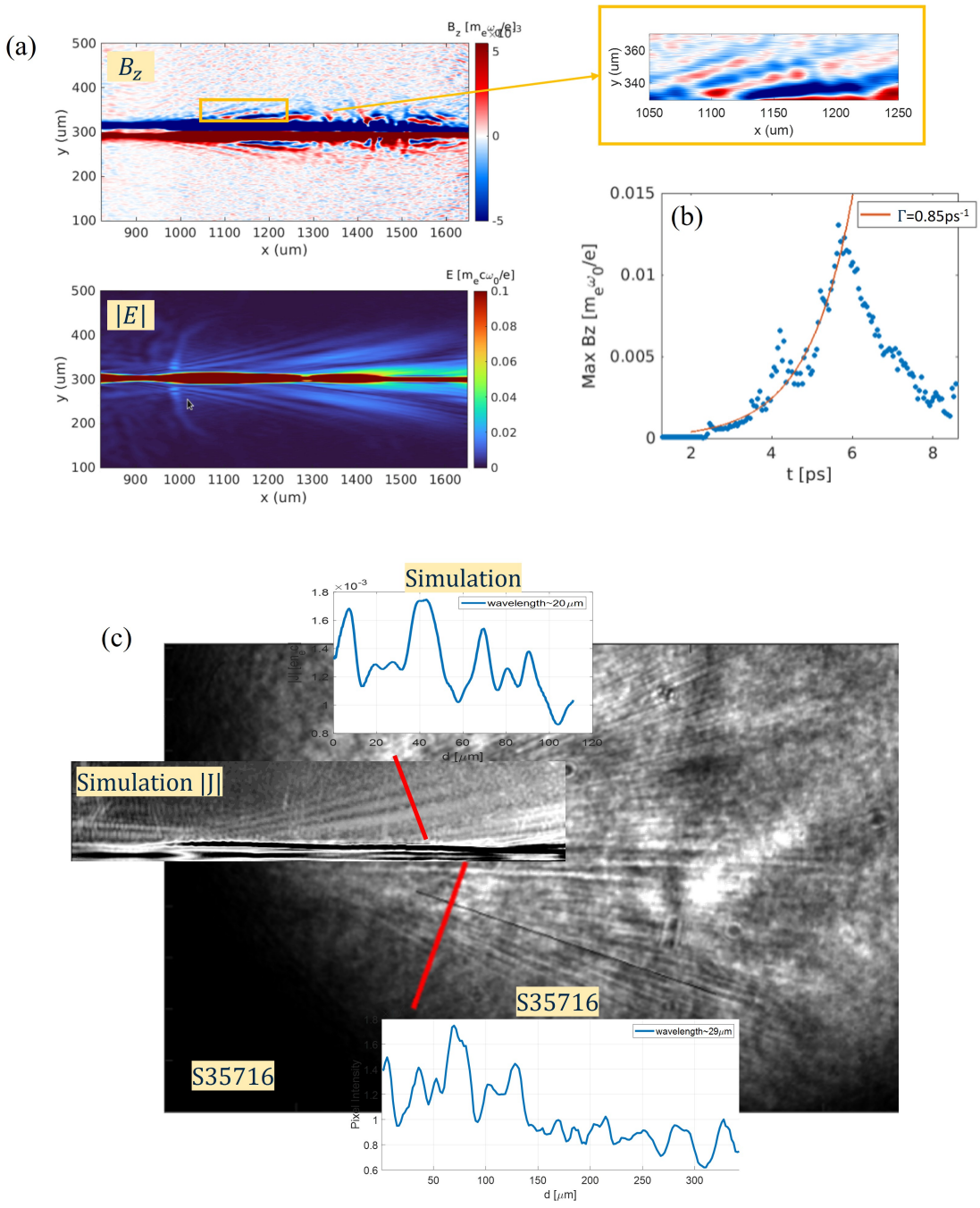

Figure 4.18: Filamentation in background plasma. (a) Simulated channel magnetic field and electric field. (b) Maximum B_z in the area of the filaments inside the orange rectangular box. $\Gamma = 0.85\ \mathrm{ps}^{-1}$ is the growth rate. (c) Comparison of simulation and experimental figure.

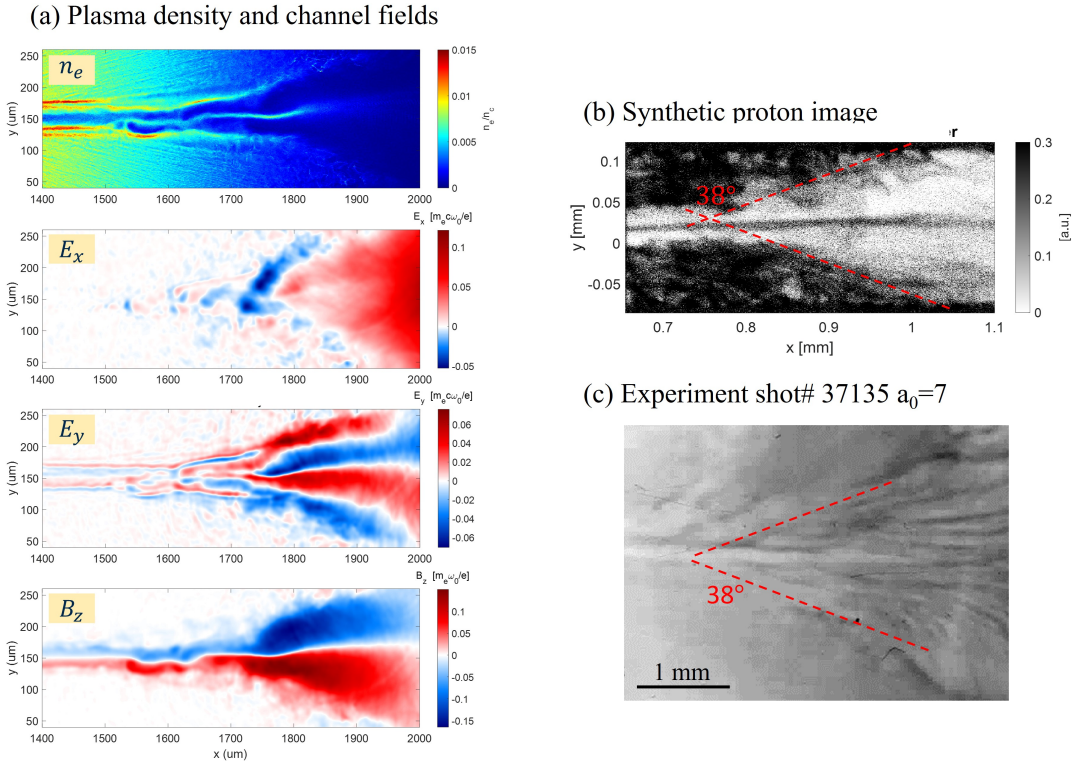

Figure 4.19: (a) A snapshot of the plasma density n_e, longitudinal channel electric field E_x, transverse channel electric field E_y, and azimuthal channel magnetic field B_z at simulation time $t = 6.35$ ps. (b) The synthetic proton image generated via 30 MeV proton propagation through the channel fields in (a). (c) A typical proton image obtained in the experiment.

a peak density of $0.01\ n_c$ was carried out.

Figure 4.19 (a) shows snapshots of the plasma density and channel fields after the laser leaves the simulation window. When the laser exits the plasma, it travels through a density ramping-down area, which serves as a transition zone connecting the bulk plasma and the vacuum. The beam spot size increases as it defocuses in the tenuous plasma, leading to the creation of an expanding channel exit with a large opening angle, resembling an estuary shape in the plasma density profile. Later on, complex channel fields quickly evolve as a result of the rapid particle movement and current flow in this

region. As shown in figure 4.19 (a), localized longitudinal sheath field E_x is generated due to charge separation caused by electrons moving out. After electrons are expelled radially, ions start to move in the radial direction following electrons at a later time. As a result, a field reversal is observed in the channel center in the E_y panel. Besides, the electron current flow forms an azimuthal magnetic field B_z along the entire channel. Using a 2D field retrieval algorithm [22], a synthetic $30\ \mathrm{MeV}$ proton deflectometry image at $8\ \mathrm{mm}$ from the interaction plane is obtained, as shown in figure 4.19 (b). The opening angle of the channel mouth is $38°$, which agrees with a measurement in one experimental proton image (figure 4.19 (c)) created using similar parameter setups with laser $a_0 = 7$ and plasma density of $0.01\ n_c$.

4.5.4 Effects of focusing on channel length

A laser pulse with a larger focal spot size usually creates a clean and nice channel. Figure 4.20 shows the in-vacuum transverse laser beam profile at their focal positions and the channel they created for different laser focal spot sizes. The channels were imaged by proton beams. We observe a nicer beam spot as the laser focal FWHM increases. A nicer channel with clearer boundaries, uniform width, and fewer filamentations outside is formed by larger laser beams. The laser channel could maintain its shape and keep a field width from the edge of the gas nozzle (marked by verticle orange lines) until a point where the channel starts to split. The length of the main channel from the nozzle edge to the splitting point increases approximately linearly with the focal spot size, as shown in the bottom panel in Figure 4.20.

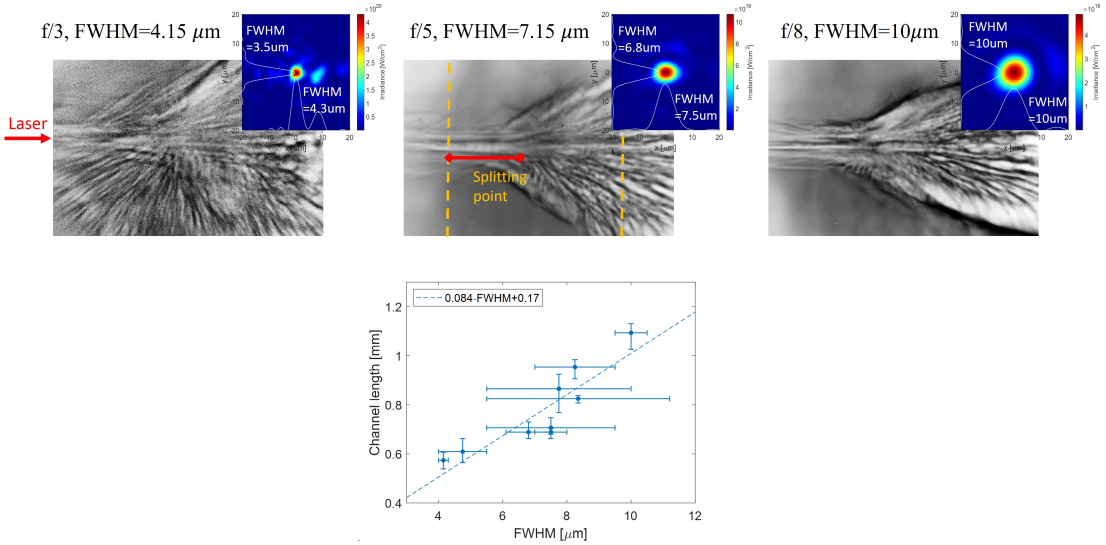

Figure 4.20: Top: Proton images showing laser channel for laser in-vacuum focal spot $\mathrm{FWHM} = 4.15\ \mu\mathrm{m},\ 7.15\ \mu\mathrm{m},\ \text{and}\ 10\ \mu\mathrm{m}$. The inset figures show the laser in-vacuum focal spots with the white curves showing horizontal/vertical outlines across the beam center. Bottom: The channel length vs laser focusing FWHM. The channel length is defined as the distance from the laser focal position (nozzle edge) to the channel splitting point, as illustrated by the red section in the top middle figure. The dashed line is a linear fitting curve with its function shown in the legend.

4.5.5 Effects of pulse duration on channel formation

One of the parameters that could have a significant influence on the channel formation is the laser pulse duration. Figure 4.21 shows the temporal evolution of different channels created by laser with pulse durations (τ) of $1\ \mathrm{ps},\ 3\ \mathrm{ps}$, and $5\ \mathrm{ps}$ respectively. A constant peak plasma density of $n_0 = 0.02\ n_c$ and a focal spot FWHM of $(7.3 \pm 1.0)\ \mu\mathrm{m}$ were utilized for all three shots.

For $\tau = 1\ \mathrm{ps}$, the channel evolution is similar to the shot using a lower plasma density of $0.012\ n_c$ in section 4.5. A central channel is clearly shown at $t = t_0 + 6\ \mathrm{ps}$ and it expands continuously from $t_0 + 6\ \mathrm{ps}$ to $t_0 + 40\ \mathrm{ps}$, accompanied by the growth of more filamentations. By $t_0 + 40\ \mathrm{ps}$, a dark dashed line is visible inside the main channel, indicating the ion movement. As the pulse duration increases to 3 or $5\ \mathrm{ps}$, outer channel boundaries develop and gradually form a wavy shape at $t = t_0 + 40\ \mathrm{ps}$.

Figure 4.22 shows how the channel width changes over time for various laser pulse durations. The channel rapidly expands within the first few tens of picoseconds after the laser propagates through the plasma until it achieves a stable state. The channel width at the stable stage is plotted using yellow markers in the right panel of figure 4.22,. Notably, the ultimate channel width increases linearly with the pulse duration. And this linear relationship is confirmed at a lower density ($0.012\ n_c$) as well, as illustrated by the blue line.

To figure out the reason for the generation of the outer channel boundaries, a two-dimensional particle-in-cell simulation was performed. To reduce the simulation time and computation memory, a moving window with dimensions of $[2882\ \mu\mathrm{m} \times 400\ \mu\mathrm{m}]$ and spatial resolutions of $[28 \times 16]$ cells per λ was utilized. The plasma has a maximum density of $0.01\ n_c$. A Gaussian laser pulse with a duration of $\tau = 3.5\ \mathrm{ps}$, $a_0 = 3.5$, a focal spot size of $\mathrm{FWHM} = 8\ \mu\mathrm{m}$ is polarized in the transverse y direction. The simu-

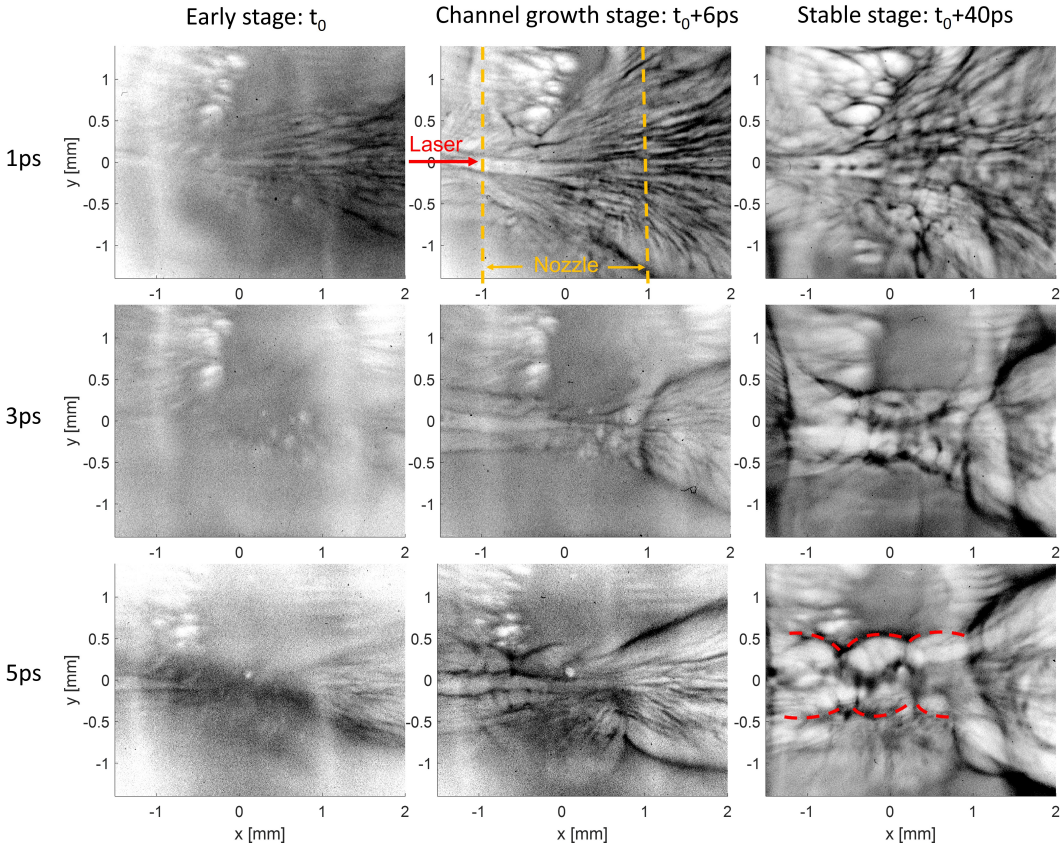

Figure 4.21: Raw proton images showing temporal evolution of laser channel in plasma. From top to bottom are generated by laser pulses with durations of 1 ps, 3 ps, and 5 ps.

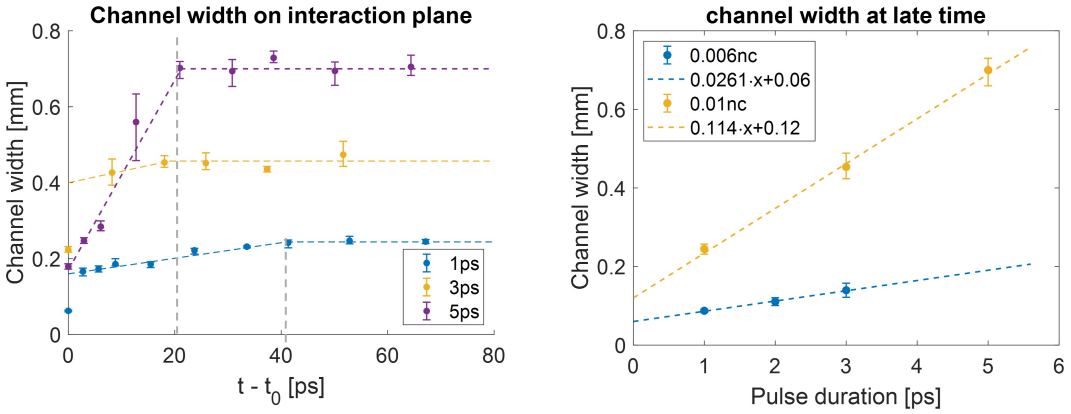

Figure 4.22: Temporal variation of channel width for different laser pulse durations. Right: channel width vs pulse duration

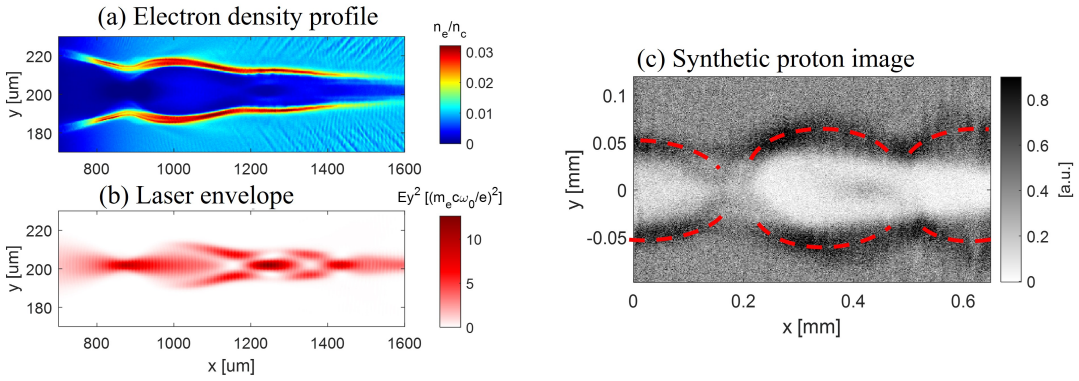

Figure 4.23: Osiris simulation results of a 3.5 ps pulse. (a) The plasma density profile. (b) The laser electric field. (c) The corresponding synthetic proton radiography.

lated plasma electron density profile, laser electric field, and the corresponding synthetic proton radiography image are shown in figure 4.23. When the beam propagates in the plasma, the leading edge ($\sim$ 1 ps) of the laser behaves exactly like a one-picosecond pulse, which creates the channel and gets self-focused inside. The middle and lagging portions of the beam go through field modulation as shown in figure 4.23 (b). The beam expands after passing the preset focal plane at $x = 880$ μm and then refocuses at separate positions around $x = 1250$ μm and $x = 1450$ μm. Along the longitudinal axis $y = 200$ μm, the laser field forms high-intensity peaks and low-intensity valleys between two peaks. The laser field forms two lobes off-axis at the valley locations, strongly indicating the generation of a new mode. The beam size change due to the modulation induces channel width variation in the plasma, forming calabash-like boundaries (figure 4.23 (a)). Consequently, periodic wavy boundary structures are clearly demonstrated in the synthetic proton radiography image and are highlighted by red dash curves in figure 4.23 (c). The shape of the channel and the dark region inside are consistent with the proton image acquired in the experiment shown in the figure 4.21. Therefore, it is very likely that a new laser mode has developed as the long-duration pulse propagates within

the plasma channel.

CHAPTER 5

Scintillator Characterization for Proton Imaging

5.1 Introduction

As shown in chapter 4, laser-driven proton deflectometry is a widely used technique to measure the time evolution of quasi-static electro-magnetic fields in high-energy-density physics (HEDP) experiments [115]. The proton source can either be a D^3He implosion [132] or a target normal sheath acceleration (TNSA) driven proton beam [115, 107], such as the diagnostic used in the DLA experiment (detailed in section 4.2.3). The small effective source size, and short emission times mean that the spatial and temporal resolution of the imaging can be very small ($\sim$ 10 μm for TNSA sources). Protons emitted from the source, propagate to the main interaction of interest, where the local electromagnetic fields deflect the protons, altering the trajectories such that an image forms in the far-field detected proton profile. Therefore, the image is magnified.

The detectors typically used for imaging the proton beam are Columbia resin 39 (CR39), or radiochromic film (RCF). These detectors are reliable: CR39 has absolute number calibration, RCF has good energy discrimination (due to the Bragg peak), and

they both have excellent spatial resolution for imaging applications. However, CR39 and RCF are single use, require replacement between shots, need scanning to process and analyze data, and in the case of CR39, require a time-consuming etching process. As proton deflectometry experiments move from being exclusively conducted at the high-energy glass-based laser systems, typically having less than 10 shots per day, to new higher-repetition extremely high-power Ti:Sapphire systems, CR39 and RCF are becoming less practical, leading to the implementation of scintillator based detectors [52, 53, 54, 55]. The luminescent yield (photons per incident proton) of the scintillator can be calibrated based on its thickness, and manufactured structures such as pixelation [121]. In addition to being multi-use, the scintillator is also expected to have a high spatial resolution, especially for experiments that need to resolve fine structures ($< 100\ \mu\mathrm{m}$) over a relatively large area. For example, the measurement of the filamentation structures in the Weibel instability shows a structure with size of $40\ \mu\mathrm{m}$ in a $6\mathrm{mm} \times 6\mathrm{mm}$ region [167]; the diagnostic of surface wave in direct laser acceleration experiments requires to resolve a periodicity of $50\ \mu\mathrm{m}$ [111].

Previous work has studied the intrinsic spatial resolution of monolithic organic scintillators using a monoenergetic proton source accelerated from a cyclotron proton source [55]. These results were promising for the use of thin scintillator detectors for the application of proton imaging. However, a laser-driven proton source has considerably different properties and operation conditions. The proton energy spectrum is typically broad and Maxwellian-like. When the proton reaches its Bragg peak in the detector material, which is the region of maximum energy loss in the proton stopping curve, the proton loses a large amount of kinetic energy in a very short distance just before it stops, producing a large local radiation dose in the detector. Unless the detecting layer is very thin (as is the case for RCF), the proton energy range that will have Bragg peaks

within the detecting layer can become significant. For proton deflectometry applications, measurement of protons with a range of energies will lead to a reduction of the image quality: Spatial smearing due to proton deflections being related to their velocities as given by the Lorentz force, and by temporal smearing due to the protons having a range of transit times from the source to the interaction of interest. Furthermore, the laser-plasma interaction driving the proton source generates relativistic electrons and high-energy x-rays that are a potential source of background signal in the scintillators. Therefore, it is important to characterize the properties of the scintillators under these more complex conditions. One approach to distinguish and account for the contributions of the background electron signal is to use a mesh grid [53, 54]. While this approach works for large scale structures such as the overall beam shape and dimensions, fine structures and imaging properties are lost.

Here we characterize a variety of scintillator types and thicknesses using TNSA accelerated protons where a background of high energy electrons and x-rays are generated. The intrinsic point spread function (PSF) is measured using a proton beam and a resolution grid. The image resolution and contrast are also characterized and compared to RCF in a point-projection imaging setup using a micro-mesh.

5.2 Experimental setup

The experiment was performed using the T-cubed laser at the University of Michigan. The laser pulses had a central wavelength of $1.053\ \mu\mathrm{m}$ and energies of 4.6 ± 0.7 J with a 400 fs full-width-at-half-maximum (FWHM) duration. An $f/2$ off-axis parabolic mirror focused the p-polarized pulse onto a $5\ \mu\mathrm{m}$ thick copper foil target at an incident angle of 24°. The elliptical focal spot had FWHM dimensions of $3 \times 8\ \mu\mathrm{m}$, giving a peak

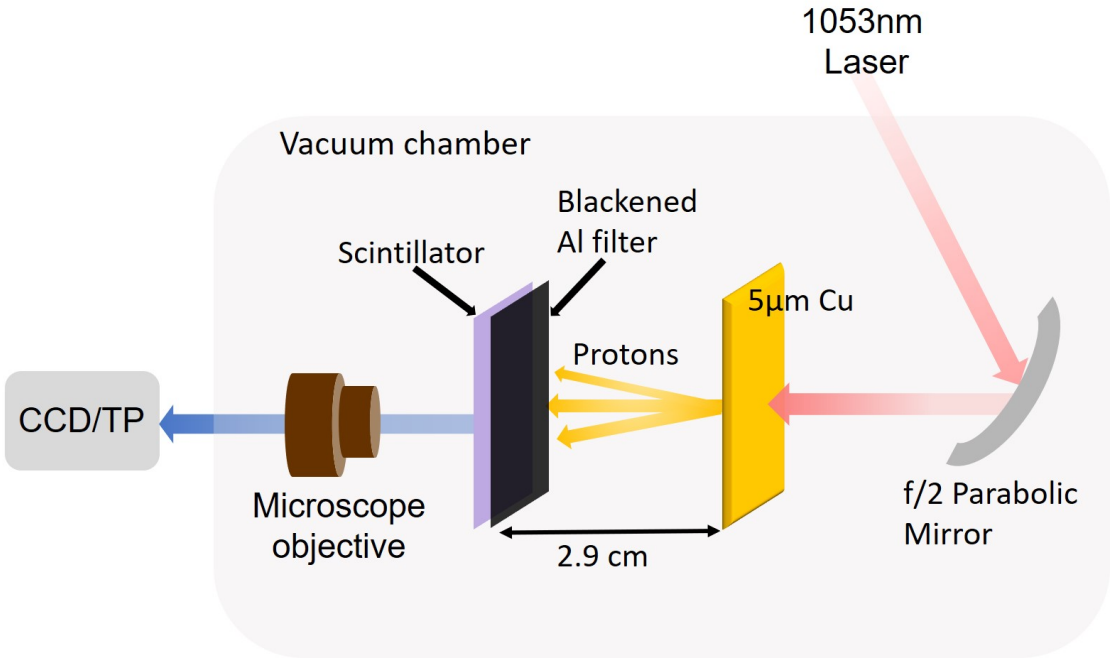

Figure 5.1: A schematic of the experimental setup. A 1053 nm high intensity laser pulse is focused by a $f/2$ parabolic mirror onto a 5 μm Cu target to generate TNSA proton beams. The proton beam is measured by either the TP spectrometer to measure the energy spectrum, or by the scintillator imaged onto a CCD with/without a microscope objective system to diagnose the spatial resolution.

intensity of $(4.3 \pm 0.9) \times 10^{19}$ Wcm^{-2}.

Fig. 5.1 shows a schematic of the experimental setup. A Thomson Parabola spectrometer (TPS) aligned along the rear target normal direction, was used to characterize the energy spectrum of the proton beam. In the TPS (details described in section 3.3.3), accelerated protons and other ions pass through a pinhole and collimator to select a small solid angle before travelling through parallel electric and magnetic fields. Particles are deflected along certain trajectories in the electric and magnetic fields due to different charge to mass ratios and energies. The ions are then detected using a microchannel plate (MCP) coupled to a phosphor screen to produce an optical signal that can be im-

Scintillator type	Nominal thickness (μm)	Actual thickness (μm)
EJ-228	50	49$\pm$3
	100	128$\pm$7
	500	359 ± 3
EJ-212	100	113$\pm$9
	500	418 ± 10
EJ-204	100	140 ± 4
	500	483 ± 4

Table 5.1: Scintillator thicknesses that were characterized in this experiment.

aged on a CCD camera. Each species forms a unique parabola on the detector screen shown in Fig. 5.2(b).

Once the proton beam had been characterized, a scintillator was placed along the proton beam path at 3 cm behind the target. Three different scintillator series from Eljen Technologies were investigated, EJ-228, EJ-212 and EJ-204 [11, 10]. These are thin, flexible, and readily available polyvinyltoluene-based scintillators that are easy to cut to a desired shape. Measurements were made using 5 cm $\times$ 5 cm squares of the scintillating material with nominal manufacture thicknesses of 100 μm and 500 μm for the EJ-204 and EJ-212 series and 50 μm, 100 μm, and 500 μm for the EJ-228 series. Table 5.1 shows the actual measured thicknesses of each scintillator type, although we will refer to the scintillators by their manufactured thicknesses.

The scintillators were shielded from any stray laser light using 50 μm thick blackened aluminum foil placed in front of the scintillators, which was also used to create a shroud around the scintillators to reduce background light. When a proton beam passes through a scintillator, the kinetic energy is lost in the material, primarily to the electrons.

Electrons are ionized or excited from the ground state to higher energy levels before a quick recombination or radiationless decay process ($\sim$ ps) accumulates them at a thermal equilibrium state. From this state electrons de-excited to the ground level within $\sim$2 ns decay time and fluorescent light of wavelength at the range of 370 - 440nm is emitted. In our experiment, this emitted light was imaged onto a Coolsnap CF CCD, for which the exposure time was much longer than the decay time.

Different imaging systems were used for the measurement of the point spread function (PSF), the relative signal contribution of electrons and X-rays, and the ability to create point-projection images. To measure the PSF, a $100\ \mu\mathrm{m}$ thick tungsten resolution grid with knife edge slits (which stopped < 6.8 MeV protons) was placed infront of the Al foil filter and scintillator. To ensure the imaging system had a resolution better than the PSF of scintillator, a Computar M1614-MP2 microscope objective collected the light emitted from the rear side of the scintillator, followed by a Computar M6Z1212-3S zoom lens mounted to the CCD which was placed outside the vacuum chamber. The averaged overall resolution of this system was $15\ \mu\mathrm{m}$ per pixel. The system resolution may fluctuate within a range of $3\ \mu\mathrm{m}$ per pixel because of the thickness variance of scintillators.

To determine the scintillator imaging capability a transmission electron microscopy (TEM) mesh was placed 1.7 mm behind the proton source producing a magnified image of the mesh on the scintillator. The lower half of the scintillator was covered with RCF layers to create a direct comparison between the two detectors. A 50 $\mu\mathrm{m}$ thick Al filter still covered the target-facing side of the detector. The imaging system of this geometry only used a CCD attached with a zoom lens and the spatial resolution was 57 $\mu\mathrm{m}$ per pixel.

5.3 Experimental results and analysis

5.3.1 Proton beam spectrum and divergence

First the proton spectrum in the target normal rear direction was characterized using the TPS. Fig. 5.2(b) shows a raw TPS image with the uppermost parabola being the dispersed proton beam and the bright spot on the top right being the "straight-through" neutral spot which acts as the reference for zero deflection. The additional parabolic signals, below the proton beam, are for different carbon ion species. The shot-to-shot proton energy spectrum variations for this experiment were primarily influenced the parameters of laser energy and the positioning of the target surface with respect to the focal position. The maximum proton energy observed by the TPS on each shot was approximately $6.7\ \mathrm{MeV}$ as shown in the spectrum in Fig. 5.2(a). A fit to the proton energy spectrum is shown as a black solid line with a form of $7 \times 10^{13} \cdot \exp(-\epsilon/T_{eff})$, with $T_{eff} = 1\ \mathrm{MeV}$ being the effective proton energy.

Fig. 5.3 shows the whole proton image on the scintillator with rectangular aluminum filters of different thicknesses covering each quarter. The thicknesses of the four Al rectangles were 12.5 μm, 42.5 μm, 82.5 μm, and 382.5 μm, correspondingly they blocked protons of energies below 900 keV, 2 MeV, 3 MeV and 7.5 MeV. The intersection of the four rectangles was aligned to the center of the proton beam. The approximate extent of the proton beam on the scintillator is illustrated by the green dashed circle, which has a radius of $0.8\ \mathrm{cm}$, corresponding to a half beam divergence of 15°.

As shown in Fig. 5.3, the top left region detecting protons above 900 keV had noticeably more signal than other three rectangles. As the filter thickness increased, a significant drop of signal is observed, as expected for a Maxwellian-like energy spectrum. In the top right region where the filter blocked all the protons, negligible low signal was

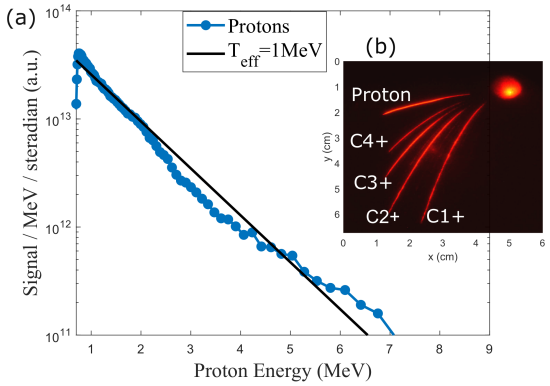

Figure 5.2: (a) Proton energy spectrum. The blue dotted line is the experiment data, the black solid line is the fitting line with a form of $7 \times 10^{13} \cdot \exp(-\epsilon/T_{eff})$, where $T_{eff} = 1$ MeV is the effective proton energy; (b) Raw image of Thomson parabola spectrometer. The top curve is the proton spectrum and the curves below are the spectra for carbon ions.

detected. Since no proton contributes to the illumination in this region, signal in this sector should only be the background due to electrons and X-rays. Other studies have found that the scintillator signal due to high energy electrons or X-rays is insignificant compared to protons when using thin (sub-mm) scintillators [168, 169, 170]. Therefore the signal generated by proton radiation dominates the emitted light, making proton imaging in this setup reliable.

5.3.2 Point Spread Function

To measure and calculate the intrinsic PSF for each scintillator we attached a 100 μm thick tungsten resolution grid in front of each scintillator and the 50μm Al filter. The grid consisted of several groups of slits with various widths. A calculation using SRIM [171, 172] shows that a 50 μm Al filter would block electrons with energy < 0.1 MeV, carbon ions with energy < 45 MeV and protons with energy < 2.2 MeV. Thus the

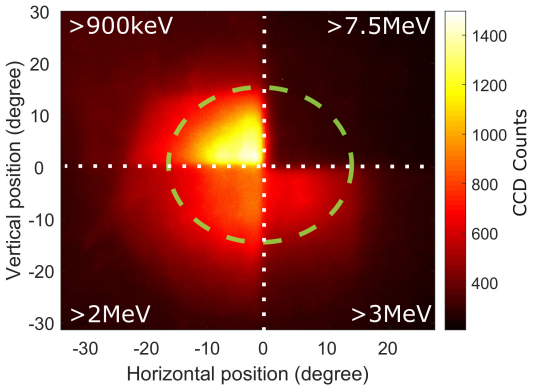

Figure 5.3: Scintillator EJ-228 image with Al filters blocking protons with energies below 900 keV, 2 MeV, 3 MeV and 7.5 MeV. The green dash circle is the $1/2$ peak intensity, corresponding to a 15° half-angle.

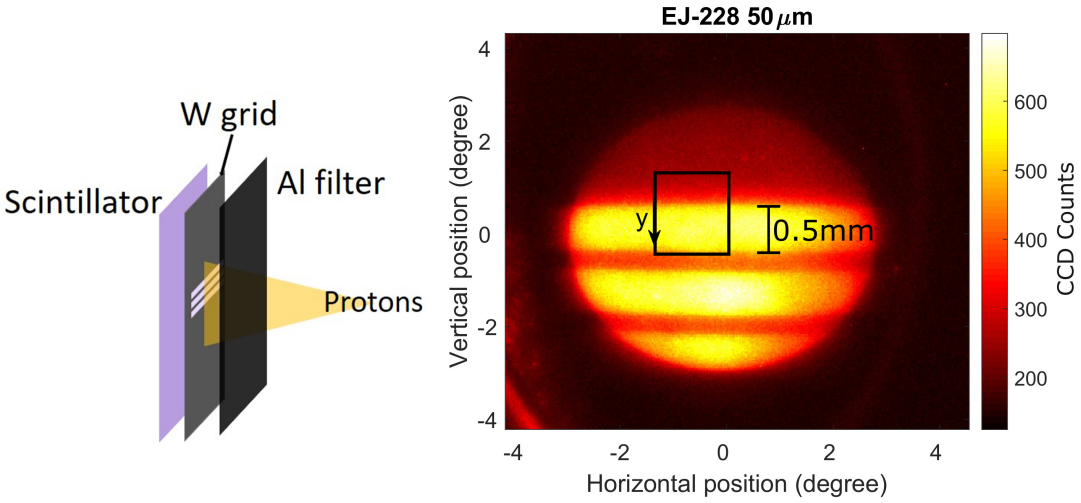

Figure 5.4: Left: A schematic of the proton beam projection through the tungsten resolution slits on a 50 μm thick EJ-228 scintillator. The width of the slits (open region) are 500 μm, the distance between the slits is 215 μm. The proton beam is centered at the lower edge of the slit group. Right: the scintillator image observed using a microscope objective, limits the field of view to 6° and produces the circular edge to the image.

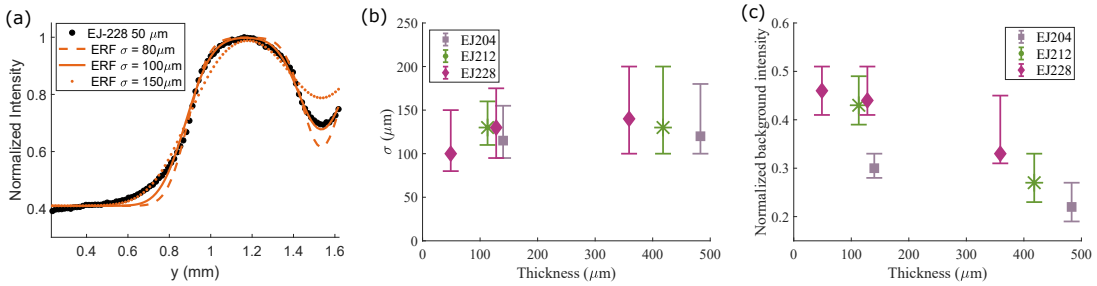

Figure 5.5: (a) Normalized intensity across the top proton bar of the $50\ \mu$m thick EJ-228 scintillator. The foot region (small y position) is the opaque tungsten area, and the intensity peak is where the proton pass through the open slit. The normalized intensity does not drop as much on the right, due to signal overlap from the second slit. The experimental data (black dots) are compared to ERF fitting curves with $\sigma = 80\ \mu$m (dotted line), $100\ \mu$m (solid), and $150\ \mu$m (dashed line). (b) Plot of the σ measurement versus scintillator thicknesses. (c) Plot of the background intensity normalized to the peak intensity of each shot versus scintillator thicknesses.

scintillator signal was only due to protons with energies in the range of 2.2 MeV to 6.7 MeV, the high-energy cutoff. The protons propagated through the slits of the grid and the black aluminium foil before hitting the front side of each scintillator. The array of $500\ \mu$m-width slits was placed in front of the scintillator, with the center of the proton beam being aligned to the lowest edge of the slits, allowing the upper half of the proton beam to transmit and the lower half to be blocked.

Fig. 5.4 shows the raw image of the $50\ \mu$m thick EJ-228 scintillator, where the circular edge is due to the objective aperture. The colorscale is proportional to the light emission from the scintillator, i.e. the lighter regions are where the protons passed through the slit and the darker slots are the tungsten-blocked areas. Images of other scintillators looked very similar to Fig.5.4 with only slightly magnification differences due to the scintillator thickness. To eliminate this error, we measured the magnification for every observation.

As protons propagate through the scintillator energy is lost primarily to exciting elec-

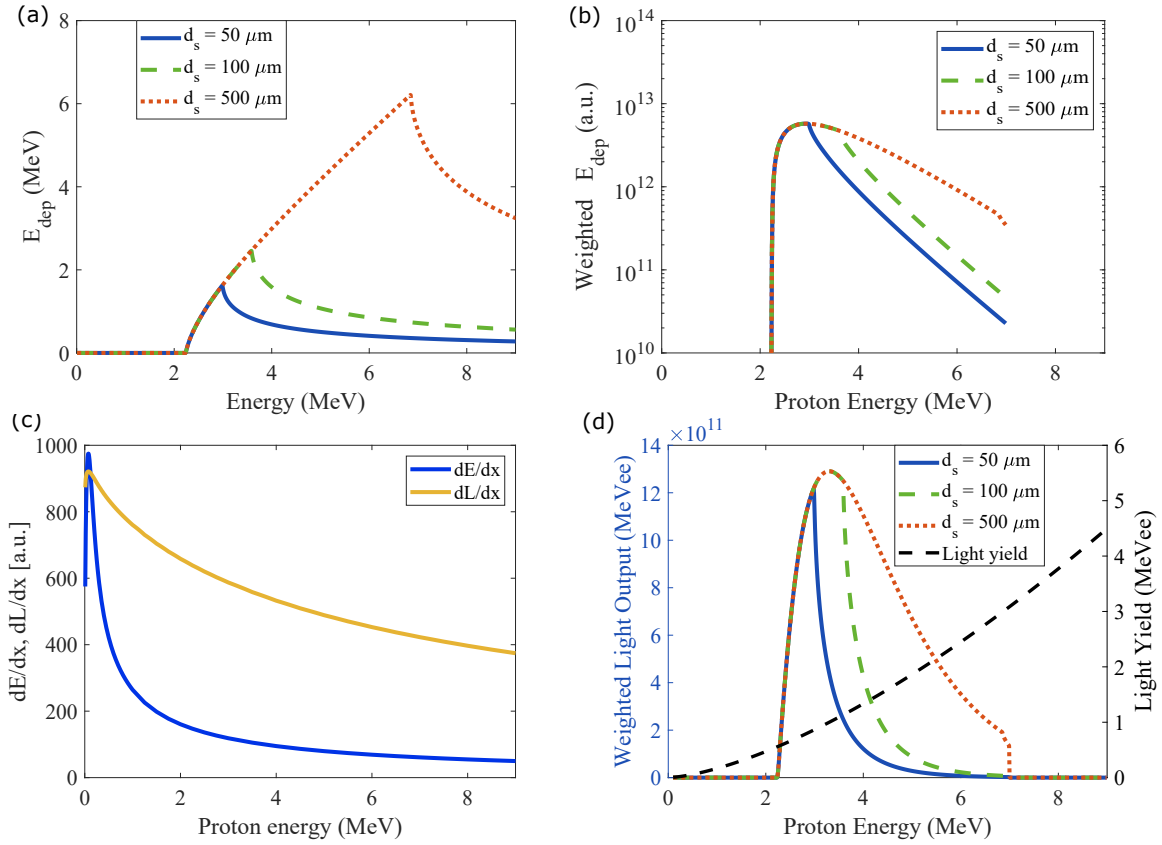

Figure 5.6: How the proton energy deposition in scintillators and light yield varies for the different nominal scintillator thicknesses. (a) The deposited energy from protons with various energies, accounting for energy loss through the $50\ \mu$m Al filter, into $50\ \mu$m (blue solid line), $100\ \mu$m (green dash line) and $500\ \mu$m (red dotted line) scintillators. (b) The energy deposition weighted by the exponential energy spectrum, $dN/dE = 7 \times 10^{13} \cdot \exp(-\epsilon/T_{eff})$, with the 7 MeV cutoff energy. (c) The proton stopping power $\frac{dE}{dx}$, and the scintillation light output per unit path length $\frac{dL}{dx}$ as a function of proton energy. The dashed curves are the exponential weighted results. (d) The light yield as a response of full-stop proton energy (black dashed curve), which is the integral of $\frac{dL}{dx}$ (yellow solid curve in (c)) and energy spectrum weighted light yield $L(E)$ in scintillators with certain thicknesses (blue, green and red curves). The units are converted to equivalent electron energy (MeVee).

trons which subsequently emit optical photons. The primary (and then secondary) electrons that are formed are emitted with similar directionality, and may go on to form further excited states and photon emission. The region of emission due to a single proton may therefore be blurred. This effect can be illustrated by the standard deviation, σ, of the PSF of the the scintillating material. Lineouts across the upper edge of the first bright slot were taken along the direction of the arrow shown in Fig. 5.4. Since a microscope objective is used, the image is distorted to a small extent around the edge. Normalized intensities shown in Fig. 5.5 were calculated as the averaged intensity of the lineouts taken from the black rectangular area close to the central vertical axis of the objective field where the intensity distribution was comparatively uniform in horizontal direction.

A compound Gauss error function (ERF) was employed to fit the experimental data and measure the point spread function given by the equation:

$$\frac{A}{2}(1+erf(\frac{x-\mu_1}{\sqrt{2}\sigma}))-\frac{A}{2}(1+erf(\frac{x-\mu_2}{\sqrt{2}\sigma}))+C \tag{5.1}$$

where A is the magnitude constant, μ_1, μ_2 are the edge positions, σ is the standard deviation corresponding to the sigmoid scale of the curve and C is a constant equal to $(1-A)$.

Fig. 5.5(a) shows the experimental data (black dots) along with ERF fitting curves (orange lines) for the $50\ \mu\mathrm{m}$ thick EJ-228 scintillator. The value of the standard deviation ranges from $80\ \mu\mathrm{m}$ to $150\ \mu\mathrm{m}$. The maximum σ ($150\ \mu\mathrm{m}$) perfectly matches the foot region, while the minimum σ ($80\ \mu\mathrm{m}$) better matches the data peak. The standard deviation for other thicknesses and scintillator types are shown in Fig. 5.5(b). σ is taken for the best fit to the experimental curves, mainly among the normalized intensity value

range of $20\% - 80\%$. For all scintillator types and thicknesses, there is not a strong dependence on thickness with σ values in the range of 100 μm–130 μm. The error bar is found by fitting to the 0%–20% normalized intensity to find the upper limit, and the 80%–100% normalized intensity to find the lower limit. For each scintillator type, the σ error bars are smaller for the thinner detector. Fig. 5.5(c) is a plot of the background signal normalized to peak intensity for each shot. Comparing the different scintillator types within similar thickness ranges, the background noise was generally largest for EJ-228, smaller for EJ-212 and smallest for EJ-204. And generally, the thicker scintillators for each type have lower background intensity, indicating a better image contrast. This is because the absolute CCD counts for the background, mainly due to high-energy electrons, is relatively flat, but the thicker scintillators generate more proton signal.

To understand the total light output from the scintillator, the weighting of the Maxwellian-like proton spectra needs to be considered. For this analysis, the proton energy spectra shift as it propagates through the 50 μm Al prior to the scintillator is accounted for, and protons with < 2.2 MeV are blocked. Fig. 5.6(a) shows the deposited proton energy for a beam with a flat energy spectrum for scintillators with different nominal thicknesses. The protons with energies at 3 MeV, 3.6 MeV and 6.8 MeV deposit the maximum energy per proton for 50 μm, 100 μm and 500 μm scintillators respectively. Higher energy protons do not reach the Bragg peak within the material and so the total deposited energy decreases with proton energy. Using a proton beam with the exponential energy spectrum shown in Fig. 5.2, the energy deposition is modified by the fitting equation and an energy cutoff of 7 MeV is applied to estimate the weighted energy deposition, shown in Fig. 5.6(b). The energy deposition is heavily weighted by the exponentially larger number of lower energy protons, meaning the light yield is dominated by the low energy protons. For thicker scintillators, the range of proton energies

that contribute significantly to the signal broadens slightly, but the energy at which the deposition peak occurs is constant.

The light output of the scintillator is a nonlinear response of the proton specific energy loss $\frac{dE}{dx}$. The light output follows Birks' law,

$$\frac{dL}{dx} = S\frac{dE}{dx}[1 + k_B(\frac{dE}{dx})]^{-1} ,$$

where $\frac{dL}{dx}$ is the light output per unit path length, S is the scintillation efficiency and k_B is a adjustable parameter for a particular material [173]. To estimate the light output, $\frac{dL}{dx}$, plotted in Fig. 5.6(c) (solid line), we take a typical value $k_B \sim 0.01\mathrm{g/MeV/cm}^2$ and use SRIM stopping power tables for the plastic-based scintillator. The exponential spectrum with $T_{eff} = 1$ MeV sharpens the stopping power and weaken the response of high energy protons. The light yield is estimated by integrating $\frac{dL}{dx}$ over the distance for protons of various energies to completely stop and is plotted as the black dashed line in Fig. 5.6(d). Intuitively, the light yield per proton increases with proton energy. Fig. 5.6(d) also plots the accumulated light output as a function of proton energy in scintillators with different thicknesses d_S, weighted to account for the Maxwellian-like energy spectra. Particles with < 4 MeV contribute most to the light yield in 50 μm and 100 μm detectors (blue and green curves). Higher energy protons have much less effect because they pass through the scintillator causing a sudden drop in light output. For the 500 μm scintillator (red dotted curve), the light output comes from a larger range of proton energies. Therefore, the 500 μm scintillator should have a higher absolute signal yield, and this is consistent with the relatively low normalized background intensity measured in Fig. 5.5(c). By taking the summation of the light yield over the whole proton energy range, the energy transfer efficiency from proton to light output is roughly

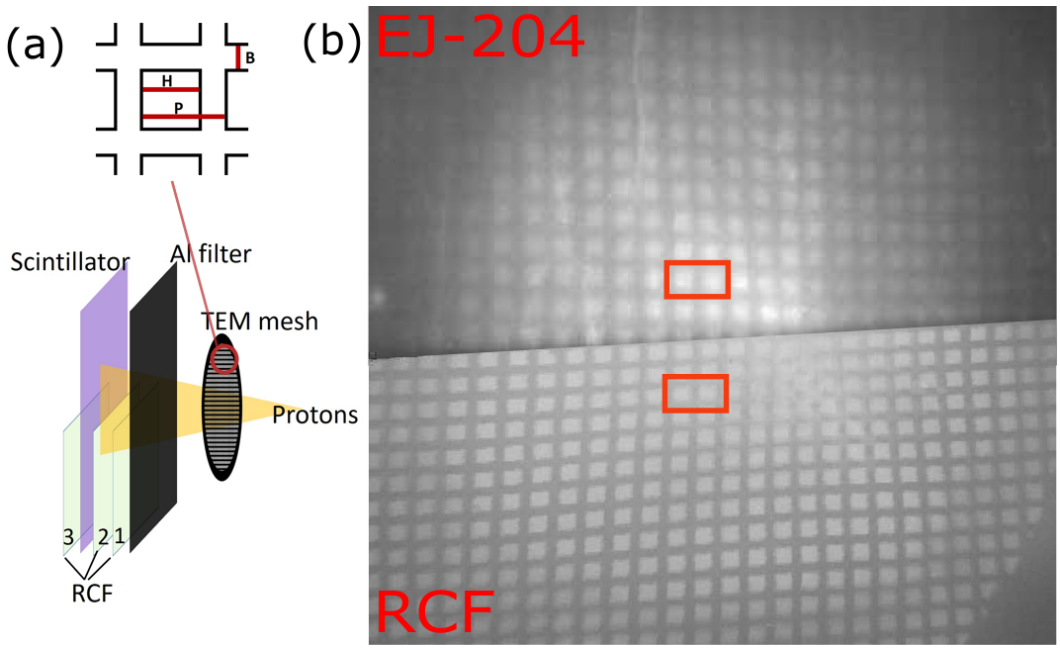

Figure 5.7: (a) The sketch of TEM mesh and pixel sizes, P = 62 μm, H = 37 μm, B = 25 μm. (b) The TEM imprint on the proton beam as observed by the EJ-204 scintillator (top) and RCF (bottom).

1.7%, 3.0% and 5.5% for 50 μm, 100 μm and 500 μm scintillators respectively. Unlike an accurate calculation [174], this rough estimate ignores the proton spatial distribution and does not integrate over the whole solid angle, and therefore likely overestimates the efficiency.

5.3.3 Effective Spatial Resolution and Contrast

The 100 μm EJ-204 scintillator was compared with RCF to investigate the imaging capabilities of each detector. The lower half of the scintillator was covered by two layers of RCF, and a third layer of RCF was placed behind to capture any protons which pass through the scintillator. The three RCF layers measured protons with energies of 2.4 ± 0.16 MeV, 4.0 ± 0.11 MeV, and 6.3 ± 0.07 MeV respectively. Note that the

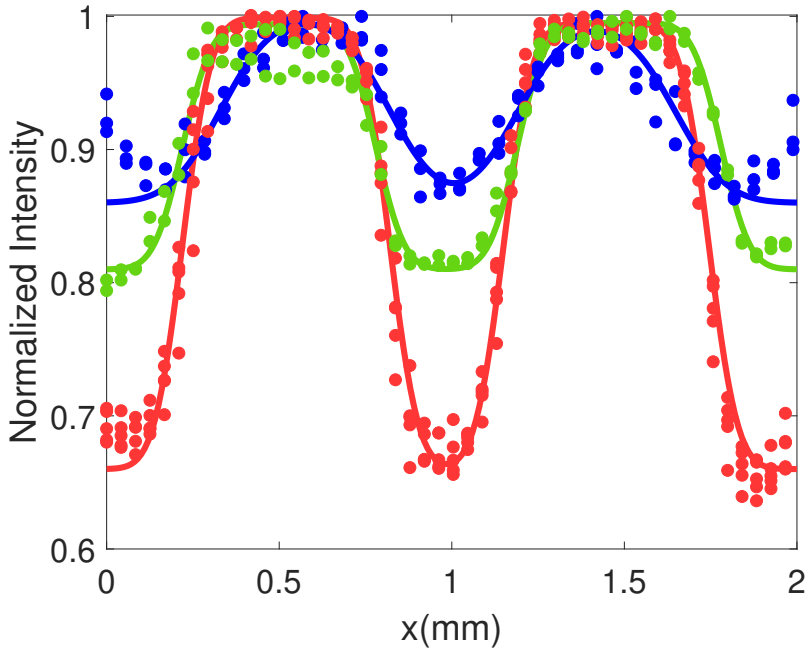

Figure 5.8: Oversampled lineouts across two pitches in the images of the first RCF layer (red), the second RCF layer (green) and the Scintillator (blue). The solid lines are the edge response curve fits.

RCF contains a very thin active layer, in the range of 8 to 12 μm, meaning a particular RCF layer is sensitive to a very narrow energy range ($\sim$ 0.2 MeV). This contrasts with the relative broad energy range the scintillators are sensitive to (see figure 5.6). In this calculation, we used the actual thickness (140 μm) for the scintillator. A TEM mesh, with a pitch of 62 μm (hole width of 37 μm and bar width of 25 μm), was placed 1.7 mm behind the proton source was projected onto the detectors. The RCF was then scanned and compared to the scintillator result as shown in Fig. 5.7. Using the dose to optical-density (OD) conversion equation obtained by Bin *et al.* [175], dose $= 374.6 \cdot OD + 2557 \cdot OD^{3.085}$, and parameters of the scanner consisting of square pixel size of 40 μm and resolution of 600 dpi, a maximum proton number per pixel $\sim 1.2 \times 10^8$ and total proton number $\sim 1.9 \times 10^{12}$ detected on the RCF were roughly calculated.

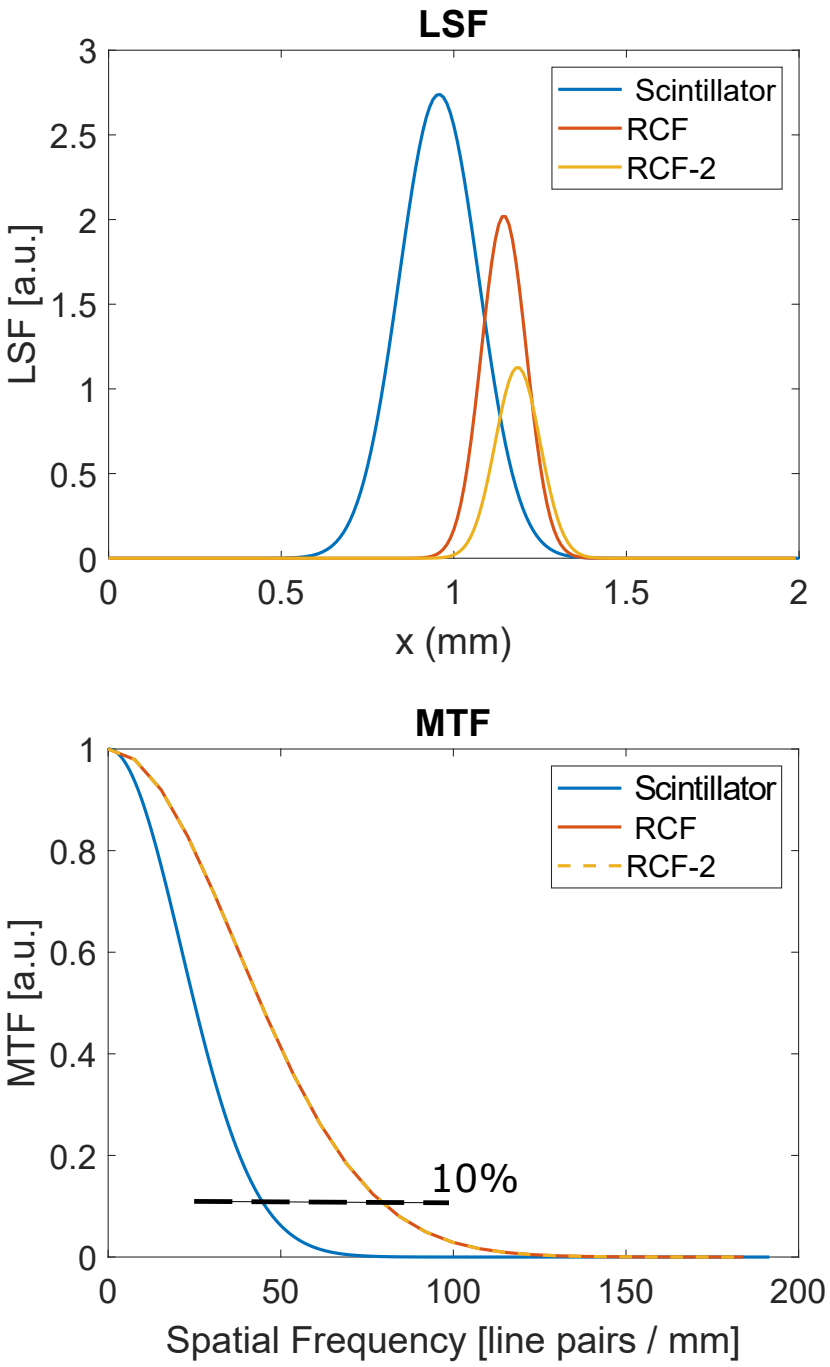

Figure 5.9: The line spread function (top) and the modulation transfer function (bottom). The resolution of the scintillator was around 26 μm, and 9 μm for the RCF.

Both detectors imaged the TEM grid with a magnification of 16. The mesh projected onto the RCF has a sharper edge and higher resolution than the scintillator. To quantify the spatial resolution of the RCF and scintillator, lineouts were taken across two pitches of the mesh from a symmetric position across the splicing line. Since the scale of the two pitches is too small to provide enough data showing the continuous intensity change near the grid edge, and the grid edges are tilted at a tiny angle, an oversampling method is used to construct oversampled lineouts. The normalized value of each pixel of the image is used as the "intensity". The pixel positions were then projected onto a line perpendicular to the grid edge which was taken as the measurement axis. We repeated this process for a group of consecutive rows to get the dotted lines shown in Fig. 5.8. ERF fitting curves with standard deviations of $65\ \mu\mathrm{m}$ and $115\ \mu\mathrm{m}$ were used as the edge response, which is also called edge spread function (ESF), for the RCF (red solid line for the first layer and green for the second layer) and scintillator (blue solid line) respectively. The edge response is the system response to a sharp straight discontinuity, which is the detector response of a knife edge illuminated by the proton beam in our experiment [176].

The fitting curves were applied for two analyses. One was to calculate the image contrast based on the Michelson contrast formula,

$$\mathrm{Contrast} = \frac{\mathrm{I_{max}} - \mathrm{I_{min}}}{\mathrm{I_{max}} + \mathrm{I_{min}}}. \tag{5.2}$$

The image contrasts are 0.22 ± 0.04, 0.13 ± 0.05 and 0.073 ± 0.02 for the first RCF layer, second RCF layer and scintillator respectively. While it might be expected for the first RCF layer to be more affected by the background signal, the large number of low energy protons (2.1–2.7 MeV) mean the contrast is best. For all the three scintillator

series, the contrast of thicker scintillator (500 μm) is larger than the thinner ones (50 μm, 100 μm) due to the longer potential propagation distance providing more opportunities for protons or the generated electrons to scatter creating a broader region of emission [55].

The second calculation was to derive the resolution limit of the scintillator following the steps in Ref [177, 178]. The derivative of the edge response is taken to obtain the line spread function (LSF), shown in Fig. 5.9. Then the modulation transfer function (MTF) is calculated by taking the Fourier transform of the LSF and normalized to its value at zero frequency in Fig. 5.9. The first zero point of the MTF represents the reciprocal of the effective resolution of the detector. However, since the first zero point on the MTF curves is difficult to identify and it corresponds to 0 contrast, here we define the resolution using the 10% MTF value, above which the MTF curves look similar for different edge responses even though it is not from an ERF fitting curves [176]. From the blue curve in Fig. 5.9(b), the intrinsic resolution of the scintillator is ~ 22 μm. Both two RCF sheets (red and yellow curves) have a same resolution of ~ 12 μm.

There are several reasons that are likely to degrade the imaging quality of scintillator, primarily due to the thickness of the "active" region. Protons will randomly scatter, changing the direction of the proton, as energy is lost to the material. Additionally, the generated electron cloud from the ionization caused by stopping the proton will form a diffuse optical emission. This differs from RCF, where the active detection layer is very thin along the propagation direction of the proton, such that the scattering and blurring effects are minimized.

CHAPTER 6

Conclusions and Future Work

This thesis has presented investigations of direct laser acceleration and measured the spatial characteristics of scintillators for proton imaging [56, 160, 161]. The study of DLA contains two main aspects, including understanding how the laser focusing and plasma density profiles influence the the generation of relativistic electron beams and the creation of a laser channel in underdense plasma. Ultra-high intensity lasers enable access to highly relativistic electrons for next-generation accelerator construction and stable ion emission for diagnostic technique advancement. Each of the experimental chapters is summarized below and potential future prospects for each topic are also discussed.

6.1 Direct Laser Acceleration

In Chapter 4, experiments using picosecond laser pulse and gas jet nozzle targets demonstrate the optimization of DLA electrons from multiple dimensions. Significant enhancement of electron energy gain from laser pulse via DLA mechanism was achieved by optimizing the laser focusing geometry using apodizers, which changed the f-number of the beam. The most energetic electron beam with maximum energy

of $400\ \mathrm{MeV}$ and mean energy of $30\ \mathrm{MeV}$ was produced using a 160 TW laser with a moderate beam size of $\mathrm{FWHM} \sim 8\ \mu\mathrm{m}$ interaction with helium plasma with density of $2 \times 10^{19}\ \mathrm{cm}^{-3}$. Experiments and simulations consistently show that focusing the laser energy on the smallest possible focal spot to achieve the highest intensity is not always advantageous for DLA. 2D PIC simulations indicate that electrons accelerated by an optimal focal spot gain more energy than a tightly focused beam in bulk plasma and lose less energy than a very large beam in the density down ramp region and through the sheath field. The optimal focusing geometry is achieved when the electron transverse oscillation amplitude matches the laser spot size in plasma, which is roughly the channel width. Based on the matching condition, a simple model is developed to find the optimal combination of laser power, focusing condition, and plasma density in experiments.

A more ideal experimental condition is approached by slanting the orientation of the gas jet nozzle at $30°$, creating a density profile, with a sharp up ramp and a shallow down ramp, along the laser propagation axis. Many more electrons, approximately 5 times the number yielded by a straight nozzle, with a higher maximum energy were detected using a tilted nozzle. Simulations are also able to explore other nozzle orientations including having the nozzle tilted toward the opposite direction, which is unavailable in experiments. Three initial plasma density distributions – up-ramp, symmetric, and down-ramp – with the same laser parameters were mimicked to examine the electron motion and laser field evolution. A steep gradient in the density up ramp region allows electrons to oscillate from a lower initial density starting point, while the electrons originate from a higher initial density in the shallow up ramp region. Hence, although the area ahead of the starting point is longer in a shallow up ramp case, it does not extend the acceleration section. In the bulk plasma region, the laser creates a wider but more uniform channel in the long down ramp case. The laser is more self-focused along the channel, preventing

laser splitting and the subsequent branching of the hot electron beam. Moreover, the effect of the sheath field is suppressed in a long down ramp plasma, resulting in more electrons leaving the plasma and with a higher final energy measured in vacuum.

The last part in Chapter 4 presents the temporal expansion of the laser-driven channel and the complex field evolution in channel and background plasma due to electron and ion motion. The channel width at the stable state is shown to be proportional to the laser pulse duration and the main channel length is related to the laser focusing condition. Simulations indicate the intriguing field development for a long pulse and imply the growth of new modes. Investigations into the channel formation and field evolution could assist fast ignition inertial confinement fusion scheme, where a strong collimating magnetic field is desired for guiding a large number of divergent ignition electrons generated in the coronal plasma [68, 179].

6.2 Scintillator characterization for proton imaging

In Chapter 5, a 4.6 J, 400 fs pulse laser focused onto a $5\ \mu\mathrm{m}$ thick Cu foil generated a proton beam with a virtual source size of $\sim 10\ \mu\mathrm{m}$, 30° divergence and maximum energy up to 6.7 MeV. The laser accelerated proton beam was utilized to measure the spatial resolution of EJ-204, EJ-212 and EJ-228 scintillators with different thicknesses. The scintillator resolution was comparable to RCF. The standard PSF for the scintillators range from $100\ \mu\mathrm{m}$ to $130\ \mu\mathrm{m}$. The thicker scintillator detectors achieved better imaging contrast. In an imaging geometry, the effective resolution limit for the scintillator was around $22\ \mu\mathrm{m}$, determining scintillators to be a feasible substitute for RCF in many situations. With a sufficient high resolution and multi-use features, the scintillators characterized are a flexible beam profile detector for laser-driven proton diagnosis

and radiography applications.

6.3 Perspectives

Secondary X-ray emission from DLA

The demonstration and optimization of high-energy DLA electron beams could pave the way for ultrahigh-fluence X-ray delivery on the picosecond time scale. As a natural consequence of electron betatron oscillation inside the channel, bright directional X-rays with high photon number has been attracting more and more attention. 3D simulations performed by O. N. Rosmej *et al.* illustrated the production of 7×10^{11} photon per shot in the energy range of 1-30 keV using a 0.7 ps, 20 J, 2×10^{19} Wcm^{-2} laser pulse and a near-critical density plasma [2]. At the critical energy of 5 keV, the brilliance of the betatron source reaches 6×10^{19} photons s^{-1} mm^{-2} mrad^{-2} $(0.1\%$ BW$)^{-1}$ (BW, bandwidth). Another mechanism for hard X-ray emission called Compton scattering, where laser photons are scattered off electrons and upshifted to higher energies, has also been studied. 2D PIC simulations performed by Y. Shou *et al* demonstrated the X-ray yield could reach 5.4×10^{10} photons J^{-1} using a carbon nanotube plasma, exceeding that in the laser wakefield acceleration (LWFA) domain by two to five orders of magnitude [180]. In addition, I-L. Yeh *et al.* have been studying the colliding of electrons with the laser in a plasma density down ramp area, indicating the possibility of producing backward X-ray with much smaller effective source size (~ 5 $\mu\mathrm{m}$) than forward x-ray [181]. The theoretical work discussed above shows promising potential in advancing X-ray radiation techniques.

Therefore, an ongoing and very valuable continuation of the DLA project would be to measure and characterize the secondary X-ray beam. Considering the features of the

betatron radiation, one of the difficulties is to find a proper detector accommodated for a broadband spectrum, high energy, and high yield X-ray. A customized Ross Filter pair, which was initially designed by P. M. King *et al.* for diagnosing x-rays from LWFA [182], could be a possible option. Based on the optimization of electron acceleration and theoretical exploration of photon generation, experimental conditions could be tailored for X-ray emission. A well-controlled x-ray source will dramatically enhance the radiographic capabilities of moderate relativistic intensity laser systems operating in high-energy-density research [183].

A second beam guiding in laser channel

To better control DLA, a two pulses co-propagation scheme might be able to enhance DLA electron generation and provide more flexibility in controlling the electron beam properties. In Chapter 4, proton deflectometry diagnostic clearly shows that a millimeter-scaled straight clean channel is established several picoseconds after the laser plasma interaction. The laser-driven channel has a low density in the center and a high density at the boundaries, facilitating an ideal structure for laser guiding. In the co-propagation design, a laser with low power, e.g. laser $a_0 \sim 1$, can be sent to the plasma to create a channel and pre-ionize plasma. Then a second laser with a higher power can be focused into the channel after a certain time interval serving as the main acceleration pulse. The background channel fields will assist electron injection into the channel and the azimuthal magnetic field will help to confine and direct the electron beam accelerated by the second laser [47]. A handful of factors, such as the relative timing between two pulses, laser energies, pulse durations, etc, are tunable in this setup, offering ample space to customize the acceleration conditions. For example, the second laser can wait until the channel expands to the optimal width before being launched.

Scintillator stack for high rep-rate experiments

In Chapter 5, experiments using broadband TNSA proton beam demonstrate competent imaging capability of each single EJ-204, EJ-212, and EJ-228 scintillators, confirming the feasibility of using scintillators as proton detectors in plasma experiments. Due to fast relaxation time and the reusable feature, scintillator-based detectors will have more applications in laser plasma interaction diagnostics, especially as the high power laser tends to be upgraded to higher repetition rates. One of the promising future works is to build a proton diagnostic package with multiple layers of scintillator, which are filtered and separated by filters such as aluminum foils. This configuration is similar to the RCF pack described in section 4.2.3, but the scintillators need to be positioned with a relative angle with respect to each other to leave a clear field of view for an imaging system looking at the back side of each layer. A scintillator stack will enable the observation of temporal variations of the electromagnetic fields in proton deflectometry application.

A prototype of the scintillator stack for the proton energy measurement has been constructed. A different scintillator type was used [184]. Researchers in Centro de Laseres Pulsados show an example of the proton detector pack designed using 10 plates of BC-400 scintillators [184]. The scintillator pack showed similar performance as RCF stack when tested using a 10 MeV proton beam. However, it is worth to note that this experiment was conducted using quasi-monoenergetic protons. The investigation of EJ-204, EJ-212 or EJ-228 scintillator stack irradiated by broadband proton beam will extend the application of proton deflectometry diagnostics into a broader range of research fields.

BIBLIOGRAPHY

[1] Sébastien Corde, K Ta Phuoc, Guillaume Lambert, R Fitour, Victor Malka, Antoine Rousse, A Beck, and E Lefebvre. Femtosecond x rays from laser-plasma accelerators. *Reviews of Modern Physics*, 85(1):1, 2013.

[2] ON Rosmej, XF Shen, A Pukhov, L Antonelli, F Barbato, M Gyrdymov, MM Günther, S Zähter, VS Popov, NG Borisenko, et al. Bright betatron radiation from direct-laser-accelerated electrons at moderate relativistic laser intensity. *Matter and Radiation at Extremes*, 6(4):048401, 2021.

[3] NSRL. Bragg curves and peaks. https://www.bnl.gov/nsrl/userguide/bragg-curves-and-peaks.php.

[4] OMEGA EP Laser System. https://www.lle.rochester.edu/omega-laser-facility-2/6271-2/.

[5] The T cubed laser. https://cuos.engin.umich.edu/researchgroups/hfs/facilities/tcubed/.

[6] Douglas S McGregor and J Kenneth Shultis. Physical sensors: Radiation sensors. 2022.

[7] Louise Willingale. *Ion acceleration from high intensity laser plasma interactions: measurements and applications*. PhD thesis, Department of Physics, Imperial College London, 2007.

[8] DH Froula, R Boni, M Bedzyk, RS Craxton, F Ehrne, S Ivancic, R Jungquist, MJ Shoup, W Theobald, D Weiner, et al. Optical diagnostic suite (schlieren, interferometry, and grid image refractometry) on omega ep using a 10-ps, 263-nm probe beam. *Review of Scientific Instruments*, 83(10):10E523, 2012.

[9] AM Hansen, D Haberberger, J Katz, D Mastrosimone, RK Follett, and DH Froula. Supersonic gas-jet characterization with interferometry and thomson scattering on the omega laser system. *Review of Scientific Instruments*, 89(10):10C103, 2018.

[10] Eljen Technology. Ej-228, ej230 - fast timing plastic scintillator - eljen technology. https://eljentechnology.com/products/plastic-scintillators/ej-228-ej-230.

[11] Eljen Technology. General purpose ej-200, ej-204, ej-208, ej-212. https://https://eljentechnology.com/products/plastic-scintillators/ej-200-ej-204-ej-208-ej-212.

[12] Donna Strickland and Gerard Mourou. Compression of amplified chirped optical pulses. *Optics Communications*, 55(6):447–449, 1985.

[13] HERCULES 300 TW laser. https://cuos.engin.umich.edu/researchgroups/hfs/facilities/hercules-petawatt-laser/.

[14] Advanced Laser for Extreme Photonics. https://lasers.colostate.edu/aleph/.

[15] Zettawatt-Equivalent Ultrashort pulse laser System at the University of Michigan. https://zeus.engin.umich.edu/.

[16] François Amiranoff, S Baton, D Bernard, B Cros, D Descamps, F Dorchies, F Jacquet, Victor Malka, JR Marques, G Matthieussent, et al. Observation of laser wakefield acceleration of electrons. *Physical Review Letters*, 81(5):995, 1998.

[17] P Sprangle, G Joyce, E Esarey, and A Ting. Laser wakefield acceleration and relativstic optical guiding. In *AIP Conference Proceedings*, volume 175, pages 231–239. American Institute of Physics, 1988.

[18] Toshiki Tajima and John M Dawson. Laser electron accelerator. *Physical Review Letters*, 43(4):267, 1979.

[19] Deborah E Citrin. Recent developments in radiotherapy. *New England journal of medicine*, 377(11):1065–1075, 2017.

[20] Victor Malka, Jérôme Faure, Yann A Gauduel, Erik Lefebvre, Antoine Rousse, and Kim Ta Phuoc. Principles and applications of compact laser–plasma accelerators. *Nature physics*, 4(6):447–453, 2008.

[21] PM Nilson, Louise Willingale, MC Kaluza, C Kamperidis, S Minardi, MS Wei, P Fernandes, M Notley, S Bandyopadhyay, M Sherlock, et al. Magnetic reconnection and plasma dynamics in two-beam laser-solid interactions. *Physical review letters*, 97(25):255001, 2006.

[22] CAJ Palmer, PT Campbell, Yong Ma, Luca Antonelli, AFA Bott, Gianluca Gregori, James Halliday, Yiftak Katzir, Peter Kordell, Karl Krushelnick, et al. Field reconstruction from proton radiography of intense laser driven magnetic reconnection. *Physics of Plasmas*, 26(8), 2019.

[23] Hideaki Takabe, TN Kato, Y Sakawa, Y Kuramitsu, T Morita, T Kadono, K Shigemori, K Otani, H Nagatomo, T Norimatsu, et al. High-mach number collisionless shock and photo-ionized non-lte plasma for laboratory astrophysics with intense lasers. *Plasma Physics and Controlled Fusion*, 50(12):124057, 2008.

[24] Hideaki Takabe and Yasuhiro Kuramitsu. Recent progress of laboratory astrophysics with intense lasers. *High Power Laser Science and Engineering*, 9:e49, 2021.

[25] JA Baumgaertel, PA Bradley, SC Hsu, JA Cobble, P Hakel, IL Tregillis, NS Krasheninnikova, TJ Murphy, MJ Schmitt, RC Shah, et al. Observation of early shell-dopant mix in omega direct-drive implosions and comparisons with radiation-hydrodynamic simulations. *Physics of Plasmas*, 21(5):052706, 2014.

[26] R Sigel. Laser-induced radiation hydrodynamics. *Plasma Physics and Controlled Fusion*, 33(13):1479–1488, nov 1991.

[27] John Lindl. Development of the indirect-drive approach to inertial confinement fusion and the target physics basis for ignition and gain. *Physics of plasmas*, 2(11):3933–4024, 1995.

[28] R. S. Craxton, K. S. Anderson, T. R. Boehly, V. N. Goncharov, D. R. Harding, J. P. Knauer, R. L. McCrory, P. W. McKenty, D. D. Meyerhofer, J. F. Myatt, A. J. Schmitt, J. D. Sethian, R. W. Short, S. Skupsky, W. Theobald, W. L. Kruer, K. Tanaka, R. Betti, T. J. B. Collins, J. A. Delettrez, S. X. Hu, J. A. Marozas, A. V. Maximov, D. T. Michel, P. B. Radha, S. P. Regan, T. C. Sangster, W. Seka, A. A. Solodov, J. M. Soures, C. Stoeckl, and J. D. Zuegel. Direct-drive inertial confinement fusion: A review. *Physics of Plasmas*, 22(11):110501, 2015.

[29] Eric Esarey, Jonathan Krall, and Phillip Sprangle. Envelope analysis of intense laser pulse self-modulation in plasmas. *Physical review letters*, 72(18):2887, 1994.

[30] C Joshi, T Tajima, JM Dawson, HA Baldis, and NA Ebrahim. Forward raman instability and electron acceleration. *Physical Review Letters*, 47(18):1285, 1981.

[31] A Modena, Z Najmudin, AE Dangor, CE Clayton, KA Marsh, C Joshi, Victor Malka, CB Darrow, C Danson, D Neely, et al. Electron acceleration from the breaking of relativistic plasma waves. *nature*, 377(6550):606–608, 1995.

[32] A Ting, CI Moore, K Krushelnick, C Manka, E Esarey, P Sprangle, R Hubbard, HR Burris, R Fischer, and M Baine. Plasma wakefield generation and electron acceleration in a self-modulated laser wakefield accelerator experiment. *Physics of Plasmas*, 4(5):1889–1899, 1997.

[33] Wei Lu, Chengkun Huang, Miaomiao Zhou, WB Mori, and T Katsouleas. Nonlinear theory for relativistic plasma wakefields in the blowout regime. *Physical review letters*, 96(16):165002, 2006.

[34] Wei Lu, M Tzoufras, C Joshi, FS Tsung, WB Mori, J Vieira, RA Fonseca, and LO Silva. Generating multi-gev electron bunches using single stage laser wakefield acceleration in a 3d nonlinear regime. *Physical Review Special Topics-Accelerators and Beams*, 10(6):061301, 2007.

[35] C Gahn, G D Tsakiris, A Pukhov, J Meyer-ter Vehn, G Pretzler, P Thirolf, D Habs, and K J Witte. Multi-mev electron beam generation by direct laser acceleration in high-density plasma channels. *Physical Review Letters*, 83(23):4772, 1999.

[36] A Pukhov, Z-M Sheng, and J Meyer-ter Vehn. Particle acceleration in relativistic laser channels. *Physics of Plasmas*, 6(7):2847–2854, 1999.

[37] GD Tsakiris, C Gahn, and VK Tripathi. Laser induced electron acceleration in the presence of static electric and magnetic fields in a plasma. *Physics of Plasmas*, 7(7):3017–3030, 2000.

[38] Alexander Pukhov. Strong field interaction of laser radiation. *Reports on progress in Physics*, 66(1):47, 2002.

[39] Stuart PD Mangles, BR Walton, M Tzoufras, Zulfikar Najmudin, RJ Clarke, Aboobaker E Dangor, RG Evans, Sven Fritzler, Abhijit Gopal, C Hernandez-Gomez, et al. Electron acceleration in cavitated channels formed by a petawatt laser in low-density plasma. *Physical review letters*, 94(24):245001, 2005.

[40] Z Najmudin, K Krushelnick, M Tatarakis, EL Clark, CN Danson, Victor Malka, D Neely, MIK Santala, and AE Dangor. The effect of high intensity laser propagation instabilities on channel formation in underdense plasmas. *Physics of Plasmas*, 10(2):438–442, 2003.

[41] S. Kneip, S. R. Nagel, C. Bellei, N. Bourgeois, A. E. Dangor, A. Gopal, R. Heathcote, S. P. D. Mangles, J. R. Marquès, A. Maksimchuk, P. M. Nilson, K. Ta Phuoc, S. Reed, M. Tzoufras, F. S. Tsung, L. Willingale, W. B. Mori, A. Rousse, K. Krushelnick, and Z. Najmudin. Observation of synchrotron radiation from electrons accelerated in a petawatt-laser-generated plasma cavity. *Phys. Rev. Lett.*, 100:105006, Mar 2008.

[42] Louise Willingale, PM Nilson, AGR Thomas, J Cobble, RS Craxton, A Maksimchuk, PA Norreys, TC Sangster, RHH Scott, C Stoeckl, et al. High-power, kilojoule class laser channeling in millimeter-scale underdense plasma. *Physical Review Letters*, 106(10):105002, 2011.

[43] JL Shaw, Nuno Lemos, Ligia Diana Amorim, Navid Vafaei-Najafabadi, KA Marsh, FS Tsung, WB Mori, and C Joshi. Role of direct laser acceleration of electrons in a laser wakefield accelerator with ionization injection. *Physical review letters*, 118(6):064801, 2017.

[44] Rong Zhang, Li-Hong Cheng, Rong-An Tang, and Ju-Kui Xue. Direct laser acceleration in an inhomogeneous cylindrical plasma channel. *Physics of Plasmas*, 23(9):093105, 2016.

[45] A V Arefiev, V N Khudik, A P L Robinson, G Shvets, L Willingale, and M Schollmeier. Beyond the ponderomotive limit: Direct laser acceleration of relativistic electrons in sub-critical plasmas. *Physics of Plasmas*, 23(5):056704, 2016.

[46] Alexey V Arefiev, Vladimir N Khudik, and Marius Schollmeier. Enhancement of laser-driven electron acceleration in an ion channel. *Physics of plasmas*, 21(3):033104, 2014.

[47] Tao Wang, Zheng Gong, and Alexey Arefiev. Electron confinement by laser-driven azimuthal magnetic fields during direct laser acceleration. *Physics of Plasmas*, 27(5):053109, 2020.

[48] Amina E Hussein, Alexey V Arefiev, Thomas Batson, Hui Chen, RS Craxton, Andrew S Davies, Dustin H Froula, Zheng Gong, Dan Haberberger, Yong Ma, et al. Towards the optimisation of direct laser acceleration. *New Journal of Physics*, 23(2):023031, 2021.

[49] JR Rygg, FH Séguin, CK Li, JA Frenje, MJ-E Manuel, RD Petrasso, R Betti, JA Delettrez, OV Gotchev, JP Knauer, et al. Proton radiography of inertial fusion implosions. *Science*, 319(5867):1223–1225, 2008.

[50] CM Huntington, F Fiuza, JS Ross, AB Zylstra, RP Drake, DH Froula, G Gregori, NL Kugland, CC Kuranz, MC Levy, et al. Observation of magnetic field generation via the weibel instability in interpenetrating plasma flows. *Nature Physics*, 11(2):173–176, 2015.

[51] Derek B Schaeffer, Archie FA Bott, Marco Borghesi, Kirk A Flippo, William Fox, Julien Fuchs, Chikang Li, Hye-Sook Park, Fredrick H Seguin, Petros Tzeferacos, et al. Proton imaging of high-energy-density laboratory plasmas. *arXiv e-prints*, pages arXiv–2212, 2022.

[52] JS Green, DC Carroll, C Brenner, Brendan Dromey, PS Foster, Satyabrata Kar, YT Li, K Markey, P McKenna, D Neely, et al. Enhanced proton flux in the mev range by defocused laser irradiation. *New Journal of Physics*, 12(8):085012, 2010.

[53] B Aurand, L Senje, K Svensson, M Hansson, A Higginson, A Gonoskov, M Marklund, A Persson, O Lundh, D Neely, et al. Manipulation of the spatial distribution of laser-accelerated proton beams by varying the laser intensity distribution. *Physics of Plasmas*, 23(2), 2016.

[54] Lovisa Senje. *Detector development, source characterization and novel applications of laser ion acceleration*. Lund University, 2017.

[55] MJ-E Manuel, J Strehlow, JS Green, D Parker, EL Alfonso, J Jaquez, L Carlson, D Neely, FN Beg, and T Ma. Intrinsic resolution limits of monolithic organic scintillators for use in rep-rated proton imaging. *Nuclear Instruments and Methods in Physics Research Section A: Accelerators, Spectrometers, Detectors and Associated Equipment*, 913:103–106, 2019.

[56] H Tang, B K Russell, A Maksimchuk, P T Campbell, M J-E Manuel, and L Willingale. Scintillator detector characterization for laser-driven proton beam imaging. *Review of Scientific Instruments*, 91(12):123304, 2020.

[57] W-M Wang, Paul Gibbon, Z-M Sheng, Y-T Li, and J Zhang. Laser opacity in underdense preplasma of solid targets due to quantum electrodynamics effects. *Physical Review E*, 96(1):013201, 2017.

[58] LB Elouga Bom, Stefan Haessler, O Gobert, M Perdrix, F Lepetit, J-F Hergott, B Carré, T Ozaki, and Pascal Salières. Attosecond emission from chromium plasma. *Optics express*, 19(4):3677–3685, 2011.

[59] F Albert, N Lemos, JL Shaw, PM King, BB Pollock, C Goyon, W Schumaker, AM Saunders, KA Marsh, A Pak, et al. Betatron x-ray radiation from laser-plasma accelerators driven by femtosecond and picosecond laser systems. *Physics of Plasmas*, 25(5):056706, 2018.

[60] Paul Gibbon. *Short pulse laser interactions with matter: an introduction*. World Scientific, 2005.

[61] P Sprangle, Cha-Mei Tang, and E Esarey. Relativistic self-focusing of short-pulse radiation beams in plasmas. *IEEE transactions on plasma science*, 15(2):145–153, 1987.

[62] SP Le Blanc, R Sauerbrey, SC Rae, and Keith Burnett. Spectral blue shifting of a femtosecond laser pulse propagating through a high-pressure gas. *JOSA B*, 10(10):1801–1809, 1993.

[63] WB Mori. The physics of the nonlinear optics of plasmas at relativistic intensities for short-pulse lasers. *IEEE Journal of Quantum Electronics*, 33(11):1942–1953, 1997.

[64] N Naseri, SG Bochkarev, and W Rozmus. Self-channelling of relativistic laser pulses in large-scale underdense plasmas. *Physics of Plasmas*, 17(3), 2010.

[65] O Willi, DH Campbell, Angelo Schiavi, Marco Borghesi, M Galimberti, LA Gizzi, W Nazarov, AJ Mackinnon, A Pukhov, and J Meyer-Ter-Vehn. Relativistic laser propagation through underdense and overdense plasmas. *Laser and Particle Beams*, 19(1):5–13, 2001.

[66] P Monot, T Auguste, Paul Gibbon, F Jakober, G Mainfray, Av Dulieu, Malka Louis-Jacquet, G Malka, and JL Miquel. Experimental demonstration of relativistic self-channeling of a multiterawatt laser pulse in an underdense plasma. *Physical Review Letters*, 74(15):2953, 1995.

[67] APL Robinson, AV Arefiev, and D Neely. Generating "superponderomotive" electrons due to a non-wake-field interaction between a laser pulse and a longitudinal electric field. *Physical review letters*, 111(6):065002, 2013.

[68] Max Tabak, James Hammer, Michael E Glinsky, William L Kruer, Scott C Wilks, John Woodworth, E Michael Campbell, Michael D Perry, and Rodney J Mason. Ignition and high gain with ultrapowerful lasers. *Physics of Plasmas*, 1(5):1626–1634, 1994.

[69] Marco Borghesi, AJ MacKinnon, L Barringer, R Gaillard, LA Gizzi, C Meyer, O Willi, A Pukhov, and J Meyer-ter Vehn. Relativistic channeling of a picosecond laser pulse in a near-critical preformed plasma. *Physical Review Letters*, 78(5):879, 1997.

[70] K Krushelnick, A Ting, CI Moore, HR Burris, E Esarey, P Sprangle, and M Baine. Plasma channel formation and guiding during high intensity short pulse laser plasma experiments. *Physical review letters*, 78(21):4047, 1997.

[71] AL Lei, A Pukhov, R Kodama, T Yabuuchi, K Adumi, K Endo, RR Freeman, H Habara, Y Kitagawa, K Kondo, et al. Relativistic laser channeling in plasmas for fast ignition. *Physical Review E*, 76(6):066403, 2007.

[72] S Kar, M Borghesi, CA Cecchetti, L Romagnani, F Ceccherini, TV Liseykina, A Macchi, R Jung, J Osterholz, O Willi, et al. Dynamics of charge-displacement channeling in intense laser–plasma interactions. *New Journal of Physics*, 9(11):402, 2007.

[73] Gianluca Sarri, KL Lancaster, R Trines, EL Clark, S Hassan, J Jiang, N Kageiwa, N Lopes, R Ramis, A Rehman, et al. Creation of persistent, straight, 2 mm long laser driven channels in underdense plasmas. *Physics of Plasmas*, 17(11):113303, 2010.

[74] PE Young and PR Bolton. Propagation of subpicosecond laser pulses through a fully ionized plasma. *Physical review letters*, 77(22):4556, 1996.

[75] M Tatarakis, FN Beg, EL Clark, AE Dangor, RD Edwards, RG Evans, TJ Goldsack, KWD Ledingham, PA Norreys, MA Sinclair, et al. Propagation instabilities of high-intensity laser-produced electron beams. *Physical review letters*, 90(17):175001, 2003.

[76] F Vidal and TW Johnston. Electromagnetic beam breakup: Multiple filaments, single beam equilibria, and radiation. *Physical review letters*, 77(7):1282, 1996.

[77] Xiaofang Wang, Mohan Krishnan, Ned Saleh, Haiwen Wang, and Donald Umstadter. Electron acceleration and the propagation of ultrashort high-intensity laser pulses in plasmas. *Physical Review Letters*, 84(23):5324, 2000.

[78] J Meyer-ter Vehn and Zh M Sheng. On electron acceleration by intense laser pulses in the presence of a stochastic field. *Physics of Plasmas*, 6(3):641–644, 1999.

[79] Alexey V Arefiev, Boris N Breizman, Marius Schollmeier, and Vladimir N Khudik. Parametric amplification of laser-driven electron acceleration in underdense plasma. *Physical review letters*, 108(14):145004, 2012.

[80] Félicie Albert and Alec GR Thomas. Applications of laser wakefield accelerator-based light sources. *Plasma Physics and Controlled Fusion*, 58(10):103001, 2016.

[81] Z-M Sheng, K Mima, Y Sentoku, MS Jovanović, T Taguchi, J Zhang, and J Meyer-ter Vehn. Stochastic heating and acceleration of electrons in colliding laser fields in plasma. *Physical review letters*, 88(5):055004, 2002.

[82] Z Gong, Felix Mackenroth, T Wang, XQ Yan, T Toncian, AV Arefiev, et al. Direct laser acceleration of electrons assisted by strong laser-driven azimuthal plasma magnetic fields. *Physical Review E*, 102(1):013206, 2020.

[83] AV Arefiev, APL Robinson, and VN Khudik. Novel aspects of direct laser acceleration of relativistic electrons. *Journal of Plasma Physics*, 81(4):475810404, 2015.

[84] Vladimir Khudik, Alexey Arefiev, Xi Zhang, and Gennady Shvets. Universal scalings for laser acceleration of electrons in ion channels. *Physics of Plasmas*, 23(10):103108, 2016.

[85] Kavin Tangtartharakul, I-lin Yeh, Hongmei Tang, Louise Willingale, and Alexey Arefiev. Mitigation of the detrimental role of the longitudinal laser electric field during direct laser acceleration of electrons. *Physics of Plasmas*, submitted.

[86] Norman W Albright. Quasilinear stabilization of the transverse instability. *The Physics of Fluids*, 13(4):1021–1030, 1970.

[87] Ronald C Davidson, David A Hammer, Irving Haber, and Carl E Wagner. Nonlinear development of electromagnetic instabilities in anisotropic plasmas. *The Physics of Fluids*, 15(2):317–333, 1972.

[88] G Kalman, C Montes, and Daniel Quémada. Anisotropic temperature plasma instabilities. *The Physics of Fluids*, 11(8):1797–1808, 1968.

[89] Francesco Califano, R Prandi, Francesco Pegoraro, and SV Bulanov. Nonlinear filamentation instability driven by an inhomogeneous current in a collisionless plasma. *Physical Review E*, 58(6):7837, 1998.

[90] JM Cole, JC Wood, NC Lopes, K Poder, RL Abel, S Alatabi, JSJ Bryant, A Jin, S Kneip, K Mecseki, et al. Laser-wakefield accelerators as hard x-ray sources for 3d medical imaging of human bone. *Scientific reports*, 5(1):13244, 2015.

[91] Jason M Cole, Daniel R Symes, Nelson C Lopes, Jonathan C Wood, Kristjan Poder, Saleh Alatabi, Stanley W Botchway, Peta S Foster, Sarah Gratton, Sara Johnson, et al. High-resolution μct of a mouse embryo using a compact laser-driven x-ray betatron source. *Proceedings of the National Academy of Sciences*, 115(25):6335–6340, 2018.

[92] S Fourmaux, Sébastien Corde, K Ta Phuoc, P Lassonde, G Lebrun, S Payeur, Frédérique Martin, Stéphane Sebban, Victor Malka, Antoine Rousse, et al. Single shot phase contrast imaging using laser-produced betatron x-ray beams. *Optics letters*, 36(13):2426–2428, 2011.

[93] Stefan Kneip, C McGuffey, Joana Luis Martins, SF Martins, C Bellei, V Chvykov, F Dollar, Ricardo Fonseca, C Huntington, G Kalintchenko, et al. Bright spatially coherent synchrotron x-rays from a table-top source. *Nature Physics*, 6(12):980–983, 2010.

[94] John David Jackson. Classical electrodynamics, 1998.

[95] E Esarey, BA Shadwick, P Catravas, and WP Leemans. Synchrotron radiation from electron beams in plasma-focusing channels. *Physical Review E*, 65(5):056505, 2002.

[96] Kim Ta Phuoc, Fréderic Burgy, Jean-Philippe Rousseau, Victor Malka, Antoine Rousse, Rahul Shah, Donald Umstadter, Alexander Pukhov, and Sergei Kiselev. Laser based synchrotron radiation. *Physics of Plasmas*, 12(2), 2005.

[97] JP Freidberg, RW Mitchell, Ro L Morse, and LI Rudsinski. Resonant absorption of laser light by plasma targets. *Physical Review Letters*, 28(13):795, 1972.

[98] Patrick Mora. Theoretical model of absorption of laser light by a plasma. *The Physics of Fluids*, 25(6):1051–1056, 1982.

[99] F Brunel. Not-so-resonant, resonant absorption. *Physical review letters*, 59(1):52, 1987.

[100] F Brunel. Anomalous absorption of high intensity subpicosecond laser pulses. *The Physics of fluids*, 31(9):2714–2719, 1988.

[101] William L Kruer and Kent Estabrook. J$\times$ b heating by very intense laser light. *The Physics of fluids*, 28(1):430–432, 1985.

[102] Hong-bo Cai, Wei Yu, Shao-ping Zhu, and Chun-yang Zheng. Short-pulse laser absorption via j$\times$ b heating in ultrahigh intensity laser plasma interaction. *Physics of plasmas*, 13(11), 2006.

[103] R Shepherd, H Chen, Y Ping, G Dyer, S Wilks, H Chung, A Kemp, S Hanson, K Widmann, K Fournier, et al. Short pulse laser absorption and energy partition at relativistic laser intensities. Technical report, Lawrence Livermore National Lab.(LLNL), Livermore, CA (United States), 2007.

[104] Shuji Sakabe, Masaki Hashida, and Shunsuke Inoue. Generation of intense short electron pulses using high-intensity lasers. *IEEJ Transactions on Electrical and Electronic Engineering*, 17(1):6–12, 2022.

[105] SC Wilks, WL Kruer, M Tabak, and AB Langdon. Absorption of ultra-intense laser pulses. *Physical review letters*, 69(9):1383, 1992.

[106] Paul McKenna and Mark N Quinn. Energetic electron generation and transport in intense laser-solid interactions. In *Laser-Plasma Interactions and Applications*, pages 91–112. Springer, 2013.

[107] Stephen P Hatchett, Curtis G Brown, Thomas E Cowan, Eugene A Henry, Joy S Johnson, Michael H Key, Jeffrey A Koch, A Bruce Langdon, Barbara F Lasinski, Richard W Lee, et al. Electron, photon, and ion beams from the relativistic interaction of petawatt laser pulses with solid targets. *Physics of Plasmas*, 7(5):2076–2082, 2000.

[108] RA Snavely, MH Key, SP Hatchett, TE Cowan, Markus Roth, TW Phillips, MA Stoyer, EA Henry, TC Sangster, MS Singh, et al. Intense high-energy proton beams from petawatt-laser irradiation of solids. *Physical review letters*, 85(14):2945, 2000.

[109] SC Wilks, AB Langdon, TE Cowan, M Roth, M Singh, S Hatchett, MH Key, D Pennington, A MacKinnon, and RA Snavely. Energetic proton generation in ultra-intense laser–solid interactions. *Physics of plasmas*, 8(2):542–549, 2001.

[110] Anatoly Maksimchuk, Shaoting Gu, Kirk Flippo, Donald Umstadter, and V Yu Bychenkov. Forward ion acceleration in thin films driven by a high-intensity laser. *Physical Review Letters*, 84(18):4108, 2000.

[111] L Willingale, A G R Thomas, P M Nilson, H Chen, J Cobble, R S Craxton, A Maksimchuk, P A Norreys, T C Sangster, R H H Scott, et al. Surface waves and electron acceleration from high-power, kilojoule-class laser interactions with underdense plasma. *New Journal of Physics*, 15(2):025023, 2013.

[112] Lorenzo Romagnani, Julien Fuchs, Marco Borghesi, Patrizio Antici, P Audebert, F Ceccherini, T Cowan, T Grismayer, Satyabrata Kar, A Macchi, et al. Dynamics of electric fields driving the laser acceleration of multi-mev protons. *Physical review letters*, 95(19):195001, 2005.

[113] Stephen P Hatchett, Curtis G Brown, Thomas E Cowan, Eugene A Henry, Joy S Johnson, Michael H Key, Jeffrey A Koch, A Bruce Langdon, Barbara F Lasinski, Richard W Lee, et al. Electron, photon, and ion beams from the relativistic interaction of petawatt laser pulses with solid targets. *Physics of Plasmas*, 7(5):2076–2082, 2000.

[114] Patrick Mora. Plasma expansion into a vacuum. *Physical Review Letters*, 90(18):185002, 2003.

[115] M Borghesi, AJ Mackinnon, D Hv Campbell, DG Hicks, S Kar, Pv K Patel, D Price, L Romagnani, Angelo Schiavi, and O Willi. Multi-mev proton source investigations in ultraintense laser-foil interactions. *Physical Review Letters*, 92(5):055003, 2004.

[116] S Ter-Avetisyan, PK Singh, MH Cho, A Andreev, KF Kakolee, H Ahmed, C Scullion, S Sharif, P Hadjisolomou, and M Borghesi. Proton acceleration through a charged cavity created by ultraintense laser pulse. *Physics of Plasmas*, 26(10), 2019.

[117] Donald Umstadter, S-Y Chen, A Maksimchuk, G Mourou, and R Wagner. Nonlinear optics in relativistic plasmas and laser wake field acceleration of electrons. *Science*, 273(5274):472–475, 1996.

[118] Szu-yuan Chen, Anatoly Maksimchuk, and Donald Umstadter. Experimental observation of relativistic nonlinear thomson scattering. *Nature*, 396(6712):653–655, 1998.

[119] GS Sarkisov, V Yu Bychenkov, VN Novikov, VT Tikhonchuk, Anatoly Maksimchuk, S-Y Chen, R Wagner, G Mourou, and Donald Umstadter. Self-focusing, channel formation, and high-energy ion generation in interaction of an intense short laser pulse with a he jet. *Physical Review E*, 59(6):7042, 1999.

[120] Sudeep Banerjee, AR Valenzuela, RC Shah, Anatoly Maksimchuk, and D Umstadter. High harmonic generation in relativistic laser–plasma interaction. *Physics of Plasmas*, 9(5):2393–2398, 2002.

[121] MJ-E Manuel, H Tang, BK Russell, L Willingale, A Maksimchuk, JS Green, EL Alfonso, J Jaquez, L Carlson, D Neely, et al. Enhanced spatial resolution of eljen-204 plastic scintillators for use in rep-rated proton diagnostics. *Review of Scientific Instruments*, 91(10):103301, 2020.

[122] Wm David Kulp III. Ionizing radiation detectors. In *Nuclear Energy: Selected Entries from the Encyclopedia of Sustainability Science and Technology*, pages 427–444. Springer, 2012.

[123] Marcia Dutra R Silva. Ionizing radiation detectors. *Evolution of Ionizing Radiation Research*, pages 189–209, 2015.

[124] WG Cross, J Böhm, M Charles, E Piesch, SM Seltzer, WG Cross, J Böhm, E Piesch, SM Seltzer, et al. Icru report 56. dosimetry of external beta rays for radiation protection. *Journal of the International Commission on Radiation Units and Measurements, Volume os29*, (1):10–1093, 1997.

[125] Slavica Grdanovska. Characterization of radiation damage to a novel photonic crystal sensor. 2015.

[126] John R Lamarsh, Anthony John Baratta, et al. *Introduction to nuclear engineering*, volume 3. Prentice hall Upper Saddle River, NJ, 2001.

[127] G Fiksel, FJ Marshall, C Mileham, and C Stoeckl. Note: Spatial resolution of fuji bas-tr and bas-sr imaging plates. *Review of Scientific Instruments*, 83(8):086103, 2012.

[128] AL Meadowcroft, CD Bentley, and EN Stott. Evaluation of the sensitivity and fading characteristics of an image plate system for x-ray diagnostics. *Review of scientific instruments*, 79(11), 2008.

[129] E Bezak and RA Nelligan. Acceptance testing and commissioning of kodak directview cr-850 digital radiography system. *Australasian Physics & Engineering Sciences in Medicine*, 29:30–34, 2006.

[130] Hui Chen, Norman L Back, Teresa Bartal, FN Beg, David C Eder, Anthony J Link, Andrew G MacPhee, Yuan Ping, Peter M Song, Alan Throop, et al. Absolute calibration of image plates for electrons at energy between 100kev and 4mev. *Review of Scientific Instruments*, 79(3), 2008.

[131] Hui Chen, Anthony J Link, Roger Van Maren, Pravesh K Patel, Ronnie Shepherd, Scott C Wilks, and Peter Beiersdorfer. High performance compact magnetic spectrometers for energetic ion and electron measurement in ultraintense short pulse laser solid interactions. *Review of Scientific Instruments*, 79(10):10E533, 2008.

[132] CK Li, FH Séguin, JA Frenje, JR Rygg, RD Petrasso, RPJ Town, PA Amendt, SP Hatchett, OL Landen, AJ Mackinnon, et al. Monoenergetic proton backlighter for measuring e and b fields and for radiographing implosions and high-energy density plasmas. *Review of scientific instruments*, 77(10), 2006.

[133] JL Jiao, SK He, HB Zhuo, B Qiao, MY Yu, B Zhang, ZG Deng, F Lu, KN Zhou, XD Wang, et al. Experimental observation of ion–ion acoustic instability associated with collisionless shocks in laser-produced plasmas. *The Astrophysical Journal Letters*, 883(2):L37, 2019.

[134] JF Drake, M Swisdak, C Cattell, MA Shay, BN Rogers, and A Zeiler. Progress in proton radiography for diagnosis of icf-relevant plasmas. *Sci*, 299:873, 2003.

[135] A Ravasio, Lorenzo Romagnani, S Le Pape, A Benuzzi-Mounaix, C Cecchetti, D Batani, T Boehly, Marco Borghesi, R Dezulian, L Gremillet, et al. Proton radiography of a shock-compressed target. *Physical Review E*, 82(1):016407, 2010.

[136] Thomson J.J. Rays of positive electricity. *Philosophical Magazine*, 21:225, 1911.

[137] PR Bolton, M Borghesi, C Brenner, DC Carroll, C De Martinis, Francesca Fiorini, A Flacco, V Floquet, J Fuchs, Pablo Gallegos, et al. Instrumentation for

diagnostics and control of laser-accelerated proton (ion) beams. *Physica Medica*, 30(3):255–270, 2014.

[138] EL Clark, K Krushelnick, M Zepf, FN Beg, M Tatarakis, A Machacek, MIK Santala, I Watts, PA Norreys, and AE Dangor. Energetic heavy-ion and proton generation from ultraintense laser-plasma interactions with solids. *Physical Review Letters*, 85(8):1654, 2000.

[139] CG Freeman, G Fiksel, C Stoeckl, N Sinenian, MJ Canfield, GB Graeper, AT Lombardo, CR Stillman, SJ Padalino, C Mileham, et al. Calibration of a thomson parabola ion spectrometer and fujifilm imaging plate detectors for protons, deuterons, and alpha particles. *Review of Scientific Instruments*, 82(7):073301, 2011.

[140] M Hegelich, Stefan Karsch, Georg Pretzler, D Habs, Klaus Witte, W Guenther, M Allen, A Blazevic, J Fuchs, JC Gauthier, et al. Mev ion jets from short-pulse-laser interaction with thin foils. *Physical review letters*, 89(8):085002, 2002.

[141] W Mróz, P Parys, E Woryna, P Straka, B Králiková, J Krása, L Láska, K Mašek, K Rohlena, T Mocek, et al. Thomson parabola ion spectrograph with the microchannel plate image converter in investigations of high-z laser plasma ion sources. *Review of scientific instruments*, 67(3):1272–1274, 1996.

[142] SS Medley and AL Roquemore. Construction and operation of parallel electric and magnetic field spectrometers for mass/energy resolved multi-ion charge exchange diagnostics on the tokamak fusion test reactor. *Review of scientific instruments*, 69(7):2651–2662, 1998.

[143] F Treffert, Q Ji, PA Seidl, A Persaud, B Ludewigt, JJ Barnard, A Friedman, DP Grote, EP Gilson, ID Kaganovich, et al. Design and implementation of a thomson parabola for fluence dependent energy-loss measurements at the neutralized drift compression experiment. *Review of Scientific Instruments*, 89(10), 2018.

[144] S. Ivancic, D. Haberberger, H. Habara, T. Iwawaki, K. S. Anderson, R. S. Craxton, D. H. Froula, D. D. Meyerhofer, C. Stoeckl, K. A. Tanaka, and W. Theobald. Channeling of multikilojoule high-intensity laser beams in an inhomogeneous plasma. *Phys. Rev. E*, 91:051101, May 2015.

[145] S Tochitsky, A Pak, F Fiuza, D Haberberger, N Lemos, A Link, DH Froula, and C Joshi. Laser-driven collisionless shock acceleration of ions from near-critical plasmas. *Physics of Plasmas*, 27(8), 2020.

[146] S Zhang, J Li, CM Krauland, FN Beg, S Muller, W Theobald, J Palastro, T Filkins, D Turnbull, D Haberberger, et al. Pump-depletion dynamics and saturation of stimulated brillouin scattering in shock ignition relevant experiments. *Physical Review E*, 103(6):063208, 2021.

[147] Ricardo A Fonseca, Luis O Silva, Frank S Tsung, Viktor K Decyk, Wei Lu, Chuang Ren, Warren B Mori, S Deng, S Lee, T Katsouleas, et al. Osiris: A three-dimensional, fully relativistic particle in cell code for modeling plasma based accelerators. In *International Conference on Computational Science*, pages 342–351. Springer, 2002.

[148] Roy Gerrit Hemker. *Particle-in-cell modeling of plasma-based accelerators in two and three dimensions*. University of California, Los Angeles, 2000.

[149] Gérard A Mourou, C P Barty, and Michael D Perry. Ultrahigh-intensity laser: physics of the extreme on a tabletop. 1997.

[150] Ishay Pomerantz, Eddie Mccary, Alexander R Meadows, Alexey Arefiev, Aaron C Bernstein, Clay Chester, Jose Cortez, Michael E Donovan, Gilliss Dyer, Erhard W Gaul, et al. Ultrashort pulsed neutron source. *Physical Review Letters*, 113(18):184801, 2014.

[151] L Willingale, SPD Mangles, PM Nilson, RJ Clarke, AE Dangor, MC Kaluza, S Karsch, KL Lancaster, WB Mori, Z Najmudin, et al. Collimated multi-mev ion beams from high-intensity laser interactions with underdense plasma. *Physical review letters*, 96(24):245002, 2006.

[152] Marija Vranic, Ondrej Klimo, Georg Korn, and Stefan Weber. Multi-gev electron-positron beam generation from laser-electron scattering. *Scientific Reports*, 8(1):1–11, 2018.

[153] Franz Pfeiffer, Timm Weitkamp, Oliver Bunk, and Christian David. Phase retrieval and differential phase-contrast imaging with low-brilliance x-ray sources. *Nature physics*, 2(4):258–261, 2006.

[154] Sergey A Pikuz, Tatyana A Shelkovenko, Daniel B Sinars, Katherine M Chandler, and David A Hammer. Phase-contrast x-ray radiography using the x pinch radiation. In *Applications of X Rays Generated from Lasers and Other Bright Sources II*, volume 4504, pages 234–239. SPIE, 2001.

[155] R Toth, JC Kieffer, S Fourmaux, T Ozaki, and A Krol. In-line phase-contrast imaging with a laser-based hard x-ray source. *Review of scientific instruments*, 76(8), 2005.

[156] Felicie Albert, AGR Thomas, SPD Mangles, S Banerjee, Sébastien Corde, Alessandro Flacco, Michael Litos, D Neely, J Vieira, Zulfikar Najmudin, et al. Laser wakefield accelerator based light sources: potential applications and requirements. *Plasma Physics and Controlled Fusion*, 56(8):084015, 2014.

[157] R Tommasini, SP Hatchett, DS Hey, C Iglesias, N Izumi, JA Koch, OL Landen, AJ MacKinnon, C Sorce, JA Delettrez, et al. Development of compton radiography of inertial confinement fusion implosions. *Physics of Plasmas*, 18(5), 2011.

[158] S Jiang, LL Ji, H Audesirk, KM George, J Snyder, A Krygier, P Poole, C Willis, R Daskalova, E Chowdhury, et al. Microengineering laser plasma interactions at relativistic intensities. *Physical review letters*, 116(8):085002, 2016.

[159] Yong Ma, Jiarui Zhao, Yifei Li, Dazhang Li, Liming Chen, Jianxun Liu, Stephen J D Dann, Yanyun Ma, Xiaohu Yang, Zheyi Ge, et al. Ultrahigh-charge electron beams from laser-irradiated solid surface. *Proceedings of the National Academy of Sciences*, 115(27):6980–6985, 2018.

[160] Hongmei Tang, Kavin Tangtartharakul, I-Lin Yeh, Félicie Albert, Róbert Babjak, Hui Chen, Paul T. Campbell, Yong Ma, Philip M Nilson, Brandon K. Russell, Jessica L Shaw, Alexander G. R. Thomas, G. J. Williams, Marija Vranic, Alexey V. Arefiev, and Louise Willingale. The influence of laser focusing conditions on the direct laser acceleration of electrons. to be submitted.

[161] Hongmei Tang, Róbert Babjak, Kavin Tangtartharakul, I-Lin Yeh, Hui Chen, Jessica L Shaw, Marija Vranic, Alexey V. Arefiev, and Louise Willingale. The influence of plasma density gradient on the direct laser acceleration of electrons. to be submitted.

[162] K. McMillen and J. L. Shaw. personal communication, 2023.

[163] Kavin Tangtartharakul, Ilin Yeh, Hongmei Tang, Tao Wang, Louise Willingale, and Alexey Arefiev. Mitigation of the detrimental role of the longitudinal laser electric field during direct laser acceleration of electrons. *Bulletin of the American Physical Society*, 2022.

[164] R. Babjak, L. Willingale, A. Arefiev, and M. Vranic. Efficient direct laser acceleration by multi-petawatt lasers, 2023.

[165] A G R Thomas, Z Najmudin, S P D Mangles, C D Murphy, A E Dangor, C Kamperidis, K L Lancaster, W B Mori, P A Norreys, W Rozmus, et al. Effect of laser-focusing conditions on propagation and monoenergetic electron production in laser-wakefield accelerators. *Physical Review Letters*, 98(9):095004, 2007.

[166] J Davis, GM Petrov, and AL Velikovich. Dynamics of intense laser channel formation in an underdense plasma. *Physics of plasmas*, 12(12):123102, 2005.

[167] Kevin Quinn, Lorenzo Romagnani, Bhuvanesh Ramakrishna, Gianluca Sarri, Mark Eric Dieckmann, PA Wilson, J Fuchs, L Lancia, A Pipahl, T Toncian, et al. Weibel-induced filamentation during an ultrafast laser-driven plasma expansion. *Physical review letters*, 108(13):135001, 2012.

[168] Liang Chen, Xiaoping Ouyang, Bin Liu, Jinliang Liu, Lin Quan, and Zhongbing Zhang. Compensational scintillation detector with a flat energy response for flash x-ray measurements. *Review of Scientific Instruments*, 84(1):013103, 2013.

[169] JS Green, Marco Borghesi, CM Brenner, DC Carroll, NP Dover, PS Foster, Pl Gallegos, S Green, D Kirby, KJ Kirkby, et al. Scintillator-based ion beam profiler for diagnosing laser-accelerated ion beams. In *Laser Acceleration of Electrons, Protons, and Ions; and Medical Applications of Laser-Generated Secondary Sources of Radiation and Particles*, volume 8079, pages 147–154. SPIE, 2011.

[170] Ashita Kumar. *An experimental study of the relative response of plastic scintillators to photons and beta particles within the context of tritium monitoring*. PhD thesis, 2011.

[171] Martin J Berger. Estar, pstar, and astar: Computer programs for calculating stopping-power and range tables for electrons, protons, and helium ions. 1992.

[172] James F Ziegler, Matthias D Ziegler, and Jochen P Biersack. Srim–the stopping and range of ions in matter (2010). *Nuclear Instruments and Methods in Physics Research Section B: Beam Interactions with Materials and Atoms*, 268(11-12):1818–1823, 2010.

[173] JB DIRKS. The theory and practice of scintillation counting, 1964.

[174] Dalal Al Oraini. Calibration of the absolute efficiency of well-type nai (tl) scintillation detector in 0.121–1.408 mev energy range. *Science and Technology of Nuclear Installations*, 2018:1–6, 2018.

[175] JH Bin, Q Ji, PA Seidl, D Raftrey, S Steinke, A Persaud, K Nakamura, A Gonsalves, WP Leemans, and T Schenkel. Absolute calibration of gafchromic film for very high flux laser driven ion beams. *Review of Scientific Instruments*, 90(5):053301, 2019.

[176] Steven W Smith et al. The scientist and engineer's guide to digital signal processing, 1997.

[177] Sedigheh Najafi and Khosro Madanipour. Measurement of the modulation transfer function of a charge-coupled device array by the combination of the self-imaging effect and slanted edge method. *Applied Optics*, 52(19):4724–4727, 2013.

[178] Ulrich Neitzel, Egbert Buhr, Gerhard Hilgers, and Paul R Granfors. Determination of the modulation transfer function using the edge method: Influence of scattered radiation: Scatter influence on mtf determination. *Medical physics*, 31(12):3485–3491, 2004.

[179] RHH Scott, F Perez, JJ Santos, CP Ridgers, JR Davies, KL Lancaster, SD Baton, Ph Nicolai, RMGM Trines, AR Bell, et al. A study of fast electron energy transport in relativistically intense laser-plasma interactions with large density scalelengths. *Physics of Plasmas*, 19(5):053104, 2012.

[180] Yinren Shou, Pengjie Wang, Seong Geun Lee, Yong Joo Rhee, Hwang Woon Lee, Jin Woo Yoon, Jae Hee Sung, Seong Ku Lee, Zhuo Pan, Defeng Kong, et al. Brilliant femtosecond-laser-driven hard x-ray flashes from carbon nanotube plasma. *Nature Photonics*, 17(2):137–142, 2023.

[181] I-Lin. Yeh, Kavin Tangtartharakul, Hongmei Tang, Louise Willingale, and Alexey V. Arefiev. Efficient backward x-ray emission in a plasma irradiated by a ps laser pulse. to be submitted.

[182] PM King, N Lemos, JL Shaw, AL Milder, KA Marsh, A Pak, BM Hegelich, P Michel, J Moody, C Joshi, et al. X-ray analysis methods for sources from self-modulated laser wakefield acceleration driven by picosecond lasers. *Review of Scientific Instruments*, 90(3), 2019.

[183] DR Rusby, CM Brenner, Chris Armstrong, LA Wilson, R Clarke, A Alejo, H Ahmed, NMH Butler, D Haddock, A Higginson, et al. Pulsed x-ray imaging of high-density objects using a ten picosecond high-intensity laser driver. In *Emerging Imaging and Sensing Technologies*, volume 9992, pages 61–68. SPIE, 2016.

[184] M Huault, D De Luis, JI Apiñaniz, M De Marco, C Salgado, N Gordillo, C Gutiérrez Neira, JA Pérez-Hernández, R Fedosejevs, G Gatti, et al. A 2d scintillator-based proton detector for high repetition rate experiments. *High Power Laser Science and Engineering*, 7:e60, 2019.